Drop impact onto a thin film of another liquid

An experimental and theoretical study

Zur Erlangung des akademischen Grades Doktor-Ingenieur (Dr.-Ing.)
Genehmigte Dissertation von Bastian Stumpf aus Schwalmstadt
Tag der Einreichung: 18.04.2023, Tag der Prüfung: 27.06.2023

Erstreferentin: Prof. Dr.-Ing. Jeanette Hussong
Korreferent: Apl. Prof. Dr. Ilia V. Roisman
2. Korreferent: Prof. Dr.-Ing. habil. Bernhard Weigand
Darmstadt, Technische Universität Darmstadt
Jahr der Veröffentlichung der Dissertation auf TUprints: 2024

TECHNISCHE
UNIVERSITÄT
DARMSTADT

Mechanical Engineering
Department

Drop impact onto a thin film of another liquid
An experimental and theoretical study

Accepted doctoral thesis by Bastian Stumpf

Erstreferentin: Prof. Dr.-Ing. Jeanette Hussong
Korreferent: Apl. Prof. Dr. Ilia V. Roisman
2. Korreferent: Prof. Dr.-Ing. habil. Bernhard Weigand

Date of submission: 18.04.2023
Date of thesis defense: 27.06.2023

Darmstadt, Technische Universität Darmstadt
Jahr der Veröffentlichung der Dissertation auf TUprints: 2024

Bitte zitieren Sie dieses Dokument als:
URN: urn:nbn:de:tuda-tuprints-264435
URL: http://tuprints.ulb.tu-darmstadt.de/26443

Dieses Dokument wird bereitgestellt von tuprints,
E-Publishing-Service der TU Darmstadt
http://tuprints.ulb.tu-darmstadt.de
tuprints@ulb.tu-darmstadt.de

For Family and Friends

Erklärungen laut Promotionsordnung

§8 Abs. 1 lit. c PromO

Ich versichere hiermit, dass die elektronische Version meiner Dissertation mit der schriftlichen Version übereinstimmt.

§8 Abs. 1 lit. d PromO

Ich versichere hiermit, dass zu einem vorherigen Zeitpunkt noch keine Promotion versucht wurde. In diesem Fall sind nähere Angaben über Zeitpunkt, Hochschule, Dissertationsthema und Ergebnis dieses Versuchs mitzuteilen.

§9 Abs. 1 PromO

Ich versichere hiermit, dass die vorliegende Dissertation selbstständig und nur unter Verwendung der angegebenen Quellen verfasst wurde.

§9 Abs. 2 PromO

Die Arbeit hat bisher noch nicht zu Prüfungszwecken gedient.

Darmstadt, 18.04.2023

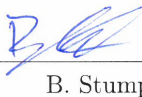

B. Stumpf

Abstract

The impact of drops onto solid substrates wetted by a liquid film of the same or a different liquid is relevant to numerous natural phenomena and various industrial or technical applications. Examples are inkjet printing, spray cooling or agricultural sprays, to name a few. Under certain conditions, the drop-wall-film interaction leads to the formation of secondary droplets (splash) that may influence the process parameters of systems like internal combustion engines or exhaust gas after-treatment systems. The high relevance of drop impact has motivated extensive research investigating the hydrodynamics of the drop-wall-film interaction, defining different regimes or characterising the drop impact outcome. These studies focus largely on impact conditions where the liquids of drop and film are the same (one-component). In many real-world applications, the fluid properties of the liquids in the film and the drop differ (two-component). In this case, additional influencing parameters related to the different fluid properties lead to a complex drop-wall-film interaction that is not entirely understood, thus making further research necessary.

This work is dedicated to improving the understanding of the complex drop-wall-film interactions during drop impact by considering three main aspects. First, the focus is on the flow dynamics in the wall near lamella formed during drop impact. Second, splashing mechanisms, particularly the phenomenon of corona detachment and the associated breakup mechanisms, are investigated. Finally, a new tool for the characterisation of secondary droplets is developed.

The impact of a drop onto a wetted substrate generates a radially expanding lamella flow adjacent to the wall. After impact, a growing viscous boundary layer increasingly decelerates the lamella flow until it eventually comes to a complete stop, while the thickness of the lamella reaches an asymptotic value. A theoretical model is developed that describes the dynamics of this lamella flow accounting for the viscous boundary layer in both the drop and the wall-film liquid. Experiments measuring the temporal evolution of the lamella thickness for a large range of impact parameters varying the Weber and Reynolds number as well as the ratio of film to drop viscosity provide physical evidence for the theoretical description.

Further focus is placed on gaining a better understanding of the mechanism of corona detachment, where the crown completely and almost instantaneously detaches from the wall-film. A high-speed camera system is used to observe and characterise the drop impact under conditions that lead to corona detachment. Moreover, special experiments are conducted where the Taylor-Culick relation is utilised to gain film thickness information from evaluating the propagation velocity

of artificially induced ruptures in the crown sheet. A hypothesis is formulated that attributes the detachment to small holes that are triggered by disturbances emerging from the early instances of impact. These holes spread, merge and thus undercut the crown sheet leading to its detachment. Building upon this hypothesis, the specific hole formation rate and the hole propagation velocity are modelled based on which the time of detachment is predicted. The theoretical scaling of time of detachment agrees well with the experiments.

Finally, an imaging technique is developed to determine the volume fraction of two-component drops containing immiscible liquids by evaluating images of a drop from two perpendicular perspectives. This technique is supported by a machine learning algorithm that is taught using synthetically generated images. The approach is validated by evaluating images of single two-component droplets with known volume fractions that are placed in an acoustic levitator. The application of this technique is demonstrated by measuring the volume fraction of secondary droplets that emerge from a two-component splash.

Zusammenfassung

Der Aufprall von Tropfen auf feste Substrate, die von einem Flüssigkeitsfilm der gleichen oder einer anderen Flüssigkeit benetzt sind, ist für zahlreiche Naturphänomene und verschiedene industrielle oder technische Anwendungen relevant. Beispiele sind der Tintenstrahldruck, die Sprühkühlung oder landwirtschaftliche Sprays, um nur einige zu nennen. Unter bestimmten Bedingungen führt die Tropfen-Wand-Film-Wechselwirkung zur Bildung von Sekundärtropfen (Splash), die die Prozessparameter von Systemen wie Verbrennungsmotoren oder Abgasnachbehandlungssystemen beeinflussen können. Die hohe Relevanz des Tropfenaufpralls hat umfangreiche Forschungsarbeiten motiviert, die die Hydrodynamik der Tropfen-Wand-Film-Wechselwirkung untersuchen, verschiedene Regime definieren oder das Ergebnis des Tropfenaufpralls charakterisieren. Diese Studien konzentrieren sich weitgehend auf Aufprallbedingungen, bei denen die Flüssigkeiten von Tropfen und Film gleich sind (einkomponentig). In vielen realen Anwendungen sind die Eigenschaften der Flüssigkeiten im Film und im Tropfen allerdings unterschiedlich (zweikomponentig). In diesem Fall führen zusätzliche Einflussparameter, die mit den unterschiedlichen Fluideigenschaften zusammenhängen, zu einer komplexen Tropfen-Wand-Film-Wechselwirkung, die noch nicht vollständig verstanden ist und somit weitere Forschung notwendig macht.

Die vorliegende Arbeit widmet sich der Verbesserung des Verständnisses dieser komplexen Tropfen-Wand-Film-Wechselwirkungen beim Tropfenaufprall unter Berücksichtigung von drei Hauptaspekten. Zunächst liegt der Schwerpunkt auf der Strömungsdynamik in der wandnahen Lamelle, die sich beim Tropfenaufprall bildet. Des Weiteren werden die Splashing-Mechanismen, insbesondere das Phänomen der Koronaablösung und die damit verbundenen Aufrissmechanismen, untersucht. Schließlich wird eine Methode zur Charakterisierung von Sekundärtropfen entwickelt.

Der Aufprall eines Tropfens auf ein benetztes Substrat erzeugt eine sich radial ausbreitende Lamellenströmung, die an die Wand angrenzt. Nach dem Aufprall bremst eine wachsende viskose Grenzschicht die Lamellenströmung zunehmend ab, bis sie schließlich vollständig zum Stillstand kommt, während die Dicke der Lamelle einen asymptotischen Wert erreicht. Es wird ein theoretisches Modell entwickelt, das die Dynamik dieser Lamellenströmung unter Berücksichtigung der viskosen Grenzschicht sowohl im Tropfen als auch in der Wand-Film-Flüssigkeit beschreibt. Experimente, bei denen die zeitliche Entwicklung der Lamellendicke

für einen großen Bereich von Aufprallparametern unter Variation der Weber- und Reynoldszahl sowie des Verhältnisses von Film- zu Tropfenviskosität gemessen wird, liefern physikalische Belege für die theoretische Beschreibung.

Ein weiterer Schwerpunkt liegt darin das Verständnis des Mechanismus der Koronaablösung zu verbessern, bei der sich die Krone vollständig und fast augenblicklich vom Wandfilm ablöst. Ein Hochgeschwindigkeitskamerasystem wird eingesetzt, um den Tropfenaufprall unter Bedingungen zu beobachten und zu charakterisieren, die zur Koronaablösung führen. Darüber hinaus werden spezielle Experimente durchgeführt, bei denen die Taylor-Culick-Relation genutzt wird, um Informationen über die Kronendicke zu gewinnen, indem die Ausbreitungsgeschwindigkeit von künstlich erzeugten Rissen im Kronenblech ausgewertet wird. Es wird eine Hypothese formuliert, die die Ablösung auf kleine Löcher zurückführt, die durch Störungen ausgelöst werden, die in einer frühen Phase des Aufpralls entstehen. Diese Löcher breiten sich aus, verbinden sich und unterschneiden so die Krone, was zu deren Ablösung führt. Auf der Grundlage dieser Hypothese werden die spezifische Lochbildungsrate und die Lochausbreitungsgeschwindigkeit modelliert, um den Zeitpunkt der Ablösung vorherzusagen. Die theoretische Skalierung der Ablösungszeit stimmt gut mit den Experimenten überein.

Schließlich wird ein Verfahren zur Bestimmung des Volumenanteils von Zweikomponententropfen mit nicht mischbaren Flüssigkeiten entwickelt, in dem Bilder eines Tropfens aus zwei senkrechten Perspektiven ausgewertet werden. Diese Technik wird durch einen Algorithmus für maschinelles Lernen unterstützt, der anhand synthetisch erzeugter Bilder trainiert wird. Der Ansatz wird durch die Auswertung von Bildern einzelner Zweikomponententropfen mit bekannten Volumenanteilen validiert, die in einem akustischen Levitator platziert werden. Die Anwendung dieser Technik wird durch die Messung des Volumenanteils von Sekundärtropfen demonstriert, die aus einem Zweikomponentensplash hervorgehen.

Acknowledgements

First of all, I want to express my sincere gratitude to my supervisors *Prof. Dr.-Ing. Jeanette Hussong*, *Apl. Prof. Dr. Ilia Roisman* and *Prof. Dr.-Ing. Cameron Tropea* for giving me the opportunity to work at the Institute for Fluid Mechanics and Aerodynamics, for all the advice, their shared expertise, the long discussions and the supervision during my time as a doctoral student. Additionally, I would like to thank *Prof. Dr.-Ing. habil. Bernhard Weigand* for acting as the external reviewer of this thesis. Many thanks to my colleagues at the Institute for Fluid Mechanics and Aerodynamics, who supported and encouraged me throughout this dissertation and always provided an interested audience for all kinds of problems. I enjoyed the open-minded and supportive working atmosphere and am grateful for numerous fruitful discussions. Special thanks to *Max Lausch*, *Mark Glörfeld*, *Till Werner* and *Ivan Joksimovic* for assisting with the proofreading. Furthermore, I want to thank the colleagues from the collaborative research center SFB/TRR 150 for the valuable exchange. In particular, I want to thank *Malki Maliha* and *Milad Bagheri* for the successful cooperations. The financial support from the *Deutsche Forschungsgemeinschaft* in the framework of the collaborative research center SFB/TRR 150 *Turbulent, chemically reactive, multi-phase flows near walls* is gratefully acknowledged. Special thanks go to all the students who supported my research. I am very grateful to *Jonas H. Ruesch* whose hard work and creative ideas were indispensable to the third considered scenario. Gratitude is also owed to *Prof. A. Yarin*, without whose expertise the formulation of the model in the second considered scenario would not have been possible. Moreover, I want to thank the administrative team formed by *Birgit Neuthe* and *Susanne Krüger*, who ensured that all my administrative needs were met and who always had an open ear to problems beyond administration. Essential parts of the experimental setup were manufactured in the workshop under the guidance of *Ilona Kaufhold*. Finally, I want express deep gratitude to my parents *Christine* and *Heiner Stumpf*, my brother *Jakob Stumpf* and my friends for their continuous support and encouragement. Especially, I would like to thank *Svenja Möller* for her patience, constant positive motivation and for being a source of much-needed distraction in stressful times.
Thank you
Bastian

Publications

Journal publications

Stumpf, B., Ruesch, J. H., Roisman, I. V., Tropea, C. and Hussong, J.: "An imaging technique for determining the volume fraction of two-component droplets of immiscible fluids". *Exp Fluids* 63, 114 (2022). DOI: 10.1007/s00348-022-03462-1.

Stumpf, B., Hussong, J. and Roisman I. V.: "Drop Impact onto a Substrate Wetted by another Liquid: Flow in the Wall Film". *Colloids Interfaces* 6, 58 (2022). DOI: 10.3390/colloids6040058.

Stumpf, B., Roisman, I. V., Tropea, C. and Yarin, A. L.: "Drop Impact onto a Substrate Wetted by another Liquid: Detachment from the wall film". *J. Fluid Mech* 956, A10 (2023). DOI: 10.1017/jfm.2022.1060.

Kissing J., **Stumpf, B.**, Kriegseis J., Hussong J. and Tropea C.: "Delaying leading edge vortex detachment by plasma flow control at topologically critical locations." *Phys Rev Fluids* 6, 023101 (2021). DOI: 10.1103/PhysRevFluids.6.023101.

Bagheri M., **Stumpf, B.**, Roisman I. V., Tropea C., Hussong, J. Wörner M. and Marschall H.: "Interfacial relaxation – Crucial for phase-field methods to capture low to high energy drop-film impacts". *Int J Heat Fluid Flow* 94, 108943 (2022). DOI: 10.1016/j. ijheatfluidflow.2022.108943.

Maliha M., **Stumpf, B.**, Beyer F., Kühnert M., Kubach H. Roisman, I. V. Hussong, J. and Koch, T.: "Optical investigation on the interaction between a fuel-spray and an oil wetted wall with the focus on secondary droplets." *Int. J. Engine Res.* 0, 0 (2022). DOI: 10.1177/14680874221095235.

Bagheri M., **Stumpf, B.**, Roisman I. V., Dadvand A., Wörner M., Marschall H.: "A unified finite volume framework for phase-field simulations of an arbitrary number of fluid phases". *Can J Chem Eng* 100, 9, pp.2291-2308, (2022). DOI: 10.1002/cjce.24510.

Conference proceedings

Stumpf, B., Roisman, I. V., Tropea, C., Yarin, A. L., Hussong, J.: *Drop Impact onto a Thin Viscous Film: Corona Thickness Measurements*, ICLASS 2021, 15th Triennial International Conference on Liquid Atomization and Spray Systems, Edinburgh, UK, 29 Aug. - 2 Sept. 2021, 10.2218/iclass.2021.5991 .

Stumpf, B., Roisman I. V., Tropea, C., Hussong, J.: *The Role of Viscosity Ratio on the Formation of a Residual Film after Drop Impact Onto Thin Liquid Films*. ILASS–Europe 2022, 31th Conference on Liquid Atomization and Spray Systems, 6-8 September 2022, Virtual, Israel.

Contents

1. Introduction

1.1. Motivation

The impact of drops onto dry or wetted substrates is fundamental to various practical applications. Among them are inkjet printing, spray painting, spray cooling, agricultural sprays, fire extinguishing, internal combustion engines or exhaust gas after-treatment systems, to name a few (Kim and Ryou, 2003; Liang and Mudawar, 2016; Dreizler et al., 2021). The fascinating and highly complex drop impact phenomenon has drawn researchers' attention for more than a century. As early as the beginning of the 20th century Worthington (1908) published his phenomenological work, containing impressive photographs of the splash resulting from a drop impacting onto a liquid film. Since then, many research areas have developed that investigate the impact of drops onto films under various conditions, some of which are briefly cited below.

Motivated by the need to prevent icing phenomena in aviation, the impact of supercooled drops was extensively investigated (Cao et al., 2018; Gloerfeld et al., 2021). Spray cooling applications motivated research on drops impacting onto superheated targets. Comprehensive reviews on this topic can be found in Kim (2007), Liang and Mudawar (2017a), Liang and Mudawar (2017b), Breitenbach et al. (2018b), and Wang et al. (2020). Applications in soft bio-printing or tissue engineering create a need for research on drop impact onto more complex substrates (Alireza, 2022) for instance, flexible materials (Kittel et al., 2018) or nanofibres (Heinz et al., 2021). Fundamental findings about the drop impact onto solid substrates are summarized in Josserand and Thoroddsen (2016). For instance analytical solutions are obtained that are applicable to the lamella flow that is created during the impact process (Yarin and Weiss, 1995; Roisman, 2009a). These models also have implications for the other areas of drop impact.

In numerous applications, drops occur in the form of sprays. The interaction of a spray with a wall cannot be described exclusively by a superposition of many single drop impacts. One reason for this is that additional drop-drop interactions need to be accounted for (Moreira et al., 2010). Nevertheless, a fundamental understanding of the interactions of a single drop with a wall is necessary to be able to understand the complex spray-wall interactions. Furthermore, in a spray, only the first droplets that impact interact with a dry substrate. In many cases, subsequent drops will impact onto a substrate wetted by the previous drops. Evidently, the interactions of a drop with a wetted substrate are essential to the spray impact process.

In many practical applications, the film and drop consist of different liquids, or the fluid properties of both liquids differ. Spray cooling, IC engines, exhaust gas after-treatment and fire extinguishing are examples where the effect of the differing liquids is of interest.

Spray cooling is applied in numerous applications ranging from cryogenic cooling to traditional industries such as hot forging Breitenbach et al. (2018b). In the scope of advancing digitalisation and the associated increase in power density of electronic devices, spray cooling becomes increasingly relevant (Kandlikar and Bapat, 2007). Moreover, the increasing demands on the thermal management of electric powertrains lead to innovative new technologies such as oil spray cooling in electric power trains (Ghahfarokhi et al., 2022). During spray cooling, the film typically has a significantly higher temperature than the impacting spray. Due to the temperature dependence of liquid properties such as viscosity, surface tension and density, this may lead to different liquid properties of the film and the drop. A fundamental understanding of the effect of differing fluid properties on the impact of drops is beneficial to improving these systems. The temporal evolution of the lamella height of the drop over time would be one crucial parameter that is necessary to calculate the heat flux from the target during drop impact (Breitenbach et al., 2018b).
Another application where drop-wall-film interactions of differing liquids become relevant is the internal combustion (IC) engine. In the recent years downsizing for the purpose of a better fuel efficiency is a trend that influences the design of IC engines (Golloch and Merker, 2005). Due to ever smaller engines the interactions of the spray with the engine walls becomes increasingly important. In an IC engine the piston and cylinder wall are wetted by a thin oil film. Secondary droplets resulting from the interaction of the spray and the wall-film may transport oil into the combustion chamber and thus influence the mixture composition potentially leading to pre-ignition or knocking (Kubach et al., 2018). For a knowledge based improvement of those systems, the composition of those secondary droplets is of particular interest.

A further example is exhaust gas after-treatment systems. Well-known examples for propulsion systems that require an exhaust gas after-treatment are diesel fuelled internal combustion engines. But also new technologies such as hydrogen engines may rely on exhaust gas after treatment as the high temperatures generated during hydrogen combustion favour the thermal generation of nitrogen oxides (Hosseini and Butler, 2020; Lott et al., 2022). One established technology used to reduce nitrogen oxides from the exhaust gas is selective catalytic reduction (SCR) (Forzatti, 2001). SCR systems utilize urea-water solutions which are injected into the exhaust tract. In the process spray will wet the wall and due to evaporation and deposit formation, the film can have a different urea concentration than the injected spray (Birkhold et al., 2006; Schmidt et al., 2021). Secondary droplets formed by the impact of the spray on the wetted wall may in turn influence the process parameters of the exhaust gas after-treatment process.

Moreover, sprays are very effective in quenching fires that burn solid materials. However, in the case of a film fuelled fire, the impact of the spray can have a contrary effect and even accelerate the fire. One approach is to use very fine sprays (Kim and Ryou, 2003). Here, the evaporation of the droplets displaces oxygen and cools the fire to extinguish it. In this scenario, the spray liquid is typically different from the film liquid. Both miscible and immiscible liquid combinations are possible. To avoid splashing and the potential acceleration of the fire, the parameters of the spray need to be carefully chosen. A fundamental understanding of the droplet-wall film interaction in two-component systems is necessary to design such systems. (Banks et al., 2013; Kim and Ryou, 2003)

Additionally, the results from generic single droplet experiments can be utilized in combination with numerical methods (Josserand and Zaleski, 2003; Xie et al., 2004; Coppola et al., 2011; Lee et al., 2011). This can happen on different levels. The first level describes the integration of simplified models into a complete system simulation. When simulating complex phenomena such as a spray impact, resolving the time and length scales of each droplet is challenging due to very high computational costs. This problem can be addressed by integrating simplified models obtained from generic experiments. Those models serve to predict certain traits of the drop impact outcome, for instance, the deposited mass or the characteristics of secondary droplets, based on known input parameters (Schmidt et al., 2021). The second level describes the validation of numerical code in system simulations as well as single drop simulations that resolve the respective time and length scales. The numerical simulation of multi-phase flows involving high impact dynamics as they may occur during the impact of a single drop is highly challenging. Data determined from generic drop impact experiments can be used as a benchmark to validate numerical methods as it has been done, in Bagheri et al. (2022b) and Bagheri et al. (2022a). Once validated, the numerical models can potentially be used to perform numerical experiments under conditions that are experimentally difficult to access.

Despite the high relevance of one and two-component drop impact, there are still open questions that need to be answered. The hydrodynamics of drop impact onto dry substrates and liquid films have been extensively researched and the kinematics of crown evolution are well described. However, the extent of splash and the associated parameters of secondary droplets are still challenging to predict. Furthermore, the evolution of the crown sheet thickness is an elusive parameter that is vital for a complete understanding of splashing phenomena. In particular, in situations where the liquids in drop and wall film have different liquid parameters, influences that can be attributed to the differing liquid properties lead to a more complex drop-wall-film interaction that, although it has received increasing scientific interest (Geppert et al., 2017; Ersoy and Eslamian, 2020; Bernard et al., 2021), is not yet completely understood. The high relevance of such two-component drop impact scenarios to many real world applications suggests that more research is necessary.

1.2. Objectives and outline of this thesis

This work is dedicated to achieving a better understanding of drop impact onto thin liquid films of the same or another liquid whereby the focus is placed on three aspects of the drop-wall-film interaction, being the dynamics of the lamella flow, a special mode of splash - the corona detachment and the associated breakup mechanism, and finally the volumetric composition of immiscible secondary droplets. Methodically this work can be split into two parts. The first part is an experimental study aimed at a better understanding of physical processes involved in the lamella flow generated by the drop impact and the processes that lead to the corona detachment, while the second part is dedicated exclusively to developing a technique to determine the volume fraction of immiscible two-component drops.

In the experimental study the flow in the lamella that forms during drop impact is considered, focusing on the residual layer that remains on the substrate after impact. Upon impact, growing viscous boundary layers in both the wall film and the drop lamella develop and eventually decelerate the flow until it comes to a complete stop. Thus, the lamella reaches an asymptotic value of thickness. The subject of investigation is the influence of different viscosity in film and drop, the initial film thickness and varying impact parameters in terms of Reynolds and Weber number on this residual layer.

The second part of the experimental investigation centres on the corona detachment. Under certain conditions, the crown sheet that forms during drop impact detaches almost instantaneously from the underlying wall film. This phenomenon is experimentally investigated with a focus on the time of detachment and the evolution of film thickness in the crown sheet, from which possible breakup mechanisms are derived.

From a splash resulting from a drop impact onto another immiscible liquid, secondary drops emerge, in which one liquid fully engulfs the other liquid, and thus drops in drops are formed. The volumetric fraction of the respective liquids in such droplets is difficult to access, and therefore experimental data on this quantity is rare. A new method to determine the volume fraction of such drops is developed in the final part of this dissertation.

The structure of this dissertation comprises seven chapters briefly introduced in this paragraph. First, an overview of the current state of the art and the theoretical background is given in Chapter 2, where existing theories and findings on the drop-wall-film interaction are discussed and the research gaps this dissertation addresses are shown. In Chapter 3, the experimental facilities and methods are presented. Furthermore, the post-processing procedures used for evaluation are introduced and an overview of the experimental procedure is given. Afterwards, in Chapter 4, the results of the lamella thickness measurements are shown and discussed. Based on these results a model predicting the residual film thickness is developed and compared to the experiments. The results of the corona detachment investigations are presented in Chapter 5, after which, the developed technique for

volume fraction determination and its validation is introduced, and its application is demonstrated on a crown splash. Finally, the conclusions drawn from the three result chapters are summarized and an outlook for possible future research is given in Chapter 6.

2. State of the art and theoretical background

Within the scope of this work, experiments on drop-wall-film interactions are conducted, evaluated and interpreted, and the results are used to develop analytical models. Furthermore, a new measurement technique is developed to determine the volume fraction of immiscible two-component droplets. In the following sections, first, the current state of the art in drop impact research is summarised, giving a review of experimental and analytical work on the topic in Sec. 2.1, followed by a review of the methods that are used to characterise and analyse drop-wall-film interactions in Sec. 2.2. This chapter aims to give context to the current study, provide the necessary theoretical background and highlight the knowledge gaps in research this dissertation addresses.

2.1. Characterisation and modelling of drop impact phenomena

The central subject of this thesis is the investigation of drop-wall-film interaction of a drop that impacts normally onto a substrate wetted by the same or another liquid. When the liquid of the drop and the film is the same, the impact will be referred to as a one-component impact, while the case in which the liquids differ is referred to as a two-component drop impact. This section provides a review of the literature and current research in and on drop-wall-film interactions, beginning with parameters and dimensionless groups that govern a drop impact in Sec. 2.1.1, moving to regimes and phases of drop impact in Sec. 2.1.2 and Sec. 2.1.3, respectively. Moreover, the early stages of drop impact are discussed in Sec. 2.1.4, whereafter the dynamics of a spreading lamella at late times of the impact are described in Sec. 2.1.5. Subsequently, the characteristics of crown formation and evolution are discussed in Sec. 2.1.6, followed by a brief review of splashing phenomena in Sec. 2.1.7. Finally, the two-component drop impact is discussed in Sec. 2.1.8.

2.1.1. Parameters and dimensionless groups governing drop impact

The impact of a drop on a thin liquid film can result in various intriguing shapes formed in an interplay of viscous forces, surface tension, and inertia, which have fascinated researchers over a decade. Despite the high complexity of this physics rich interaction, several parameters are identified that have an influence on the outcome. The characteristics of the impacting drop in terms of impact velocity U_0, drop diameter D_0 and its fluid parameters viscosity ν_d, surface tension σ_d and density ρ_d, affect the outcome of the impact just as the characteristics of the liquid film do, which are its height H_{f0} and its fluid parameters ν_f, σ_f and ρ_f. The subscripts d and f are used to denote whether the corresponding quantity describes a property of the drop or a property of the film. Furthermore, the temperature T, as well as the properties of the surrounding gas in terms of viscosity and density, may influence the evolution and outcome of the drop impact. Comprehensive reviews on the topic can be found in Yarin (2006), Moreira et al. (2010), Liang and Mudawar (2016), Yarin et al. (2017), and Lamanna et al. (2020).

The influencing parameters can be summarized into dimensionless groups. The most commonly used expressions in the context of drop impact onto thin films are introduced below.

The Reynolds number represents the relation of inertial to viscous forces as

$$\mathrm{Re} = \frac{D_0 U_0}{\nu_d} = \frac{\rho_d U_0 D_0}{\eta_d}, \tag{2.1}$$

where η_d is the dynamic viscosity of the drop. Effects of surface tension are included in the Weber number, which are related to the inertial forces defined by

$$\mathrm{We} = \frac{\rho_d U_0^2 D_0}{\sigma_d}. \tag{2.2}$$

A combination of Reynolds and Weber numbers; hence, the relation of viscous forces to the square root of the product of inertia and surface tension, is represented by the Ohnesorge number as

$$\mathrm{Oh} = \frac{\eta_d}{\sqrt{\rho_d \sigma_d D_0}} = \frac{\sqrt{\mathrm{We}}}{\mathrm{Re}}. \tag{2.3}$$

Note that the Ohnesorge number does not account for the impact velocity. Another dimensionless parameter that incorporates the effects of viscosity, inertia and surface tension in a single quantity is the K number. This parameter is used in K type correlations to specify a splashing threshold. A more detailed discussion of splashing phenomena and related thresholds will be given in Sec. 2.1.7. The following formulation defines the K number based on Mundo et al. (1995) as

$$K = \mathrm{WeOh}^{-0.4} = \mathrm{We}^{0.8}\mathrm{Re}^{0.4} \tag{2.4}$$

Besides the dimensionless groups, also single parameters can be non-dimensionalised using characteristic scales. The drop diameter D_0 is used as a length scale while the drop velocity U_0 is used as a velocity scale and the ratio of both D_0/U_0 is used as a timescale. Dimensionless lengths, times and velocities, scaled by those parameters are signified with a tilde in the following. Following this principle, the dimensionless film thickness $\tilde{\delta}$ and the dimensionless time $\tilde{t}$ can be expressed as:

$$\tilde{\delta} = \frac{H_{\mathrm{f0}}}{D_0} \qquad \tilde{t} = \frac{tU_0}{D_0}. \tag{2.5}$$

When the liquid of the drop and the film differ, additional quantities such as the interfacial tension between the film and the drop liquid σ_{df}, or the ratios between the respective viscosity and density become relevant. These ratios are defined by

$$\kappa_* = \frac{\nu_f}{\nu_d}, \quad \varrho_* = \frac{\varrho_f}{\varrho_d}. \tag{2.6}$$

Generally, the fluid properties and pressure of the surrounding gas can further influence the outcome of the drop impact (Liang et al., 2014a). However, within the scope of this work, the drop-wall-film interactions will be considered under ambient conditions, and thus the effects of changing gas properties will not be discussed further.

2.1.2. Regimes of drop impact onto wetted substrates

The impact of a drop onto a wetted substrate can be classified based on the resulting morphology and outcome. Four general regimes, namely *floating/bouncing*, *deposition*, *crown formation* and *splash*, are identified. Snapshots of experiments in each regime are depicted in Fig. 2.1.

For impacts with relatively low kinetic energy upon impact, when the Weber number is of the order unity We $= \mathcal{O}(1)$, it can be observed that the drop floats on the liquid film. At slightly higher Weber numbers (We$= \mathcal{O}(10)$), the drop partially or fully bounces back in the air and merges with the film after a series of bounces (Pan and Law, 2007). This behaviour is attributed to a thin gas layer that forms between the drop and the film. If the inertia of the impact is high enough to penetrate this thin gas layer, advective forces will dominate, and the drop will be absorbed by the liquid film (Tang et al., 2019). Rioboo et al. (2003) termed this regime *deposition*. The inertia in the deposition regime is not high enough to overcome viscous losses and surface tension, hence the impact energy is fully dissipated. In this case no visible rim forms above the film. As inertia in relation to surface tension and viscosity increases, a crown-like liquid sheet bounded by a free rim ejects during the impact process. The regime where the crown forms but does not disintegrate into secondary droplets will be referred to as *crown formation* regime in the following. Rioboo et al. (2003) showed that a transition from deposition to crown formation could be characterised by the K number, which

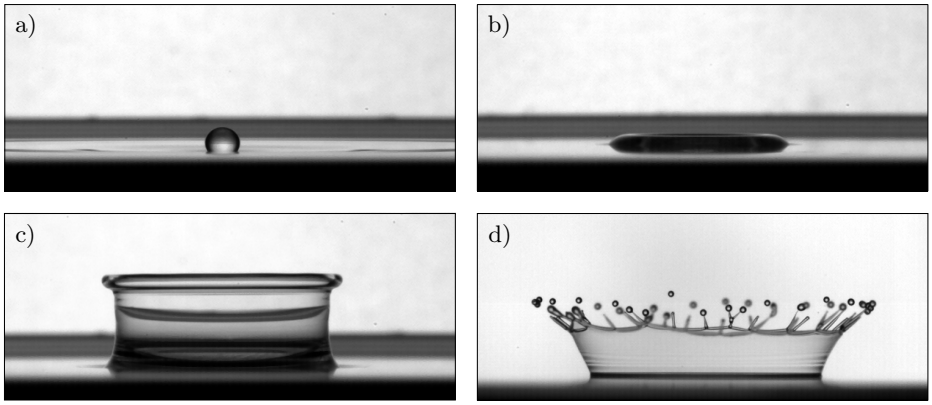

Figure 2.1: Snapshots of experiments showing the result of drop impact in different regimes. a) floating/bouncing (We = 0.62 , Re = 24, $\tilde{\delta} \approx 0.33$), b) deposition (We = 78, Re = 300, $\tilde{\delta} = 0.33$) c) crown formation (We = 700, Re = 900, $\tilde{\delta} = 0.33$, d) splash (We = 1224, Re = 604, $\tilde{\delta} = 0.04$).

they found to be $K \approx 400$ for $0.08 < \tilde{\delta} < 0.14$. For even higher impact energies in terms of K number, the crown sheet may become unstable, resulting in the ejection of secondary droplets. All scenarios in which the impact of the drop leads to the ejection of secondary droplets are assigned to the *splashing* regime. Hereby, the parameter K is often used to bound the splashing regime. The phenomenon of splashing, the associated thresholds and mechanisms, and the characteristics of secondary droplets, will be discussed in Sec. 2.1.7.

For drop impact onto wetted surfaces, distinct regimes with respect to the wall-film characteristics are distinguished. Tropea and Marengo (1999) proposed the four regimes, namely, very thin film, thin film, thick film and deep pool and used the three dimensionless parameters $\tilde{\delta}$, $R_{nd} = R_a/D_0$ and L_{nd} to separate the regimes, where R_a is the mean surface roughness, and L_{nd} is a characteristic roughness length scale. In the very thin film regime, a dominating role is attributed to the properties of the wall in terms of surface roughness. The influence of roughness decreases in the thin film regime, where the film thickness becomes the dominating factor. For drop impact in the thick film regime (also known as shallow pool regime), wall properties do not influence the drop impact, but the influence of the film thickness remains. In the deep pool regime, the result of drop impact solely depends on the impact parameters and fluid properties; hence, film thickness and wall properties do not influence the result of impact anymore. (Liang and

Regime	Range	Ref.
Very thin film	$L_{nd} < \tilde{\delta} < 3R_{nd}^{0.16}$	Tropea and Marengo (1999)
Thin film	$3R_{nd}^{0.16} < \tilde{\delta} < 1.5$	Tropea and Marengo (1999)
	$\tilde{\delta} < 1$	Cossali et al. (1997) Motzkus et al. (2011)
Thick film	$1.5 < \tilde{\delta} < 4$	Tropea and Marengo (1999)
	$\tilde{\delta} > 1$	Motzkus et al. (2011)
Deep pool	$\tilde{\delta} \gg 4$	Tropea and Marengo (1999)

Table 2.1: Distinction of drop impact regimes by characteristics of the wall-film according to the summaries of Geppert (2019) and Kittel (2019).

Mudawar, 2016)
Different delimitations of the wall-film regimes can be found in the literature as summarized in Table 2.1.

This work mainly focuses on drop-wall-film interactions in the crown formation and splashing regime, where the inertia of the impact plays a dominating role (We $\gg 1$, Re $\gg 1$).

2.1.3. Phases and zones of drop impact

The impact of a drop onto a dry or wetted substrate is a highly transient phenomenon. In Fig. 2.2, snapshots of the impact at different instants of an experiment are exemplified. In this experiment, a silicone oil drop impacts onto a wetted substrate in the splashing regime. After the initial contact of the drop with the wall-film, a liquid jet is ejected in the horizontal direction, as depicted in the enlarged detail of Fig. 2.2a). This jet, named *ejecta*, transforms into the radially spreading crown-like liquid sheet, which is referred to as *crown* or *corona* (Fig. 2.2 a-b). It is confined by a free liquid rim which eventually becomes unstable. The unstable rim forms finger-like jets that finally break into secondary drops (Fig 2.2 d-g). After it has reached its maximum height, the crown recedes, if it has not entirely disintegrated into secondary drops (Fig 2.2 e-h).

The transient nature of the drop impact suggests that it can be divided into different phases. One approach is to distinguish between the phases based on phenomenological features. This was done by Cossali et al. (2004), who proposed four phases which are assigned to the instants shown in Fig 2.2 in the following.

- Drop impact and resulting lamella formation Fig. 2.2 a-b.
- Crown and cavity formation Fig. 2.2 b-c.
- Jet formation, instability and breakup Fig. 2.2 d-f.
- Crown collapse Fig. 2.2 e-h.

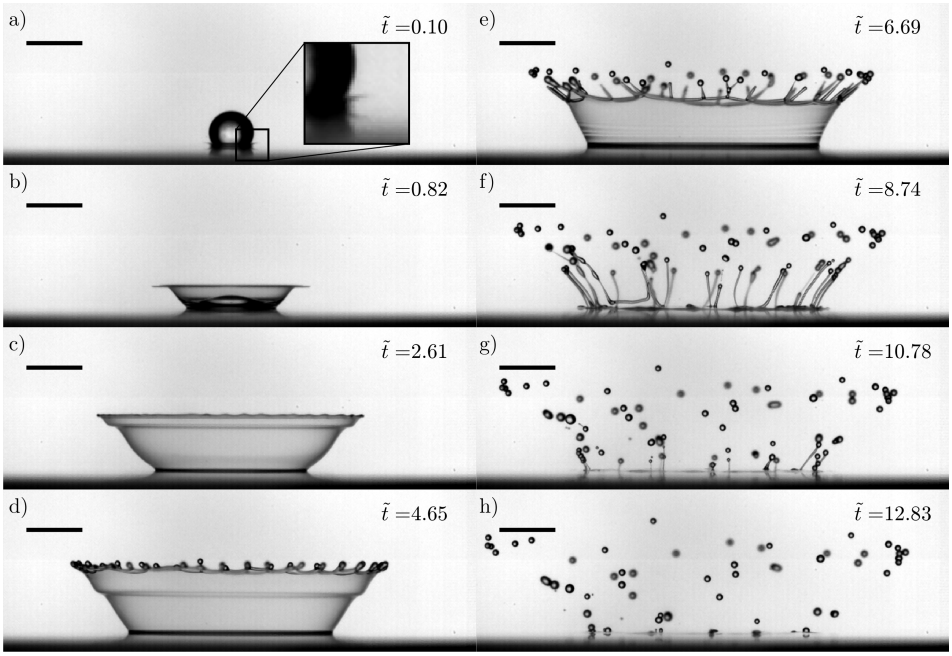

Figure 2.2: Temporal evolution of the crown after a drop impacting onto a wetted substrate resulting in a splash. Impact parameters: We = 1230, Re = 612, $\tilde{\delta} = 0.042$.

Another concept is distinguishing between phases based on modelling approaches (Yarin et al., 2017). For instance, distinctions are drawn between the very early stages of impact $\tilde{t} \ll 1$ at which the drop intersects with the liquid film and large times of impact $\tilde{t} \gg 1$ when the impact has generated a radially expanding flow in a thin liquid sheet. The early stage is characterised by high shear gradients and a complicated geometry which makes the flow difficult to model, while the radially expanding liquid sheet that is generated at large times after impact is well suited for analytical models applying remote asymptotics (Yarin et al., 2017). Lamanna et al. (2022) propose categorizing the impact into three phases based on modelling approaches and the evolution of the crown sheet. Phase 1 describes the early stages of impact $\tilde{t} < 1$, which continuously transitions into phase 2, where the crown is formed. The third phase addresses the radial propagation of the crown. Evidently, the different phases are strongly interconnected and certain stages take place at the same time. For this reason it is beneficial to additionally separate the impact region into different zones.

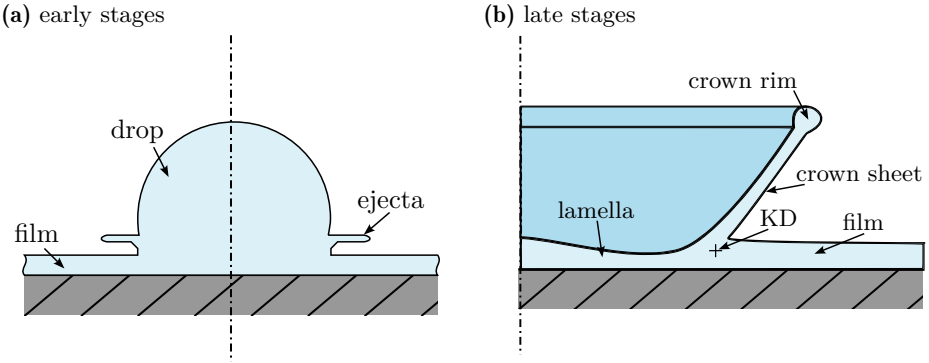

Figure 2.3: Sketch of a drop impacting onto a thin film in the early stage a) and in the late stage b) of drop impact.

Figures 2.3a and 2.3b define the relevant zones for the early stages and the late stages of impact respectively. In the early stages of drop impact, one can distinguish between the drop, the ejecta and the film, as depicted in Fig. 2.3a. In the late stages, the crown can be separated into four main regions, which are shown schematically in Fig. 2.3b (Yarin et al., 2017). The first region is the lamella adjacent to the wall and confined by the crown sheet. The quiescent liquid film outside the crown forms the second region, while the ejected crown-sheet forms the third region. Finally, the crown rim that bounds the crown sheet at its upper end can be defined as the fourth region. Note that the term lamella is used for the total liquid flow confined by the crown sheet adjacent to the wall. In case there are different liquids used, the term lamella describes both wall-film and drop-lamella. When only the lamella from the liquid of the drop or the liquid of the wall-film is meant, they will be referred to as drop lamella or wall-film lamella, respectively.
Due to the high complexity of the drop impact phenomenon, it is convenient to divide it into phases in terms of both temporal and spatial aspects. The subsequent sections follow such a spatio-temporal classification of the drop impact into different phases and zones and discuss the dynamics and characteristics of each phase. A Lagrangian particle located in the drop at the instant of impact could experience the four described phases and zones in a temporal sequence. First, the early stages of drop impact will be considered in Sec. 2.1.4. Afterwards the dynamics of the lamella are discussed for large times after impact in Sec. 2.1.5. In the region where the lamella flow meets the quiescent wall-film, a kinematic discontinuity (KD) forms and causes liquid from the lamella and the wall-film to be propelled into the air, where it forms the crown sheet (Yarin and Weiss, 1995). The evolution of this crown sheet and its formation mechanism will be illuminated in Sec. 2.1.6.

Eventually, the crown becomes unstable and atomizes into secondary drops. The splashing phenomena, possible regime boundaries and mechanisms leading to crown instability are discussed in Sec. 2.1.7.

2.1.4. Early stages of impact

The first interaction of the drop with the liquid film characterises the early stages of impact. These early stages are accompanied by a horizontal jetting of the ejecta, which is schematically represented in Fig. 2.3a. It was first predicted numerically (Yarin et al., 1999) and only afterwards observed experimentally (Thoroddsen, 2002). Interestingly, numerical studies conducted so far focused strongly on the early stages of impact as the short times and the small spatial expansion lead to lower computational costs compared to the later stages. Whereas at the later stages, a larger computational domain and satisfactory spatial resolutions to resolve the thin lamella and crown sheet are necessary. One of these studies by Josserand and Zaleski (2003) revealed that there is both film and drop liquid present in the ejecta. Under certain conditions the ejecta may atomize into secondary droplets (Thoroddsen, 2002), the splash resulting from ejecta atomization is referred to as *prompt splash* (Liang and Mudawar, 2016) or early splash (Okawa et al., 2021). A kindred form of ejecta disintegration into secondary drops has been reported by Thoroddsen et al. (2011), where the ejecta touches the wall-film and subsequently ejects secondary droplets in a slingshot mechanism.
A numerical study of Thoraval et al. (2012) shows that in the early stages of drop impact vortex structures evolve from the shear layer between the film and drop liquid. For high Reynolds numbers $\mathcal{O} = 10^5$ this may lead to the entrapment of bubble rings (Thoraval et al., 2013). These vortices result from the high velocity gradients that accompany the early stages. The complex flow geometry which evolves in the case when the drop impacts onto a wetted substrate makes it difficult to formulate analytical models for this stage.
Analytical approaches to describe the flow at the early stages of impact exist, given that there is no pre-existing film on the substrate. These models are based on the assumption that the flow is incompressible and inertia-dominated. Different authors such as Philippi et al. (2016) and Roisman (2022) use the inviscid character of the flow at early times and describe it as a potential flow around a spreading disk. The drop shape is similar to the shape of a truncated sphere. The radius a_s of the disc can be approximated by the radius of the inter-sectional area of the sphere and the substrate, resulting in $a \approx \sqrt{2\tilde{t}}$. Experiments of Rioboo et al. (2002) have shown good agreement with this approximation. Philippi et al. (2016) predict a similar disc radius of $a \approx \sqrt{3\tilde{t}}$ which is close to the $\sqrt{2\tilde{t}}$ scaling.

Furthermore, Philippi et al. (2016) simulated the flow of a drop impacting onto a dry substrate for short timescales and provided a detailed asymptotic analysis, revealing a self-similar structure of the flow and pressure field. They approximated a boundary layer based on an analogy with the boundary layer which emerges after

a shock (Schlichting and Gersten, 2017), resulting in a spatio-temporal expression to describe a displacement thickness $\tilde{\delta}_1$ as

$$\tilde{\delta}_1 = \frac{2}{\sqrt{\pi}\sqrt{\mathrm{Re}}}\sqrt{\tilde{t} - \tilde{r}^2/3}, \tag{2.7}$$

where $\tilde{r}$ is the radial coordinate normalised by the drop diameter. The resulting analytical model of the velocity field exhibits good agreement with numerical simulations for Reynolds numbers larger than 300.

2.1.5. Dynamics of a spreading lamella

At large times after impact $\tilde{t} \gg 1$ the impacting drop generates a radially expanding flow in a relatively thin liquid sheet. The dynamics of this lamella are the subject of this section.

In the first stages of drop impact onto wetted substrates the flow geometry is complex and challenging to model, however the flow in the thin lamella at relatively large times $\tilde{t} \gg 1$ is well suited for modelling approaches based on remote asymptotics (Yarin et al., 2017).

A remote asymptotic solution which is applicable to the flow in the lamella for this stage and both wetted and dry substrates is obtained by Yarin and Weiss (1995). The solution satisfies the mass and momentum balance for a quasi-two-dimensional, inviscid flow and reads as:

$$\tilde{u}_r = \frac{\tilde{r}}{\tilde{t} + \tilde{\tau}}, \quad \tilde{u}_y = -\frac{2\tilde{y}}{\tilde{t} + \tilde{\tau}} \tag{2.8}$$

Here, $\tilde{u}_r$ and $\tilde{u}_y$ are the non-dimensional, height-averaged velocities in the radial and axial direction, respectively. The non-dimensional radial and axial coordinates are denoted with $\tilde{r}$ and $\tilde{y}$. The linear character of this radial velocity distribution has been confirmed experimentally using particle image velocimetry (PIV) (Smith and Bertola, 2011; Gultekin et al., 2020). The temporal evolution of the uniform, non-dimensional lamella thickness $\tilde{h}_{\mathrm{yw}}$ is then expressed as

$$\tilde{h}_{\mathrm{yw}} = \frac{\tilde{\eta}}{(\tilde{t} + \tilde{\tau})^2}. \tag{2.9}$$

The parameters $\tilde{\tau}$ and $\tilde{\eta}$ that occur in Eqs. (2.8) and (2.9) are constants to be determined by experiments. Those equations have the same form as the solution for a uniformly spreading liquid sheet. A generalized solution for the inviscid flow, providing a non-uniform temporal and radial distribution of the lamella thickness as indicated in Fig. 2.4 is obtained in (Roisman et al., 2009b). In this work, a Gaussian function is used to describe the initial lamella shape, from where the momentum

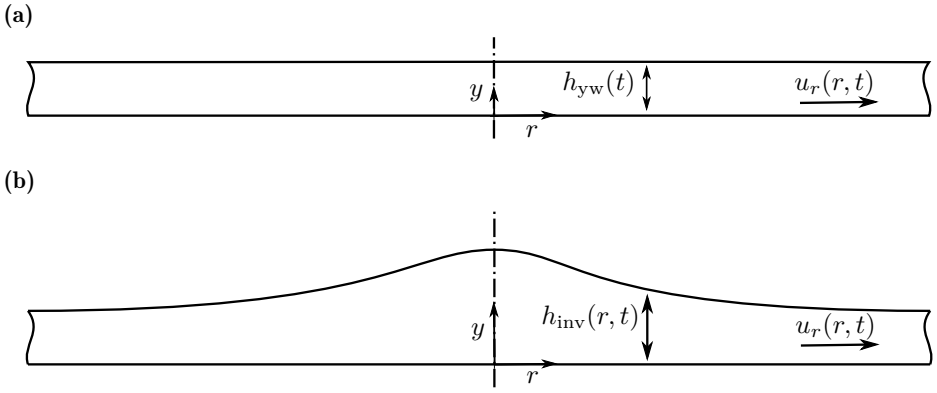

Figure 2.4: Schematic representation of the two-dimensional axisymmetric flow in the lamella for a uniform spreading liquid sheet a) and a non-uniform radial lamella thickness distribution b).

and mass balance of the quasi-two-dimensional flow are solved. The height of the radial film thickness distribution is matched with the remote asymptotic solution in Eq. (2.8) at the impact axis $\tilde{h}_{\mathrm{yw}} = \tilde{h}_{\mathrm{inv}}$ for $\tilde{r} = 0$ resulting in

$$\tilde{h}_{\mathrm{inv}} = \frac{\tilde{\eta}}{(\tilde{t}+\tilde{\tau})^2}\exp\left[-\frac{6\tilde{\eta}\tilde{r}^2}{(\tilde{t}+\tilde{\tau})^2}\right], \quad \tilde{\eta} = 0.39, \tilde{\tau} = 0.25. \tag{2.10}$$

Here, the parameters $\tilde{\eta}$ and $\tilde{\tau}$ are obtained from numerical simulations for $\mathrm{We} > 70$ and $\mathrm{Re} > 30$ of a drop impacting onto a dry substrate. The velocity distribution presented in Eq. (2.8) is used in both studies of Yarin and Weiss (1995) and Roisman et al. (2009b). However, the approach to describe the flow in the lamella with remote asymptotics is only valid for large times $\tilde{t} \gg 1$. In the initial stages of drop impact the flow is more complex, as described for instance in Thoraval et al. (2012) and Thoraval et al. (2013), vortex structures have been observed to emerge in the lamella which may also influence the flow at later times of the impact. The discussed theories in Eqs.(2.8),(2.9) and (2.12) are only applicable when the influence of viscous forces and surface tension are negligibly small. This is the case when the lamella curvature expressed by the parameter $h^{-}1\partial h/\partial r$ is small and the height of the lamella is much bigger than the viscous boundary layer (Roisman et al., 2009b).

The effect of the viscous boundary layer on the flow in a spreading liquid sheet is considered by Roisman (2009a), where a full solution of the Navier-Stokes equations is provided. In this study, the boundary-layer thickness δ_{BL} is defined as the distance to the substrate where the radial velocity component of the boundary-

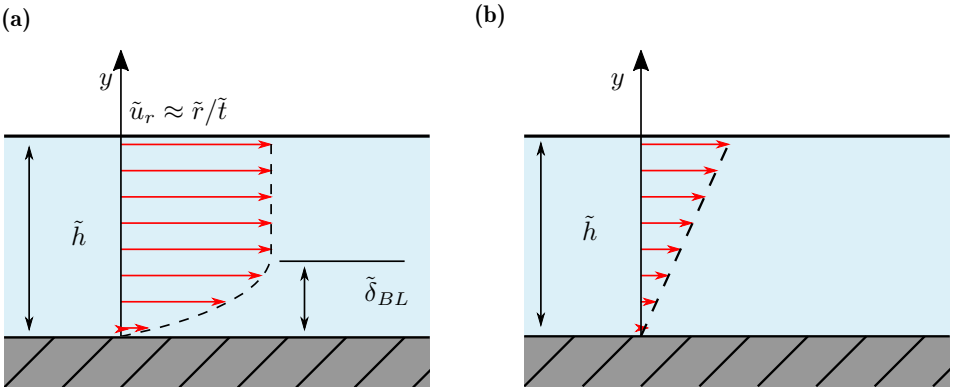

Figure 2.5: Sketch of the flow in a spreading viscous sheet for a) times smaller than the viscous time $\tilde{t} < \tilde{t}_\nu$ and b) times larger than the viscous time $\tilde{t} > \tilde{t}_\nu$ after Roisman (2009a).

layer flow has reached 99 % of the magnitude of the radial velocity component of the inviscid flow. Based on the analytical solution of the Navier-Stokes equations and numerical simulations, the temporal evolution of the uniform boundary-layer thickness is found to be $\delta_{BL} = 1.88\sqrt{t\nu}$ which can be expressed as

$$\tilde{\delta}_{BL} = 1.88\sqrt{\tilde{t}/\mathrm{Re}} \tag{2.11}$$

in non dimensional form. This relation is then used to estimate the asymptotic value of film thickness formed by a normal drop impact onto a solid substrate.

An essential conclusion of the study is that the characteristic time $\tilde{t}_\nu$, when the boundary layer intersects with the interface of the drop lamella, separates two regimes of lamella flow. For times $\tilde{t} < \tilde{t}_\nu$, the flow consists of an inviscid part and a growing viscous boundary layer beneath, as depicted in Fig. 2.5a. The total film thickness $\tilde{h}$ can be expressed as a superposition of the viscous and inviscid contribution $\tilde{h}_\nu$ and $\tilde{h}_{\mathrm{inv}}$ defined by

$$\tilde{h} = \tilde{h}_{\mathrm{inv}} + \frac{4}{5}\gamma\tilde{t}^{1/2}\mathrm{Re}^{-1/2}, \gamma \approx 0.626. \tag{2.12}$$

In this relation γ is a dimensionless constant that is numerically determined in Roisman et al. (2009b). The instant $\tilde{t}_\nu$ can be estimated by equating the boundary-layer height and the lamella thickness $\tilde{h}(\tilde{t_\nu}) = \tilde{\delta}_{\mathrm{BL}}$ resulting in

$$\tilde{t}_\nu \approx \frac{\tilde{\eta}^{2/5}}{(1.88 - 0.8\gamma)^{2/5}}\mathrm{Re}^{1/5}. \tag{2.13}$$

For times larger than the viscous time $\tilde{t} > \tilde{t}_\nu$, the flow is dominated by a balance of inertial and viscous forces. When viscous effects have dissipated all the kinetic energy, the radial velocity component vanishes and consequently, the film thickness reaches an asymptotic value $\tilde{h}_{\mathrm{res}}$ which can be expressed by

$$h_{\mathrm{res}} = A\mathrm{Re}^{-2/5}. \tag{2.14}$$

The prefactor A is a constant which is equal to $A = 0.79$ for drop impact onto solid surfaces. (Roisman, 2009a)
Furthermore, the impact of a drop impacting onto a substrate wetted by a pre-existing film with a thickness $\tilde{\delta} = \mathcal{O}(1)$ was experimentally investigated by van Hinsberg et al. (2010). They found that the minimum distance from the crater to the substrate can also be described by Eq. (2.14) when A is a function of $\tilde{\delta}$. The resulting empirical approximation of A is

$$A = 0.098\tilde{\delta}^{4.0413} + 0.79. \tag{2.15}$$

At present, there is a lack of data on the residual film thickness for drop impact onto thin films that has also been recognized in other studies (Lamanna et al., 2022). A detailed physical analysis that goes beyond the creation of a fit, as in Eq. (2.15), does not yet exist. Furthermore, the influence of differing fluid parameters in drop and liquid film on the formation of the residual layer have never been investigated. In Chapter 4, such measurements are provided for a large variety of impact parameters as a part of this dissertation. Additionally, a theory predicting the residual film thickness is developed that takes the influence of the preexisting liquid film into account and incorporates the influence of different fluid properties, such as the viscosity ratio κ_*. The next section covers the flow at the borders of the impact region where the lamella meets the quiescent wall-film and the crown sheet emerges. The formation mechanism and the propagation of the crown sheet will be discussed.

2.1.6. Characteristics of crown formation and evolution

In the description of the lamella flow, there are analogies between the impact onto wetted and dry substrates. However, significant differences can be identified when observing the flow at the borders of the impact region where the lamella flow meets the quiescent wall-film. In contrast to the impact onto a wetted substrate, a drop impacting onto a dry substrate requires relatively high impact energy to result in crown formation. Typically the energy is so high that a crown formation is accompanied by atomization into secondary droplets. Hence, a crown formation is usually part of a splash (Josserand and Thoroddsen, 2016). While a splash onto dry substrates can be expected for $K \gtrsim 3000$ (Josserand and Thoroddsen, 2016), a relatively small number of $K \approx 400$ is sufficient for the formation of a crown in case of the drop impact onto a wetted substrate. This discrepancy can be attributed

to different crown formation mechanisms in the dry and wet scenarios. While the formation of a crown on dry substrates is mainly attributed to aerodynamics forces (Riboux and Gordillo, 2014), the formation of the crown following the drop impact onto a wetted substrate can be attributed to the interaction of the radially expanding lamella flow with the quiescent wall-film. As indicated in Fig.2.6, the radially expanding lamella flow meets the quiescent wall-film at the base of the crown. Due to the abrupt change of velocity of the lamella inside the crown and the wall-film outside the crown in the region of the crown base, a kinematic discontinuity (KD) is created (Yarin and Weiss, 1995). As a result, high pressure regions form in this region (Coppola et al., 2011) and liquid from both the lamella and the wall-film are propelled into the air, where they form the crown sheet. Accordingly, the KD propagates in the radial direction at the base of the crown sheet. The KD has been observed in experimental (Ninomiya and Iwamoto, 2011) and numerical studies (Coppola et al., 2011) and is widely accepted as the formation mechanism of the crown (Trujillo and Lee, 2001; Roisman and Tropea, 2002; Yarin, 2006; Lamanna et al., 2022).

A theoretical approach to describe the flow near the KD can be found in Yarin and Weiss (1995). Considering an inviscid flow and neglecting forces related to surface tension, the mass and momentum equations can be formulated according to Eqs. (2.16) and (2.17). The control volume which moves with the KD can be drawn as depicted in Fig. 2.6. The resulting mass conservation equation can be formulated as (Roisman and Tropea, 2002)

$$h_l \left(U_1 - U_{\mathrm{KD}}\vec{e}_n'\right) \cdot \vec{e}_n' - H_{\mathrm{f0}} \left(U_2 - U_{\mathrm{KD}}\vec{e}_n'\right) \cdot \vec{e}_n' = Q, \tag{2.16}$$

while the momentum equation results in

$$\begin{aligned} &h_l \left[\left(U_1 - U_{\mathrm{KD}}\vec{e}_n'\right) \cdot \vec{e}_n'\right] \left(U_1 - U_{\mathrm{KD}}\vec{e}_n'\right) - H_{\mathrm{f0}} \left[\left(U_2 - U_{\mathrm{KD}}\vec{e}_n'\right) \cdot \vec{e}_n'\right] \left(U_2 - U_{\mathrm{KD}}\vec{e}_n'\right) \\ &= Q \left(U_d - U_{\mathrm{KD}}\vec{e}_n'\right). \end{aligned} \tag{2.17}$$

Here, U_{KD} is the velocity of the KD, which propagates along the wall in $\vec{e}_n'$ direction. The flow propelled into the crown sheet is included in the form of a mass sink Q. Neglecting viscous losses or mass accumulations and transient effects in the KD, the velocity U_B of the liquid leaving the KD is equal to the centre of mass velocity

$$\vec{U}_B = \frac{\vec{U}_1 h_l + \vec{U}_2 H_{\mathrm{f0}}}{h_l + H_{\mathrm{f0}}}. \tag{2.18}$$

Combining Eqs. (2.16), (2.17) and (2.18), the velocity of the KD, as well as the specific volume flux into the KD, can be expressed as:

$$U_{\mathrm{KD}} = \frac{1}{2}(U_1 + U_2)\vec{e}_n' \qquad Q = \frac{1}{2}(h_l + H_{\mathrm{f0}})(U_1 - U_2)\vec{e}_n' \tag{2.19}$$

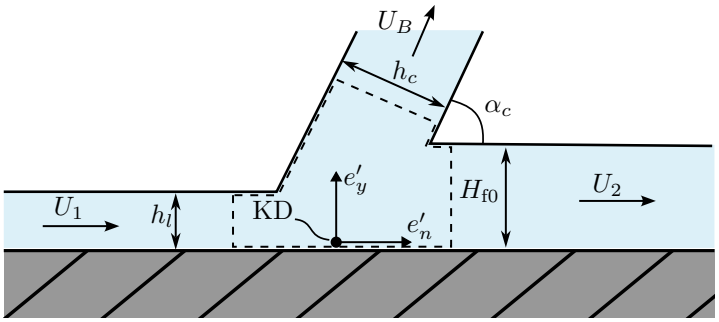

Figure 2.6: Schematic representation of the flow at the kinematic discontinuity (KD), adopted from Roisman and Tropea (2002).

For drop impact onto quiescent films, the velocity $\vec{U}_2$ vanishes and the propagation of the KD in radial direction will be approximated by the following differential equation

$$\frac{\partial r_{\mathrm{KD}}(\zeta)}{\partial t} = \frac{1}{2} U_1(r,t), \tag{2.20}$$

where ζ is a Lagrangian location parameter. To solve this equation Yarin and Weiss (1995) used an asymptotic solution in parametric form obtained in Whitham (1974), which has the form

$$U_1 = F(\zeta), \qquad x = F(\zeta)t + \zeta. \tag{2.21}$$

The function $F(\zeta)$ describes the radial velocity distribution at the initial stage of impact. Evaluating Eqs. (2.20) and (2.21) at the location $r = r_{\mathrm{KD}}$, the temporal evolution of the discontinuity radius can be determined in its dimensionless form as

$$\tilde{r}_{\mathrm{KD}} = \beta\sqrt{\tilde{t} + \tilde{\tau}}. \tag{2.22}$$

Here, β and $\tilde{\tau}$ are dimensionless constants that describe the integral characteristics of the radial velocity distribution at the initial stage of impact and are to be determined experimentally. The radial position of the kinematic discontinuity can be interpreted as the radius of the crown at its base $r_{\mathrm{KD}} = r_c$.

Based on a comparison with data on the radial expansion of a crown obtained from Levin and Hobbs (1971) the parameter $\tilde{\tau}$ is found to be $\tilde{\tau} \approx 0.0172$ and a empirical correlation describing the parameter β as a function of the initial film thickness $\beta = (2/(3\tilde{\delta}))^{0.25}$. Many subsequent studies report that the radius at the crown base follows the general relation

$$\tilde{r}_c = C_{\mathrm{r}}(\tilde{t} - \tilde{\tau})^{n_{\mathrm{r}}}. \tag{2.23}$$

A summary of those correlations is provided by Liang and Mudawar (2016), showing that the square-root-dependence predicted in Eq. (2.22) is confirmed by most of the studies. Only some document slightly lower exponents of $0.406 < n < 0.469$ (Rieber and Frohn, 1999; Guo et al., 2014).

The influence of initial film thickness on the spreading is still controversial. Some studies report that a changing film thickness has a weak influence on the spreading diameter (Cossali et al., 2004; Lee et al., 2011) while others state that reducing $\tilde{\delta}$ increases crown diameter (Trujillo and Lee, 2001; Liang et al., 2014b). The numerical investigation of Mukherjee and Abraham (2007) revealed contrary effects for different film thickness ranges. While for thin films with $\tilde{\delta} < 0.25$ increasing the film thickness increases the crown diameter, for thicker films in the range $0.25 < \tilde{\delta} < 2$ the crown diameter decreases with increasing film thickness. Gao and Li (2015) present a modified version of Eq. (2.22) where both $\tilde{\tau}$ and β depend on the film thickness while additionally an empirical parameter λ_s is introduced accounting for momentum losses. Recently, an expansion of the inviscid solution of Yarin and Weiss (1995) was published (Lamanna et al., 2022), where the impact of the drop is interpreted as a decaying transient stagnation point flow. Furthermore, the authors considered the boundary layer and incorporated an integral correction for momentum loss due to viscous effects in the expression for the crown radius, which reads

$$\tilde{r}_\mathrm{c} = \alpha_L \lambda_1 \sqrt{\lambda_i} \sqrt{\tilde{t} - \tilde{\tau}_\mathrm{ini}} + \tilde{R}_\mathrm{c,ini}. \tag{2.24}$$

Hereby, α_L is a dimensionless constant, λ_1 is a time-dependent function incorporating viscous losses, $\sqrt{\lambda_i}$ represents the losses due to deformation in the initial stage of impact and $\tilde{\tau}_\mathrm{ini}$ as well as $\tilde{R}_\mathrm{c,ini}$ can be interpreted as a temporal and radial offset of a fully formed crown.

The influence of gravity and capillary effects is not negligible for drop impact onto thick films (Yarin et al., 2017). Their influence on the evolution of the crown radius is investigated in Roisman et al. (2008). Based on Eq. (2.22) and additionally incorporating gravity and capillary effects, a relation for $\tilde{r}_c$ is obtained that predicts crown expansion and its receding

$$\tilde{r}_\mathrm{c} = \sqrt{\beta T - \left(\frac{4G\tilde{\delta}^{1/2}}{\beta G^{1/2} We - 2\tilde{\delta}^{1/2}} + \frac{4}{We} + \frac{\tilde{\delta}^2}{\mathrm{Fr}} \right) \frac{T^2}{\tilde{\delta}}}. \tag{2.25}$$

$$T = \tilde{t} + \tilde{\tau}, \tag{2.26}$$

$$G = \frac{4}{\mathrm{We} + \frac{\tilde{\delta}^2}{\mathrm{Fr}}}, \quad \mathrm{Fr} = \frac{U_0^2}{g D_0} \tag{2.27}$$

$$\tag{2.28}$$

In this relation Fr is the Froude number and β corresponds to the parameter β in Eq. (2.22). The drop impact is investigated for dimensionless film thicknesses $\tilde{\delta}$ in the range of $0.5 < \tilde{\delta} < 2$. For this range empirical correlation for the dimensionless parameters β, $\tilde{\tau}$ are obtained as

$$\tilde{\tau} = -0.8\tilde{\delta}^{1.7}, \beta = 0.62\tilde{\delta}^{0.33}. \tag{2.29}$$

Besides the radial spreading of the crown, the shape of the crown has been a subject of research. Characteristic quantities that describe the crown shape are its height and angle a_c.

Experimental investigation of Wang and Chen (2000) as well as Fedorchenko and Wang (2004) reveal that the crown angle for $\tilde{\delta} > 0.25$ is ca. 90°, while it reduces with reducing film thickness for thinner films. Roisman and Tropea (2002) generalized the theory of Yarin and Weiss (1995) for arbitrary velocity vectors resulting in an analytical model predicting the shape of the crown. The model neglects viscous losses but considers inertial effects and surface tension. Furthermore, a relation for the crown angle α_c is derived that depends on density, surface tension, as well as the film heights inside and outside of the crown and the velocity vectors $\vec{U}_1$ and $\vec{U}_2$ at the crown base.

Numerical simulations show that for the same liquids in film and drop and relatively thin films ($\tilde{\delta} = 0.15$), the viscosity has an influence on the crown shape, resulting in smaller angles for higher viscosity (Josserand and Zaleski, 2003; Liang et al., 2014b). Hence, also effects of viscosity would need to be considered in order to achieve a full understanding of the situation at the crown base. Recent studies, temporally resolving the evolution of the crown angle (Gao and Li, 2015; Geppert, 2019; Bernard et al., 2020), show that the angle of the crown is not constant but a non-monotonic function of time. Some studies even observe cone-shaped crowns where the diameter at the crown base is significantly larger than the diameter of its top. These types of crowns, observed for elevated Weber numbers ($We > 1100$, $\tilde{\delta} > 0.2$), may also lead to the entrapment of large bubbles (Geppert et al., 2017). Those shapes have not yet been predicted by any analytical model (Liang and Mudawar, 2016).

Moreover, the shape of the crown can be expressed in the form of its height. Different studies report that, analogously to the crown angle, the crown height is more sensitive to the film thickness for impact on thinner films $\tilde{\delta} < 0.25$ (R. Davidson, 2002; Šikalo and Ganić, 2006). For thicker films and deep pool impact, the crown height depends solely on the Weber number, a relation of which is quantified in multiple empirical correlations (Cossali et al., 2004; Asadi and Panahi, 2011). Analytical predictions of the crown height from Roisman and Tropea (2002) match well with the results of Cossali et al. (1997) for a relatively thin film thickness of $\tilde{\delta} = 0.29$, but fails to predict the height for drop impact on thicker films $\tilde{\delta} = [0.67, 1.13]$ of the subsequent experiments (Cossali et al., 2004). This supplements the conclusion that for different regimes of initial film thickness, the crown height is determined by different factors.

Generally, the height of the crown is determined by the inertia of the impact, the crown angle and surface tension. At the rim binding the crown sheet at its free end, the inertia of the liquid flowing into the rim is in balance with surface tension (Roisman, 2010; Yarin et al., 2017). The relative velocity of the rim to the liquid sheet can be expressed by the well-known relation of Taylor (1959) and Culick (1960) as

$$u_{\mathrm{tc}} = \sqrt{\frac{2\sigma}{h_c \rho}}, \tag{2.30}$$

where u_{tc} is the velocity of the rim relative to the liquid sheet and h_c is the liquid sheet thickness. The height of the crown is thus strongly interconnected with the velocity and the thickness of the crown sheet. Although the thickness of the crown sheet is an important parameter for predicting the crown height or predicting splash by instability analysis, there is little experimental data on this quantity. Only some studies, for example Cossali et al. (2004), provide coarse approximations of the "normal" crown-sheet-thickness by analysing the shadow cast by the crown sheet from a bottom perspective. In the scope of this dissertation a method is developed where the rim of an artificially induced rupture in the crown sheet is tracked and the Taylor-Culick relation is utilised to estimate the crown sheet thickness from the rupture propagation velocity. The method is presented in Chapter 3 and the results of which are shown in Chapter 5.

2.1.7. Splashing phenomena

The relevance of the splashing phenomena to many industrial and technical applications has motivated numerous studies in this field. Consequently, much effort has been put into analysing the mechanisms leading to splashing, characterising thresholds for its occurrence, or characterising the secondary drops ejected in a splash. This subsection will give a brief overview of the current state of the art related to splashing phenomena after the drop impact onto wetted walls.

In Fig. 2.7, different types of splash resulting from a drop impact onto a liquid film are presented. *Prompt splash* (Fig. 2.7a), also referred to as early splash, describes a scenario in which the ejecta atomizes in the early stages of drop impact. This type of splash occurs mainly for low Ohnesorge numbers (i.e. low viscosity liquids) and results in the ejection of relatively small and fast secondary droplets (Cossali et al., 1997; Liang et al., 2013; Okawa et al., 2021).

The *corona splash* (Fig. 2.7b) is also referred to as late splash. Compared to the prompt splash, it occurs on a slightly longer timescale. In some situations, a prompt splash even precedes a corona splash. The corona splash is attributed to the instability of the crown rim, which forms finger-like jets that finally break up into secondary droplets. To identify the factors influencing the rim stability, Roisman (2010) analyzed the azimuthal and transverse instability of a rim bound by a planar liquid sheet and found that the fastest growing wavenumbers are very similar to the respective Rayleigh-Plateau and Rayleigh-Taylor instabilities. The growth rate

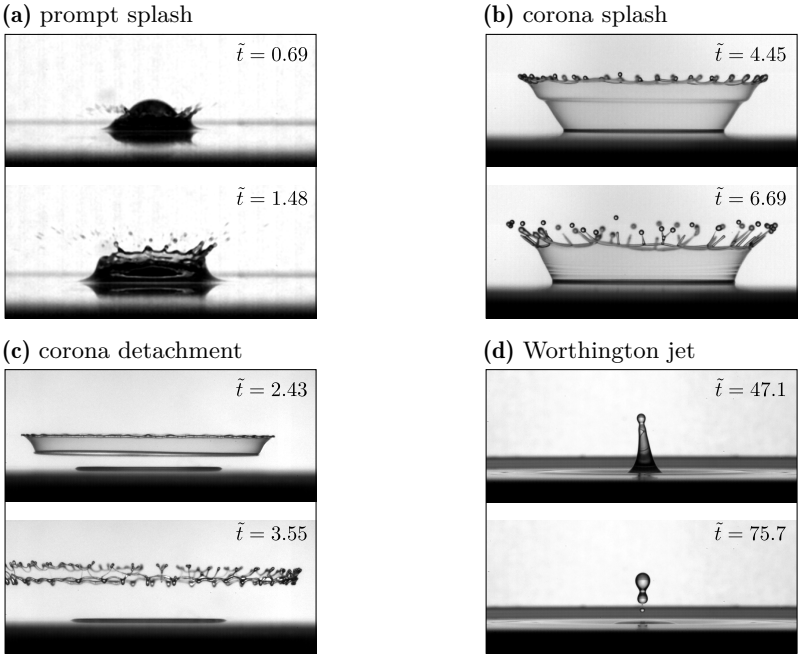

Figure 2.7: Snapshots from experiments showing different types of splash at two consecutive instants: a) prompt splash (We = 263, Re = 6505, $\tilde{\delta}$ = 0.315); b) corona splash (We = 1230, Re = 612, $\tilde{\delta} = 0.042$); c) corona detachment (We = 915, Re = 600, $\tilde{\delta} = 0.018$); d) Worthington jet (We = 701, Re = 900, $\tilde{\delta} = 0.333$).

of the disturbance depends on all parameters of the problem but mostly on the rim deceleration. The predicted growth rates agree with the results from Agbaglah et al. (2013), who observed a combination of Rayleigh-Taylor and Rayleigh-Plateau instability in the crown.

The almost simultaneous detachment of the crown from the wall-film at the crown base is referred to as *corona detachment* (CD), which is shown in Fig. 2.7c. Geppert (2019) developed correlations based on We and $\tilde{\delta}$ to confine the regime of CD. Although this phenomenon has been observed in various studies (Chen et al., 2017; Kittel, 2019; Geppert, 2019), a detailed analysis of the hydrodynamics leading to this phenomenon is still missing. A self-consistent model predicting the instant of the breakup is presented in Chapter 5.

For drop impact onto relatively thick films a *Worthington jet* can be observed, where gravity and surface tension leads to a receding of the crown at large times after impact. The receding flow collides at the impact axis, causing the Worthington jet to emerge. Once propelled into the air, the jet may become unstable and eject secondary droplets (Yarin, 2006).

There are kindred types of splashing related to different fluid properties in the film and drop liquid. Marangoni holes that form due to a different surface tension in drop and film have been reported for miscible liquids (Thoroddsen et al., 2011; Aljedaani et al., 2018; Geppert, 2019). For a relatively narrow range of impact parameters, apex jetting has been observed. This phenomenon requires a more viscous drop than the film; at the same time surface tension and inertia need to be low. During apex jetting the ejecta adheres to the drop and travels along its periphery until it collides at the apex of the drop, causing a high-speed vertical jetting (Marston and Thoroddsen, 2008). In this section, it is shown that there are various phenomena that lead to a splash.
The following section addresses the delimitation of the splashing regime on the basis of threshold parameters.

Splashing threshold

Much of the research has focused on defining general parameters that can predict the occurrence of a splash based on impact parameters and fluid properties. Generally, viscous forces and surface tension have been identified to inhibit splashing, while inertia tends to promote splashing (Motzkus et al., 2011). Some studies describe the splashing threshold based on a critical Weber number. However, because surface tension and viscosity affect the splashing, the Weber number alone is insufficient to map a universal threshold (Liang and Mudawar, 2016). A widely accepted parameter, used to describe the splashing threshold is the K number, which incorporates viscous and inertial forces as well as effects of surface tension in a single parameter. In addition to the form shown in Eq. (2.4) ($K = \mathrm{We}^{0.8}\mathrm{Re}^{0.4}$), many alternative formulations incorporate the We and Oh or Re numbers in the general form

$$K = A_K \mathrm{We}^a \mathrm{Oh}^b. \tag{2.31}$$

A summary of K type correlations to describe the splashing threshold can be found in comprehensive reviews of Moreira et al. (2010) and Liang and Mudawar (2016). A comparative study of Motzkus et al. (2011) shows that many of the K based thresholds fail to predict splash when they are extrapolated out of the range of parameters they are obtained in.

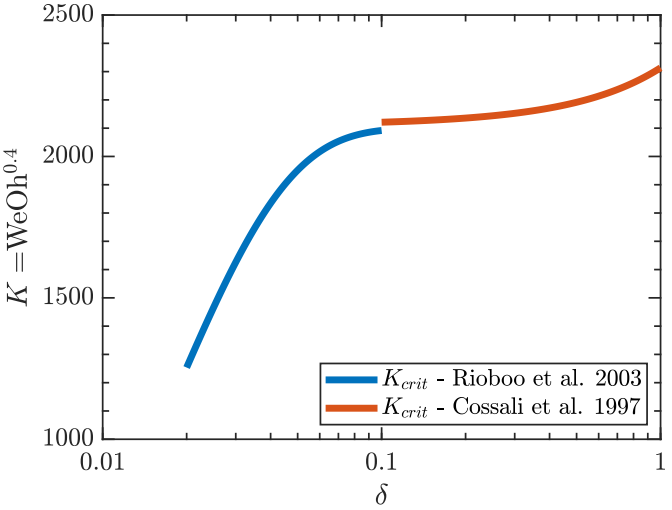

Figure 2.8: Critical splashing threshold as a function of dimensionless film thickness obtained from Cossali et al. (1997) and data of Rioboo et al. (2002).

Moreover, the influence of the initial film thickness on the splashing threshold is still controversial. While some studies observe a direct effect of $\tilde{\delta}$ on the splashing threshold (Rioboo et al., 2003; Cossali et al., 1997; Motzkus et al., 2011; Geppert, 2019), others report a very weak or no effect (Wang and Chen, 2000; Okawa et al., 2006; Okawa et al., 2008).

In a recent publication, Okawa et al. (2021) investigated the splashing threshold for $(0.2 < \tilde{\delta} < 0.5)$ and water-ethanol solutions of different concentrations. They differentiate between prompt and corona splash and propose different correlations for each phenomenon. The correlation for corona splash depends on the initial film thickness, while the correlation for prompt splash is independent of this parameter.

Figure 2.8 shows two representative K number type correlations for the splashing threshold. One obtained from Cossali et al. (1997), valid for $0.1 < \tilde{\delta} < 0.5$, agrees rather well with data and correlations obtained in other studies in this parameter range (Tropea and Roisman, 2000; Motzkus et al., 2011; Geppert, 2019). It is described by

$$K_{\mathrm{crit}} = 2100 + 5880\tilde{\delta}^{1.44} \quad (0.1 < \tilde{\delta} < 1). \tag{2.32}$$

The second correlation covers thin films for $\tilde{\delta} < 0.1$ and is obtained from data of Rioboo et al. (2002) by Kittel (2019) as

$$K_{\mathrm{crit}} = 2100 - 2700\exp(-58\tilde{\delta}) \quad (0.01 < \tilde{\delta} < 0.1). \tag{2.33}$$

It becomes apparent from the figure that K_{crit} rapidly decreases with decreasing film thickness for $\tilde{\delta} < 0.1$. Rioboo et al. (2002) attribute this behaviour to effects of surface roughness. The experiments described in Chapters 4 and 5 are conducted in a similar range for $\tilde{\delta} < 0.1$ and reveal that crown stretching and the attributed thinning of the crown sheet might be a reason for this effect. For completeness, it is mentioned here that the splash of a drop impacting onto a dry substrate is a totally different phenomenon and therefore not included in this overview. The interested reader might be referred to the review of Josserand and Thoroddsen (2016) for more information on this topic.

Secondary droplets

When the drop impact results in a splash, secondary droplets are ejected in the process. Their relevance to numerous technical and industrial applications has motivated various studies that focus on the characterisation of the main parameters of secondary droplets. Those main parameters are the number, velocity and diameter of secondary droplets.

For the characterisation of the size of secondary droplets, it has to be considered that the droplets are not produced with a uniform diameter but are spread over a spectrum. Commonly used distributions to describe the spectrum of secondary drop diameter, but also the velocity, are log-normal distributions (Lefebvre and McDonell, 2017). Characteristic parameters such as the arithmetic average diameter $\bar{d}_{\mathrm{sec}}$ or the mean velocity components $\bar{u}_{i,\mathrm{sec}}$ can be formulated to condense the spectrum to a single parameter. Other relevant quantities are the number of ejected droplets N_{sec} or the total mass of ejected drops m_{sec}.

Investigating the effects of surface tension and viscosity on the secondary droplet diameter, experimental studies show that increasing the surface tension or the viscosity has a similar effect on secondary droplets, which increase in diameter but decrease in total number (Vander Wal et al., 2006; Motzkus et al., 2011). Furthermore, decreasing the initial film thickness is found to increase the number of secondary droplets (Samenfink et al., 1999), while the ejection angle reduces (Allen, 1988).

Semi-empirical correlations describing the normalized diameter of ejected secondary droplets over time can be found in the form

$$\bar{d}_{\mathrm{sec}}/D_0 = C_s \tilde{t}_s^{\,n}, \tag{2.34}$$

where C_s and n_s are empirically determined constants which are sensitive to the Weber number (Cossali et al., 2004; Guildenbecher et al., 2014; Guildenbecher et al., 2016; Wu et al., 2020).

Similar power law fittings in the form $\bar{u}_{i,\mathrm{sec}}/U_0 = q\tilde{t}^{\,m}$ are formulated for the individual velocity components of secondary droplets normalized by the impact velocity U_0 (Wu et al., 2020; Guildenbecher et al., 2014). Recently, Wu et al. (2020)

used a stereoscopic shadowgraphy setup to obtain three-dimensional trajectories of secondary droplets resulting from drop impact onto thin films ($\tilde{\delta} < 0.035$). Similar to Guildenbecher et al. (2014) and Guildenbecher et al. (2016), they investigate secondary droplets in a cylindrical measurement volume providing correlations for the average droplet diameter and velocities. Their measurements reveal that corona detachment leads to a significant increase in the number of secondary droplets accompanied by a slight increase in the ejected mass. These results agree well with the observations made in Geppert (2019).

Other studies describe the total number of ejected drops as a function of the K parameter and initial film thickness (Okawa et al., 2006) or as a function of only the initial film thickness (Stow and Stainer, 1977). Okawa et al. (2006) report that the ejected mass of secondary droplets does not depend on the initial film thickness, contrary to their quantity. They observe that when the film thickness is reduced, the secondary droplet diameter does decrease, while the total number of secondary droplets does increase. Consequently, they argue that these effects cancel each other out. Roisman et al. (2006) provided phase Doppler (PD) measurements of secondary droplets forming during a spray impact onto a solid substrate and showed that the diameter of secondary drops scales well with the thickness of the viscous boundary layer.

$$\bar{d}_{\mathrm{sec}}/\bar{d}_{\mathrm{prim}} = \mathrm{Re}^{-1/2}. \tag{2.35}$$

where, $\bar{d}_{\mathrm{prim}}$ is the average diameter of the primary spray.

Various empirical correlations to describe the main parameters of secondary droplets for different impact parameters can be found in the literature. Comprehensive summaries can be found, for instance, in reviews of Moreira et al. (2010) and Liang and Mudawar (2016), underlining that applying these correlations out of their validation range is not recommended.

This limitation to their validation range underlines the high complexity of the phenomenon and suggests a lack of knowledge about vital influences. Multiple factors, such as the inertia of the impact, the initial film thickness, but also liquid properties such as surface tension and viscosity, influence the outcome of a splash. Therefore, it is crucial to consider the splashing mechanism to perform reliable predictions on the parameters of secondary droplets. A further parameter that is often attributed to influence the size of secondary droplets is the thickness of the crown sheet (Chen et al., 2017; Geppert et al., 2017). However experimental data on this topic is seldom acquired and consequently rare. Measurements of the crown sheet thickness that may contribute to a better understanding of the secondary droplet formation in future are presented in Chapter 5.

2.1.8. Two-component drop-wall-film interactions

While much of the previous research focuses on drop impact situations where the drop and the film are of the same liquid, the hydrodynamics of drop impact with differing liquids is less intensively investigated. However, the interest in

two-component drop-wall-film interactions has risen over the last years. Effects of interfacial tension (Bernard et al., 2021), Marangoni effects (Aljedaani et al., 2018), but also effects related to the differing viscosity (Banks et al., 2013) of the fluids of drop and wall-film affect the morphology and outcome of the drop impact. Investigating two-component drop impact may not only identify those effects but also provide insight into which role the liquid of the drop and crown play individually in the complex drop-wall-film interaction.

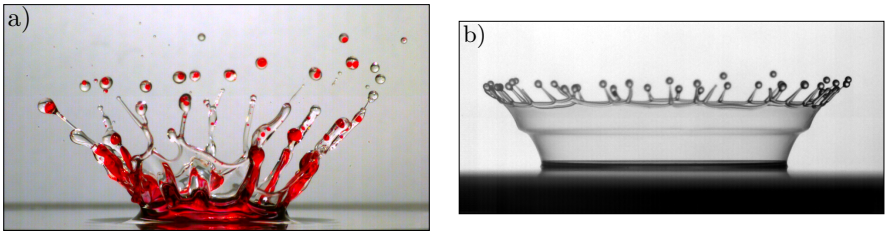

Figure 2.9: Snapshots from experiments of a) a red coloured water droplet impacting onto a silicone oil film (We = 384, Re= 9473, $\tilde{\delta} = 0.2$) and b) silicone oil drop of high viscosity ($\nu = 20$ mm^2/s, We=1257, Re=354) impacting onto a film of lower viscosity ($\nu = 5$ mm^2/s; $\tilde{\delta} = 0.037$).

When the liquids in drop and film have different chemical potentials, an interface forms between both liquids during the impact. In the case of miscible liquids, the interface vanishes over time with ongoing diffusion (Smith et al., 1981). However, since the time scales of diffusion are smaller than the timescale of drop impact, they are assumed to exist over the entire process of impact (Chen et al., 2017; Bernard et al., 2021). Previous studies on two-component drop impact focus on the effect of different liquid properties on the drop impact morphology, the splashing threshold, and characterising the outcome in terms of secondary droplets. In Fig. 2.9, two snapshots of experiments, one from immiscible liquids and one for miscible liquids with similar surface tension but differing viscosity, are presented, illustrating the complexity of two-component drop impact. Different morphology of the crown breakup is observed depending on whether the liquids in the drop and film are miscible. Thoroddsen et al. (2011) and Aljedaani et al. (2018) investigated highly viscous drops impacting on thin ethanol film and observed that, first, the crown sheet is bisected in ethanol and an oil layer. Second, the ejected ethanol drops falling back on the crown sheet cause Marangoni holes to form that in turn cause the crown to disintegrate in a net-like structure. This phenomenon could not be observed for immiscible liquids. Further studies of Chen et al. (2017) and Wu et al. (2021) investigated the effect of miscible and immiscible drop-wall-film combinations and observed different morphology for each category. While for immiscible systems, the breakup is dominated by a fingering instability, for miscible systems, hole formation and corona detachment are more prominent (Chen et al., 2017).

(Bernard et al., 2021) investigated two-component drop impact with miscible and immiscible liquid combinations and found that the interfacial tension between the drop and film liquid in the crown wall stores parts of the impact energy. This leads to larger crown diameters and a higher tendency to splash when the interfacial tension is low.

Other studies focus on defining a splashing threshold. For the drop impact liquids with a different degree of miscibility Kittel et al. (2018) identified three regions of splashing. Region one and two are defined for situations where the viscosity in drop and film strongly differ. In region I, the drop is significantly more viscid than the film, while in region II, the film has a significantly higher viscosity. In those regions, the K number based on the liquid properties of the drop K_d or the film K_f describe the outcome of the impact, respectively. An alternative K number is formulated for the intermediate region III

$$K^\star = \mathrm{Re}^{1/4}\mathrm{We}^{\star 1/2}, \quad \mathrm{We}^\star = \frac{(\rho_f + \rho_d) D_0 U_0^2}{2\min(\sigma_d; \sigma_f),} \tag{2.36}$$

is formulated, where an average density and the minimum of both surface tensions are used to calculate $\mathrm{We}^\star$. The critical threshold based on the $K^\star$ number is then found to be a function of only the viscosity ratio $K^\star = f((\kappa_* - 1)/\kappa_*^{3/5})$.

Shaikh et al. (2018) investigated the impact of immiscible liquids using water and oil combinations as already proposed by Marston and Thoroddsen (2008). They characterise the outcome based on composite Reynolds and Weber numbers Re_f and We_f, where the diameter and the velocity of the drop are used as length and velocity scale, but viscosity, surface tension and density of the film liquid are used. The resulting splashing threshold takes the form ${\mathrm{Re_f}}^{1/4}{\mathrm{We_f}}^{1/2} = 100$. Furthermore, evaluating the size of sessile secondary droplets that have landed on the film, it is found that the number of secondary droplets is sensitive to initial film thickness and viscosity while the modal diameter d_{mod} scales with the Weber number $d_{\mathrm{mod}} \sim We^{-1/4}$.

Further studies on the characterisation of secondary droplets resulting from two-component drop impact are provided by Geppert et al. (2017) and Terzis et al. (2019) . Geppert et al. investigate hypsin/hexadecane systems and develop semi-empirical correlations for the drop diameter and the total number of ejected droplets depending on the film thickness and Weber number. Terzis et al. (2019) provided similar correlations for urea water solutions in different concentrations, additionally considering the ratio of dynamic viscosity.

From Fig. 2.9 it becomes evident that during two-component impact, secondary droplets may emerge that contain both drop as well as film liquid. Quantitative data on the composition of secondary droplets experimentally difficult to access and therefore experimental data on this parameter is rare. In the scope of this dissertation a new method to obtain such data is developed and validated, which

is presented in Chapter 6. As a part of the next section, which addresses the methods for characterising and analysing drop impact, the existing approaches for determining the composition of secondary droplets will also be discussed.

2.2. Methods for characterisation and analysis of drop impact

Two new techniques are developed in the scope of this work. One to characterise the film thickness of the crown sheet and one to determine the volume fraction of immiscible two-component droplets. In this section, a brief overview of experimental methods commonly used to characterise the main parameters related to drop impact is given to highlight the methodological gaps the newly developed methods address. The technique for volume fraction determination of secondary droplets utilises methods from machine learning, which are subsequently introduced. Finally, a short overview of numerical methods is given.

2.2.1. Experimental methods

The main quantities and characteristics that are of interest in the context of drop impact onto wetted substrates are: film thickness, crown morphology, the flow in the crown and the characteristics of secondary droplets. If multiple liquids are involved in a two-component impact, additionally the composition of the crown or the secondary droplets becomes relevant. In the following, common experimental methods to characterise those parameters are discussed.

Film thickness characterisation in the context of drop impact

The thickness of the film on the substrate before impact is an important quantity that needs to be precisely determined to achieve repeatable experiments, but also the thickness of the lamella during impact as well as the thickness of the crown sheet are of interest.
A commonly used technology to quantify the thickness of thin films are chromatic confocal sensors (CCS). These sensors utilise chromatic aberration to measure distance or thickness (Browne et al., 1992; Miks et al., 2010). During a measurement white light is sent through a system of lenses, which are aligned, so that chromatic aberration shifts the focal point in the measuring range depending on the light wavelength. Interfaces that are in the measuring range reflect light which is captured and then analysed by a spectrometer. The intensity of the wavelength that has its focal point directly at the interface is maximal. By analysing the peaks in the spectrum of the reflected signal, the position of the interface can be determined accordingly. In the case of a liquid film, two interfaces, i.e. two peaks, can be detected. Based on the relative position of the peaks in the reflected

light spectrum, the film thickness can be determined. Various studies apply this technique to measure the thickness of the wall-film pre-impact (Cossali et al., 2004; Okawa et al., 2008; Geppert et al., 2016; Lamanna et al., 2020), or to obtain time resolved data of the lamella thickness, during impact (van Hinsberg et al., 2010; Kuhlman and Hillen N. l., 2016).
Although CCS are well suited to determine the film thickness in the lamella without contact, there are restrictions of minimal and maximal thickness that can be measured. The minimal film thickness a sensor can measure is usually 5% to 10% of its overall measuring range. Furthermore, the design of the probes limits the measurement positions so that the thickness of moving traits of the crown, such as the crown sheet, is difficult to measure with this method.
Another approach to estimate a liquid sheet thickness is utilising the Taylor-Culick relation. Both Taylor (1959) and Culick (1960) found that the rim of a rupturing liquid sheet of constant thickness h_c propagates with a steady velocity u_{tc} relative to the liquid sheet. This can be attributed to a balance of inertia and surface tension. The liquid of the sheet is initially at rest, subsequently when it is absorbed by the rim it is accelerated to u_{tc} . This contributes inertial forces that are decelerating the rim, at the same time surface tension at the connection between film and rim opposes this deceleration. The resulting relation between film thickness and relative rim propagation velocity is $u_{\mathrm{tc}} = \sqrt{\frac{2\sigma}{h_c \rho}}$.

Thoroddsen et al. (2006) used this approach to estimate the thickness of the ejecta emitted in the early stages of drop impact. Both Aljedaani et al. (2018) and Thoroddsen et al. (2011) applied the Taylor-Culick relation to propagating Marangoni holes in the crown sheet and estimated a crown thickness of $29 \pm 9\,\mu\mathrm{m}$ and $23\,\mu m$ respectively. In this study CCS technology is used to measure the thickness of the wall-film before as well as the thickness of the lamella during drop impact. In Chapter 5 the Taylor-Culick relation is used to estimate the evolution of the thickness of the crown sheet.

Characterisation of crown morphology

The impact of a drop onto a liquid film can result in various forms and shapes. Capturing this morphology is an essential step in understanding the underlying physical processes. Imaging techniques are widely used to capture the morphology of drop impact. Worthington (1908) succeeded in inspiring the scientific world with his fascinating snapshots of drop impact, using a quarter plate camera and short-time electric flashes. Significant advances in imaging techniques have been made in recent decades. The development of high-speed cameras with CMOS or CCD sensors enable researchers to capture drop impact with frame rates in the order of 10^4 fps, providing a boost to drop impact research (Liang and Mudawar, 2016). An often used technique to capture time resolved videos of drop impact is shadowgraphy, where a high-speed camera is used in combination with direct backlighting of high intensity. Different types of high-speed imaging applied in the

context of drop impact experiments are discussed in Thoroddsen et al. (2008). A more recent review of Versluis (2013) discusses imaging techniques in the context of general fluid mechanics.

The obtained time resolved videos are used to categorise the regime of drop impact. In doing so, various regimes can be identified, which are discussed in detail in Sec. 2.1.2 (Cossali et al., 1997; Okawa et al., 2006; Motzkus et al., 2011). Furthermore, image processing techniques are applied to the video material to extract characteristic quantities such as the maximum crown radius and the lifetime of a crown (Roisman et al., 2008). Moreover, time resolved quantities such as the evolution of the crown radius or the crown height (Cossali et al., 2004; Lamanna et al., 2020) or the crown angle (Cossali et al., 2004; Terzis et al., 2019) are obtained from the analysis of high-speed recordings. Additionally, the high temporal and spatial resolution of the recording allows for the identification of local phenomena such as bubble entrainment (Liang et al., 2014b; Thoraval et al., 2012) or the formation of an ejecta (Thoroddsen et al., 2011).

Characterisation of secondary droplets

The impact of a drop may result in the ejection of secondary drops. Various studies focus on the characterisation of the velocity, number and size of these droplets. Different methods are used to quantify the characteristics of these drops which are mentioned in the following. With the phase Doppler (PD) technique (Albrecht et al., 2003), it is possible to determine velocity components and the size of secondary droplets. The technique allows for local measurements in a small volume of $\mathcal{O}(10^{-4})$ m. Hence, the PD technique is often used for characterising secondary droplets resulting from spray impact (Sivakumar and Tropea, 2002; Roisman et al., 2006), thermal atomization (Breitenbach et al., 2018a), secondary droplets resulting from experiments where a drop chain impacts onto a solid substrate or shear driven flow (Mundo et al., 1995; Samenfink et al., 1999).
Larger secondary droplets can be captured from high-speed recordings utilising image processing techniques from one perspective as in Cossali et al. (2004) and Okawa et al. (2006) or multiple perspectives as it was performed by Terzis et al. (2019). A sophisticated method to track three-dimensional trajectories, size and velocity of secondary droplets is high-speed digital in-line holography (Guildenbecher et al., 2014; Guildenbecher et al., 2016) or stereoscopic shadowgraphy (Wu et al., 2020). More recently, similar information can be obtained using the depth from defocus (DFD) technique (Zhou et al., 2020; Zhou et al., 2021; Sharma et al., 2023).

Characterisation of drop and crown composition

When the drop and film consist of different liquids, one measurement quantity of interest is the volume fraction of one liquid in the other. Chromatic high-speed imaging is applied to trace the drop and wall-film liquids. In the process, either the

wall film or the drop is dyed and chromatic high-speed recordings reveal qualitative streak lines of the liquid (Ersoy and Eslamian, 2019; Kittel, 2019). Another approach is to utilise laser-induced fluorescence (LIF), where luminescent dye is used as a marker. In a basic application of the LIF technique, luminescent dye is used as a tracer to qualitatively determine whether secondary droplets contain drop, film or both liquids (Lu et al., 2020). A similar approach is used in Maliha et al. (2022) where luminescent dye is used to determine the origin of the secondary spray resulting from the impact of a gasoline spray onto a thin oil film. It could be demonstrated that the secondary spray contains oil from the wall-film as well as gasoline from the primary spray. Stiti et al. (2021) developed a two-color LIF method to characterise droplets in an icing wind tunnel. The method is capable to determine whether the drop is supercooled, fully or partially frozen.

In order to derive integral quantities, such as the volume fraction of a two-component drop, from the emitted wavelength intensity signal, it would be necessary to uniformly excite every dye molecule in the drop. Furthermore, the total volume of the drop would have to be determined, and internal absorption would have to be accounted for, as with other quantitative applications of LIF (Greszik et al., 2011). In case the droplet consists of immiscible liquids, it may be necessary to consider additional optical effects at the interface between the respective liquids. Although, there are analytical solutions to the light scattering of an eccentric inclusion in a sphere (Gouesbet and Gréhan, 2000; Videen et al., 1995; Borghese et al., 1992; Fuller, 1995; Wang et al., 2011), these analyses have yet to lead to instruments capable of quantifying the inclusion volume. Given that there is no method to quantify the volume fraction of different liquids in an airborne droplet, a method based on chromatic high-speed recordings from two perpendicular perspectives to estimate the volume fraction is developed in the scope of this work (Chapter 6). Since the framework of the method utilises algorithms of machine learning, a brief introduction will be given in the following section.

2.2.2. Machine learning based data analysis [1]

In recent years, the field of machine learning has gained massive popularity and also found its way into the field of fluid mechanics. Due to the rapid progress in computational power and more sophisticated measurement techniques, an increasing amount of data is available. With the growing amount of data, it has become attractive to use machine learning to gain additional information. Up-to-date machine learning algorithms are applied to various fields of fluid mechanics, for example, in experimental data processing or turbulence closure modelling (Brunton et al., 2020). In general, machine learning algorithms may be classified into three categories based on the data that is available for their training; these classes are known as supervised, semi-supervised and unsupervised learning methods. Supervised learning methods require a large amount of labelled data where the

[1] Part of this section is published in Stumpf et al. (2022b), used under CC BY 4.0.

label contains the desired output. In this way, the quality of the predictions can be permanently checked during training. The training process can be formulated as a minimization problem of the error of the method. In contrast, there are unsupervised learning methods where no labelled data providing ground truth is needed. The algorithm extracts information from the data by recognizing patterns. Furthermore, there are semi-supervised methods that work with a limited proportion of labelled data or corrections received from the environment (Brunton et al., 2020).

In the scope of developing a method of volume fraction determination for secondary droplets, a ray tracing approach is utilised, which enables synthetic data to be generated. This provides the possibility to use machine learning methods from the category of supervised learning. Multiple techniques have been tested and support vector machines (SVM) showed the best performance. A brief discussion of the principles of SVM is given in the following.

Support-vector-machine

The SVM is a supervised learning algorithm which is used for the classification of data. In the training process labeled sets of data are used to find a boundary, also referred to as hyperplane, that best separates the data into different classes. To apply a SVM to a specific problem it first needs to be trained. The aim of the training is to find an algorithm that allocates every datum to a class based on its features. This training process and the resulting algorithm are discussed in the following.

The training data has n features and each data point is labeled to a specific class. The learning process can be interpreted geometrically by assigning each feature to an individual axis and plotting each data point into the feature space. The SVM then finds the optimal n-dimensional hyperplane which separates the classes from each other. In Fig. 2.10 a simplistic example of classification into two classes based on two features is given. The solid line describes the optimal separating hyperplane while the dashed lines describe the margin between the classes. The margin is defined by support vectors which are marked by the dashed circles in the figure. Accordingly, the optimal separating hyperplane is the hyperplane with the maximum margin. In case the data is not perfectly separable, Cortes and Vapnik (1995) introduced the soft margin SVM, which tolerates a certain amount of data inside the region of the margin. A further method to increase the applicability of SVMs is the use of kernel functions (Boser et al., 1992). If the data is not separable by linear hyperplanes, the n-dimensional feature space can be transformed into a higher dimensionality N and be separated by a N-dimensional hyperplane. In this way it is possible to create arbitrary hypersurfaces to separate the patterns of

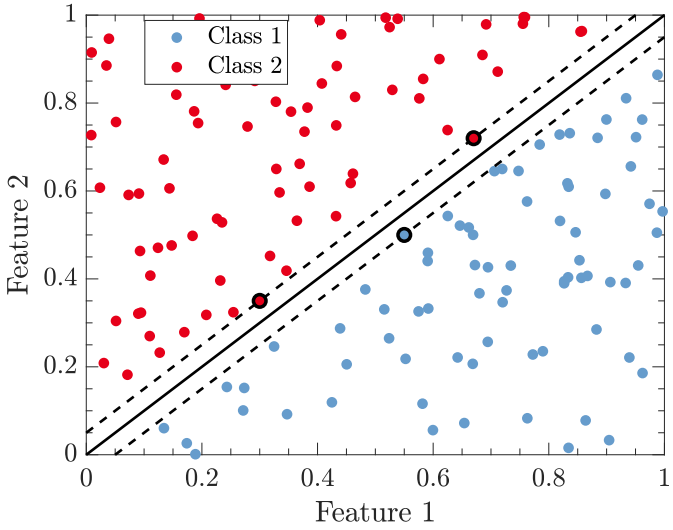

Figure 2.10: Simplified example of the classification principle of an SVM after Richter (2019). The solid line shows the optimal hyperplane, the dashed lines show the optimal margin and the support vectors are marked with black circles.

classes. A detailed description of the optimisation problem can be found in Awad and Khanna (2015), Cortes and Vapnik (1995), Steinwart and Christmann (2008), and Bhavsar and Panchal (2012).

The result of the training process is a classifier $f_j(\vec{b})$, whereby the observation $\vec{b}$ is a vector assigned with values of the observed features. This classifier can then perform a prediction, whether the observation $\vec{b}$ belongs to class 1 or class 2. The geometrical interpretation of the process would be to plot $\vec{b}$ into the feature space and depending on which side of the hyperplane it is on, it is assigned to either class 1 or class 2. SVMs in general are binary classifiers and well suited to discriminate two classes against each other. In order to solve a multi-class problem, as in the present case, more advanced strategies such as the *error correcting output* (ECOC) framework, first introduced by Dietrich and Bakiri (1995), need to be applied. This framework allows for a separation of the multi-class problem into multiple binary classification problems. Basically the ECOC method consists of a encoding step that assigns which classes of which binary classifier are to be compared, and a decoding step where the outputs of all the binary classifiers are evaluated and a predicted class is assigned (Escalera et al., 2010; Allawein et al., 2000)).

Two of the most prominent strategies to encode in ECOC are the *one-versus-all* (OVA) and the *one-versus-one* (OVO) method. If c is the total number of classes, in the OVA method a number of $l = c$ binary classifiers are trained, distinguishing

between one individual class and the set of all other classes. Whereas in the OVO method a number of $l = c(c-1)/2$ classifiers are trained, building classifiers for every possible class pair (Awad and Khanna, 2015; Chaitra and Saravana Kumar, 2018). Note that in the scope of this work only the OVO method is used. Accordingly, each classifier represents a hyperplane separating one specific class from all other classes. Which binary classifier discriminates between which classes is specified in the coding matrix m_{kj}, which has the dimension $c \times l$ and for whose elements the following applies: $m_{kj} \in \{1, 0, -1\} (k \in \{1..c\}, j \in \{1..l\})$. In Table 2.2 an example for a coding matrix for classification into three classes, organised according to the OVO method is given. The value 1 can be translated with “class to compare”, 0 with “class to ignore” and -1 with “class to compare to” (Allawein et al., 2000). The columns define which classes are compared with each other in the respective classifier. In this example the classifier f_1 discriminates between class 1 and class 2 while ignoring class 3, as defined in the first column of the coding matrix.

	$f_1(\vec{b})$	$f_2(\vec{b})$	$f_3(\vec{b})$
class 1	1	1	0
class 2	-1	0	1
class 3	0	-1	-1

Table 2.2: Coding matrix m_{kj} for a three-class problem organised according to the OVO method.

Each binary classifier $f_j(\vec{b})$ has an output $s_j \in \{1, -1\}$, indicating the outcome of the binary decision. According to the coding matrix in Table 2.2 the output of f_1 would be $s_1 = 1$ if the observation $\vec{b}$ is assigned to class 1 and $s_1 = -1$ if $\vec{b}$ is assigned to class 2.

In order to infer a predicted class from the output information s_j of the individual classifiers a decoding step is necessary. The predicted class $\hat{k}$ is chosen by searching for the class k, where the decoding function $d(m_{kj}, f_j(\vec{b}) = s_j)$ is minimal for a given input observation.

$$\hat{k} = \arg\min_{k} d(m_{kj}, s_j) \tag{2.37}$$

In this study a loss-weighted decoding following Escalera et al. (2010) is applied, resulting in the following decoding function:

$$d = \frac{\sum_{j=1}^{l} |m_{kj}| g(m_{kj}, s_j)}{\sum_{j=1}^{l} |m_{kj}|}. \tag{2.38}$$

with $g(m_{kj}, s_j)$ being the loss function for which in this study the ”hamming” principle has been chosen:

$$g(m_{kj}, s_j) = \frac{1 - sign(m_{kj} s_j)}{2}. \tag{2.39}$$

The output of the decoding function is a measure of how often the binary decisions based on an observation turns out in favor of a specific class. In the limiting case, d becomes 0 if every decision is in favor of the class, or $d = 1$ if no decision is in favor of the class. The decoding step can alternatively be expressed as a maximisation problem by using the complement of the decoding function $d' = 1 - |d|$ and the classification applies as

$$\hat{k} = \arg\max_{k} (1 - |d|). \tag{2.40}$$

This complementary approach is used in the presented study.

2.2.3. Numerical methods

One of the objectives pursued by experimental drop impact research is to provide simplified models of the drop impact outcome that can be used in simulations of systems where a spray interacts with a wall. Examples of spray systems could be internal combustion engines or exhaust gas after-treatment systems. A drop impact event inherits very short time and length scales and numerically resolving those in a full-scale spray simulation would require enormous computational resources. Consequently, drop impact models where the impact event is reduced to a set of input and output parameters can efficiently reduce computational costs. However, numerical simulations of single drop impact resolving the respective time and length scales can provide valuable field information on flow quantities. It is possible to numerically investigate process parameters that are experimentally difficult to achieve. The impact of very small and fast drops would be one example. Therefore, the numerical simulation is a good complement to the experimental investigation of drop impact.

The impact of a liquid drop onto a solid substrate or liquid film can be interpreted as a multiphase problem with at least one liquid and one gaseous phase. Therefore, one of the core challenges in numerical drop impact research is to find a correct representation of the interface (Liang and Mudawar, 2016). Some methods do not require a direct reconstruction of the interface, such as Lagrangian particle (LP) methods (Gingold and Monaghan, 1977; Yang et al., 2017) or Lattice Boltzmann (LB) method (Shi et al., 2008; Shen et al., 2012; Raman et al., 2015; Zhang et al., 2014). Common mesh-based methods capable of describing a multiphase problem include the volume of fluid (VOF) method (Hirt and Nichols, 1981), standard-level-set (SLS) (Osher and Sethian, 1988) or phase-field method (PHF) (Harlow and Welch, 1965; Hirt and Nichols, 1981; Wacławczyk, 2017). In the VOF method, a field parameter ranging from 0 to 1 describes the respective volume fraction of fluid A and B in a control volume. The VOF method is used in various studies in the context of drop impact. Examples are Coppola et al. (2011), Rieber and Frohn (1999), and Nikolopoulos et al. (2005). In the framework of the SLS method, a continuous function Φ describes the distance to the interface. A level-set of

$\Phi(\vec{x}, t) = 0$ represents the interface accordingly. Capillary forces can be derived from the curvature of the level-set function. LS method or deviations are applied to drop impact in Shao et al. (2015) and Lee et al. (2011). While VOF performs well in mass conservation, the SLS-Method can represent the interface more accurately (Wacławczyk, 2017). Moreover, there are studies where VOF and SLS are used in a combined approach coupling both methods (CLSVOF) (Son, 2003; Liang et al., 2014b) to benefit from the advantages of both models (Liang and Mudawar, 2016).

While VOF and LS methods represent the interface sharply, diffuse interface PHF methods represent the interface as a region of non-zero thickness where fluid parameters change abruptly but continuously. In these models, a field variable (i.e. order parameter) is introduced to map the change of fluid parameters(Wacławczyk, 2017).

Based on experiments carried out in the scope of this thesis, a new formulation of the PHF method could be validated (Bagheri et al., 2022b). This study shows that capturing the relaxation of a capillary interface towards its equilibrium is essential for accurate simulations of two-phase flows with high dynamics such as the impact of a drop onto a liquid. To validate the numerical model, experiments in the crown formation regime are conducted and characteristic parameters such as the crown radius and the crown height are extracted to compare with the simulations. The fact that the whole impact process stays axisymmetric is utilised to lower the computational costs of the validation process. Figure. 2.11 exemplifies one of the results of the study where experiments and simulations are shown in juxtaposition, highlighting the excellent agreement between experiment and simulation. In a subsequent publication, this method could be generalized to an arbitrary amount of phases Bagheri et al. (2022a).

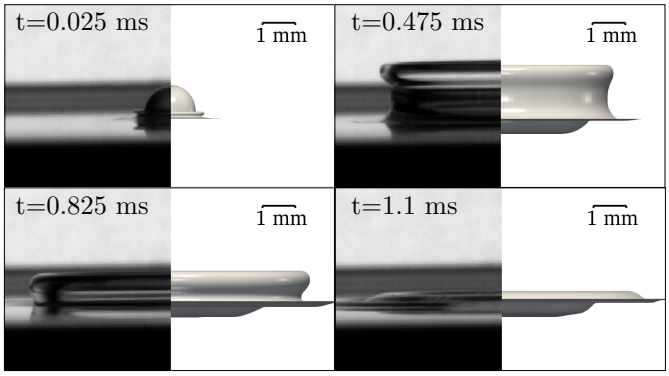

Figure 2.11: Experiments from this project (left) and numerical simulation (right) of a drop impacting onto an oil film at consecutive time instants. The liquid is silicone oil, impact parameters are $U_0 = 2\,\mathrm{m/s}$, $D_0 = 2\,\mathrm{m/s}$, We= 311.9, Re= 600, $\delta = 0.33$. Adapted from Bagheri et al. (2022b).

3. Experimental methods and materials

The experimental facilities and methods that are used and developed in the framework of this dissertation can be divided into two main groups. The first group is presented in Sec. 3.2 and comprises a drop impact setup, which is utilised to characterise the lamella thickness, the crown sheet thickness, the impact outcome and the liquid sheet breakup. The results obtained from this setup are presented in Chapters 4 and 5. The second group, presented in Sec. 6.4, is related to the newly developed method for volume fraction determination of immiscible two-component droplets, which is presented in Chapter 6. Before the experimental methods and setups are discussed, the liquids used are briefly described below.

3.1. Test liquids

In the context of this dissertation, different liquids are used as film or drop liquid. Silicone oils are denoted with the abbreviation SXX, where XX indicates a placeholder for a number representing the kinematic viscosity in mm^2/s. In Table 3.1 the fluid properties of the liquids used are summarized.

Liquid	ν / [mm^2/s]	σ / [mN/m]	ϱ / [kg/m^3]
S5	5	17.72	920
S10	10	18.29	930
S20	20	18.2	945
S50	50	18.6	960
S100	100	18.7	960
FuH2O	0.95	70.2	998

Table 3.1: Material properties of the liquids used in the experiments: kinematic viscosity ν, surface tension σ and density ϱ. The abbreviation "SXX" denotes silicone oils with different respective viscosity.

3.2. Methods for the characterisation of lamella thickness, impact outcome and breakup [1]

3.2.1. Drop impact experiment

A schematic representation of the drop impact setup is shown in Fig. 3.1. The setup can be divided into four main groups: the drop generation system, the wetted substrate, the optical system and the film thickness measurement system. For the

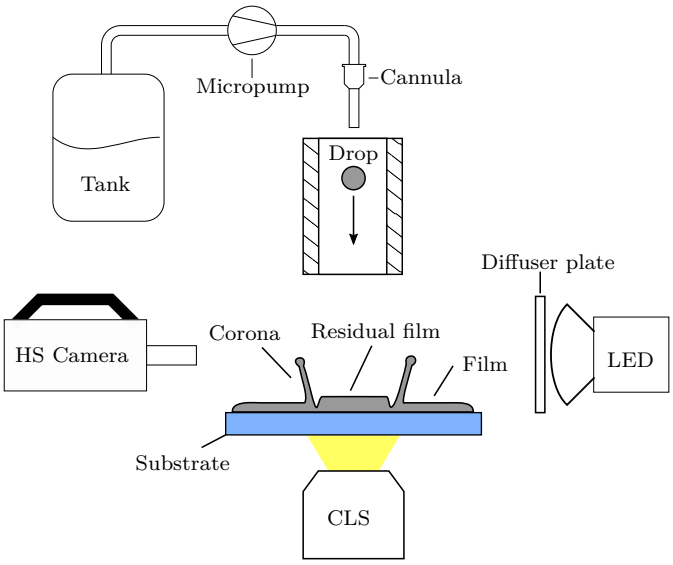

Figure 3.1: Schematic representation of the drop impact setup.

generation of a single drop, a piezo actuated micropump delivers liquid from a tank into a cannula where a drop forms and eventually drops off. The drop adheres to the cannula due to surface tension. If the drop reaches a critical mass that overcomes surface tension, it falls, accelerated by gravity until it impacts onto the wetted substrate. A pipe with an inner diameter of 50 mm is used to minimize external influences on the drop trajectory. The impact substrate is a sapphire plate with a diameter of 50 mm and a height of 0.5 mm, which is optically polished to minimize the effects of surface roughness. The substrate is wetted by a film of a constant thickness in a spin coating process. For drop impact on films with heights larger than 100 µm, a thin ring of PVC foil is attached to the sapphire that confines the liquid film. The film thickness can be constantly monitored with a

[1] Part of this section is published in Stumpf et al. (2022a), used under CC BY 4.0

chromatic confocal line (CL) sensor (Precitec CHRocodile CLS) in combination with a CLS-0.5-LL Probe. This system can measure the film thickness on a line of 4.5 mm length, discretized in 192 individual measurement points. The measurement frequency reaches up to 2000 Hz and the film thickness can be determined with an accuracy of $\pm 0.5\,\mu m$. The CL sensor is used to monitor the film thickness before the impact and measure the thickness of the lamella during the impact. Additionally, the impact process is captured with a high-speed camera system (Photron SA-X2) and a Tokina Makro objective with a focal length of 100 mm. In combination with a diffusor plate, a high intensity LED (Veritas Constellation 120E) is used to provide uniform backlighting. The resolutions achieved range from 19 µm to 30 µm per pixel, depending on the experiment.
The test rig is controlled by an in-house Labview script that serves three purposes: controlling the micropump, collecting metadata consisting of the impact and fluid parameters of the respective experiment and the ambient temperature, and finally providing synchronized trigger signals for the camera using a NI-DAQ system. Note that the synchronization has been implemented in the scope of permanent enhancement of the setup. Hence, the high-speed camera and the CL sensor are not synchronized for every experiment. In the following, the necessary preparations and procedures of the experimental execution are discussed.

Experimental execution

The precise control of the impact parameters is essential for repeatable experiments. To achieve this, each set of experiments is preceded by a number of preparations. In a first step, the projected size of a pixel is determined using a calibration target on which points with known distance are marked. The diameter of the cannula as well as the surface tension and the density of the drop liquid determine the drop size. The diameter of the drop is adjusted by choosing a cannula of the corresponding size while the impact velocity is set by adjusting the height of the cannula over the wetted impact target. Preceding every individual experiment, a cleaning procedure is performed to remove liquid residues from the previous experiment. In order to protect the smooth surface of the substrate, this is done utilising an ultrasonic bath, where the substrate is submerged in isopropyl. After the substrate is dried with pressurized air it is ready for the spin coating process. During this process, film liquid is applied to the center of the substrate, which is then rotated to evenly distribute the liquid. After the spin coating process, the substrate is moved to the impact location, where the film thickness is monitored with the CL sensor from beneath. In Fig. 3.2, an example of the film thickness distribution of a prepared film of 42 µm height 0.1 ms before drop impact is presented. In the figure, h represents the local film thickness distribution as a function of the longitudinal coordinate of the CL sensor. The representative film thickness H_{f0} is calculated as the mean value of h over the length of the sensor line.
The film is considered uniform and suitable for an experiment if the maximum

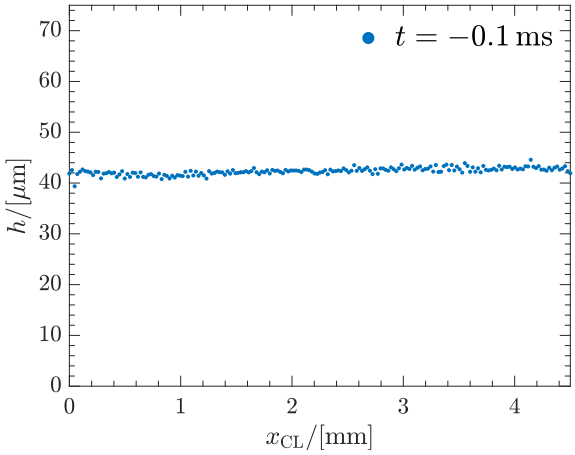

Figure 3.2: Local film thickness h as a function of the longitudinal coordinate of the CL sensor 0.1 ms before drop impact.

difference of h in the measurement interval is less than 5 µm, which is equivalent to an inclination angle of 0.06°. In case the film does not have the intended thickness, the spin coating process and the monitoring are repeated until the desired film thickness is reached. Once the film is prepared, the experiment is initiated by starting the micropump via the Labview script, which generates a drop. Subsequently, a trigger signal is sent to the high-speed camera and the CL sensor, ensuring that both start to capture the impact event simultaneously.
The high-speed recordings of preliminary experiments are analyzed with the help of the Matlab image processing toolbox. As part of the analysis, successive images of the drop are first subjected to background subtraction and then binarized. Once identified, the diameter of the drop can be obtained using the *regionprops* function of Matlab by forming the average of the horizontal and vertical axis. The velocity is determined by tracking the drop centroid over multiple frames shortly before impact. The diameters and impact velocities determined from random samples of all experiments performed are found to have a relative standard deviation of less than 2.5% for the droplet diameter and less than 3% for the velocity.

3.2.2. Needle experiment for film thickness estimation [2]

The thickness of a rupturing liquid sheet can be estimated from the relative rim propagation velocity, surface tension and density by utilising the well-known Taylor-Culick relation presented in Eq. (2.30).

[2]Part of this section is published in Stumpf et al. (2023), used under CC BY 4.0.

In a special configuration of the drop impact setup, a needle is used to pierce the spreading crown during impact and inflict an artificial rupture. For this purpose, the needle is positioned in a fixed position in the vicinity of the impact region so that it pierces the radially expanding crown. A schematic representation of the needle setup can be found in Fig. 3.3.

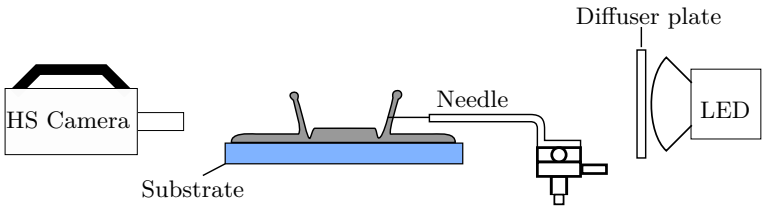

Figure 3.3: Schematic representation of the needle configuration of the drop impact setup.

The propagation of the artificially induced rupture rim is recorded with the high-speed camera system. One result of these experiments is exemplified in Fig. 3.4, illustrating how the needle first punctures the crown sheet, creating a rupture that then propagates along the perimeter of the crown in the subsequent frames. However, the rim does not propagate along a planar liquid sheet but along the conical contour of the crown. To address this, the horizontal displacement observed in high-speed recordings is projected onto a circular path lying on the perimeter of the crown. Provided that the crown is rotationally symmetric, the angle $\Delta\alpha$ through which the rim propagates between two consecutive frames at times t_1 and t_2 is given by

$$\Delta\alpha = \left|\arcsin\left(\frac{x_R(t_1,y)}{r_{\mathrm{cs}}(t_1,y)}\right) - \arcsin\left(\frac{x_R(t_2,y)}{r_{\mathrm{cs}}(t_2,y)}\right)\right|, \tag{3.1}$$

where x_R is the horizontal distance measured from the crown centre axis to the rupture rim and r_{cs} is the radial distance from the centre axis to the crown sheet (as shown in Figure 3.5). Both quantities are functions of time and height above the crown base, y. Using the Matlab image processing tool, these two quantities can be obtained directly from the high-speed images, as indicated in Fig. 3.6, where the outline of the rim and the crown border in subsequent time steps is plotted as coloured lines.

To compute the velocity of the rim in the azimuthal direction, u_{az} (compare Fig. 3.5) , the time average of the crown radius over two subsequent frames is formed, i.e.,

$$\Delta s_{\mathrm{az}} = \bar{r}_{\mathrm{cs},12}\Delta\alpha; \quad \bar{r}_{\mathrm{cs},12} = \frac{r_{\mathrm{cs},1} + r_{\mathrm{cs},2}}{2}; \quad u_{\mathrm{az}} = \frac{\Delta s_{\mathrm{az}}}{\Delta t} \tag{3.2}$$

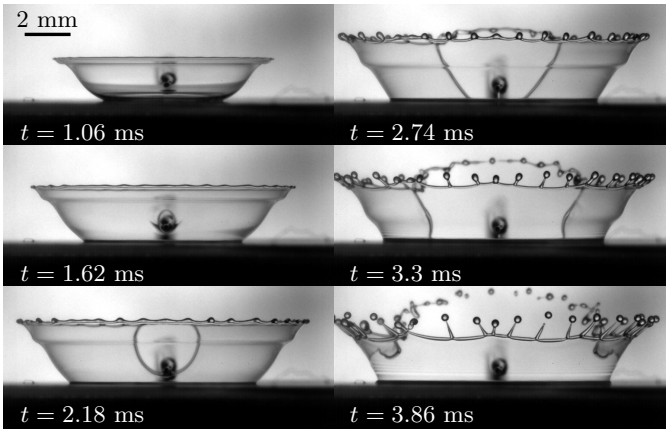

Figure 3.4: Puncturing of the crown sheet using a needle and propagation of the resulting hole throughout the sheet. The Δt between the images is 0.56 ms. Drop impact parameters are: film and drop liquid are S10 (liquids designation is explained in Table 3.1), $U_0 = 3.2\,\mathrm{m/s}$, $D_0 = 2\,\mathrm{mm}$, $H_{\mathrm{f0}} = 77\,\mu\mathrm{m}$, We = 1041, Re= 640, $\tilde{\delta} = 0.0385$.

where $r_{\mathrm{cs},1}$ and $r_{\mathrm{cs},2}$ are the crown radii at the times t_1 and t_2 and $\Delta t = t_2 - t_1$.

The velocity u_{tc} appearing in Eq. (2.30) is the velocity normal to the rim, which would require following material points in the sequence of images available from the high-speed camera. Since this is not possible, the velocity u_{tc} was estimated by using the measured horizontal velocity of the rim, u_{az}, and the local inclination angle of the rim to the vertical, θ, in the form $u_{\mathrm{tc}} = u_{\mathrm{az}} \cos\theta$. This approach also assumes that the advection of the crown wall liquid is zero, which for the horizontal velocity component of the rim is thought to be a good assumption.

Due to the high frame rate, the displacement of the rim in one time step is relatively small as can be seen on the close spacing of the coloured lines in Fig. 3.6. This makes the measurements susceptible to pixel-locking effects. To address those effects, a running median filter with a width of five subsequent time steps is used on the u_{az} data. Assuming small angles α, the error of the u_{az} measurements can be estimated as

$$u_{az,e} \approx \sqrt{(\frac{1}{t_e}\Delta l_e)^2 + (-\frac{x_e}{t_e^2}\Delta t_e)^2}. \tag{3.3}$$

The time interval over five time steps at a frame rate of 50 kHz is $t_e = 0.1\,\mathrm{ms}$. The spatial error can be specified by the pixel resolution $\Delta l_e = 19\,\mu\mathrm{m}$, whereas the temporal accuracy can be specified by the shutter speed of $\Delta t_e = 18.37\,\mu\mathrm{s}$. A typical rim velocity would be $u_{\mathrm{typ}} = 3\,\mathrm{m/s}$ (as will be shown in Chapter 5), which results in a typical displacement of $x_e = u_{\mathrm{typ}}/t_e$. The estimated error would be

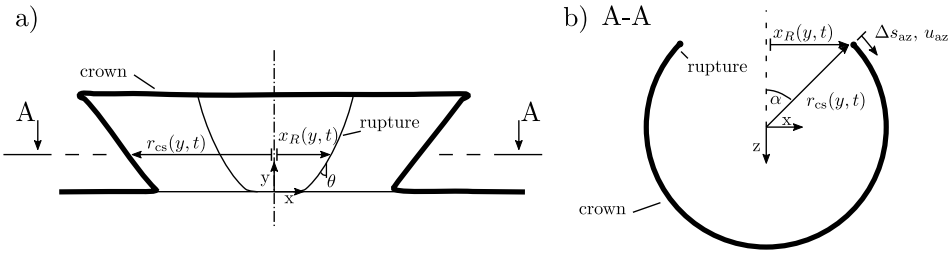

Figure 3.5: Sketch of a crown with an artificially inflicted rupture. a) shows a side view and b) a top view, showing the time and location dependent crown radius r_{cs}, projected x position x_R, the propagation angle of the crown α, the azimuthal displacement Δs_{az} and velocity u_{az} as well as the local rim angle θ.

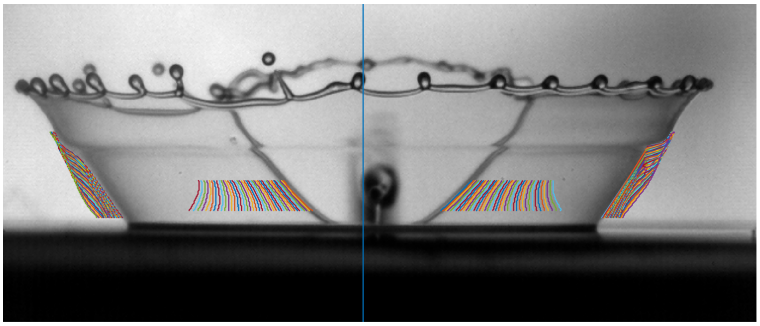

Figure 3.6: Drop impact at $t = 2.6$ ms. Blue line denotes crown centerline/axis. The rim contour at different subsequent time instants is shown with different colours on the left and right side of the centerline. The liquid is S10 and the impact parameters are: $D_0 = 2\,\text{mm}$, $U_0 = 3.2\,\text{m/s}$, $H_{f0} = 80\,\mu\text{m}$, We $= 1041$, Re $= 640$, $\tilde{\delta} = 0.04$.

$u_{az,e} \approx 0.2$ m/s. At this point, it should be noted that Eq. (2.30) neglects inertial effects related to an acceleration of the rim. This may lead to a overestimation of the sheet thickness.

3.3. Experimental methods for the characterisation of the volume fraction of two-component droplets [3]

The precise allocation of the proportions of two liquids contained in a two-component drop poses a challenge, as only the captured images of the droplets are available. With a dye mixed into one of the liquids it is possible to distinguish between the two immiscible liquids. However, quantification of the volume fraction of two-component droplets is challenging, because the orientation of the droplet with respect to the illumination and/or imaging optics is not known *a prior* and also changes with time. For instance, Fig. 3.7 shows a red coloured water droplet encapsulated in silicone oil suspended in an acoustic levitator at consecutive time steps. While at $t = 0.232$ s the projected part of the inner droplet only covers a small portion of the total projected area, at $t = 0.6$ s it occupies almost the entire area. The size of the projected image of the encapsulated droplet varies depending on its position in the outer droplet relative to the observer.

To describe such two-component drops, different sizes and ratios are introduced

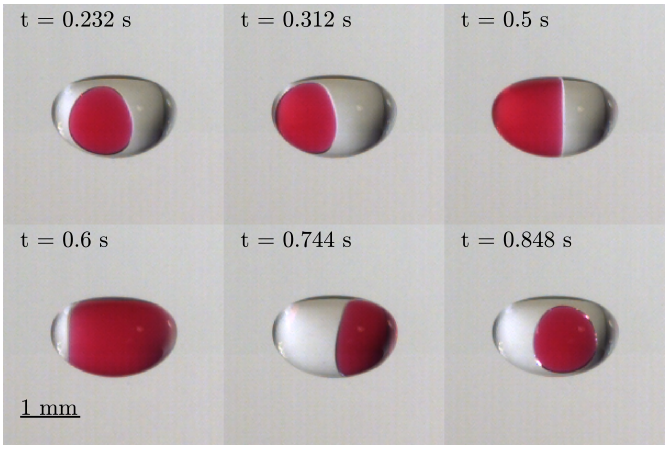

Figure 3.7: Levitated two-component droplet ($V_{\text{frac}} = 0.13$) of red coloured water (FuH2O) and silicone oil (S20) for various time instances.

in the following. The ratio of projected areas from the inner to outer droplet can be expressed as

$$A_{\text{ratio}} = \frac{A_{\text{inner}}}{A_{\text{total}}}. \tag{3.4}$$

The relative position of the inner droplet has a strong influence on the shape and size of the projected area of the inner droplet on the image. In order to describe the position explicitly, a coordinate system located in the center of the two-component

[3] Part of this section is published in Stumpf et al. (2022b), used under CC BY 4.0.

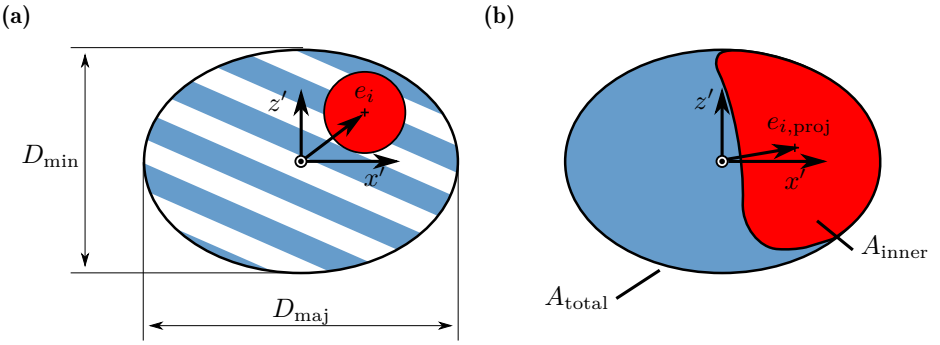

Figure 3.8: a) definition of coordinate system origin. b) definition of projected eccentricity vector.

droplet is introduced in Fig. 3.8a. The position of the inner droplet is denoted by the eccentricity e_i describing the normalized vector between the center of mass of the inner droplet and that of the outer droplet:

$$e_x = \frac{x}{D_{\mathrm{maj}}/2}, \quad e_y = \frac{y}{D_{\mathrm{maj}}/2}, \quad e_z = \frac{z}{D_{\mathrm{min}}/2}. \tag{3.5}$$

where (x, y, z) describes the position relative to the center of the inner droplet and D_{min} and D_{maj} are the directional associated half-axes of the ellipsoidal shaped droplet. The eccentricity vector e_i is not directly observable from the experiments since the projected images of the inner droplet are distorted due to refraction. In order to be able to estimate the position of the inner droplet, the normalised projected eccentricity $e_{i,\mathrm{proj}}$ is introduced, describing the vector between the centers of the two projected areas, outer to inner droplet (see Fig. 3.8b).

Since the shape of the projected image is also influenced by the local curvature of the outer droplet and thus by the deformation of the entire droplet, the ellipsoidal deformation ε is introduced

$$\varepsilon = \frac{D_{\mathrm{min}}}{D_{\mathrm{maj}}}. \tag{3.6}$$

The volume fraction V_{frac} is defined by

$$V_{\mathrm{frac}} = \frac{V_{\mathrm{inner}}}{V_{\mathrm{total}}}, \tag{3.7}$$

where V_{inner} describes the volume of the inner drop and V_{total} describes the total volume of the two-component drop including the inner drop.

In the scope of this dissertation a technique to determine the V_{frac} of two-component drops that utilises a SVM is developed. The SVM is aimed to predict the volume fraction based on features that can be experimentally determined

from high-speed recordings from two perpendicular perspectives. As a part of the development of this technique an elementary ray tracing approach is utilised to create large amounts of synthetic data that are then used to train the SVM and validate its predictions. Furthermore, two sets of experiments are conducted. In the first set chromatic images of single two-component droplets suspended in a acoustic levitator are recorded. The volume fraction of these droplets is known and the obtained experimental data is used to validate the predicitons of the trained SVM. In a second set, the developed method is applied to secondary droplets resulting from a crown splash. For this, a novel setup to observe a crown splash from two perpendicular perspectives is developed. In the following, the ray tracing method, the levitator experiment as well as the crown splash experiment and the corresponding methods will be discussed. The resulting technique for volume fraction determination, its validation and the experimental results will be discussed in Chapter 6.

3.3.1. Inverse ray tracing

To quantitatively determine the size of the projected area of the inner droplet an elementary ray tracing approach was employed, as illustrated in Fig. 3.9a. Assuming the inner droplet is sufficiently illuminated, light emanating from the inner (coloured) droplet will reach the observer (positioned at $y = -\infty$) after being refracted once at the outer droplet/gas interface. By examining all rays coming from the observation direction that intersect the droplet, Snell's law is applied at the gas/droplet interface to determine whether the ray will emanate from the inner droplet or not. This procedure is termed 'inverse ray tracing' in the following. For this the refractive index of the gas, n_g and that of the liquid droplet n_l must be known. Thus, the black rays in Fig. 3.9a will not image the inner, coloured droplet and the projected image, here in the X-Z plane, will appear as shown in Fig. 3.9b. This approach neglects rays with two or more internal reflections before reaching the observer, but in a similar study, such secondary effects were shown to be negligible (Frackowiak and Tropea, 2010), making a more complex ray tracing routine unnecessary.

In Fig. 3.10 a result of this ray tracing procedure is exemplified. The left side of the figure shows a three-dimensional presentation of a spherical inner drop enclosed by an outer drop, while the right side shows the projected image an observer looking at this two-component drop from $y = -\infty$ would perceive. From these projected images quantities such as the A_{ratio}, the eccentricity ϵ and the projected eccentricity vector $e_{i,\text{proj}}$ can be extracted. Accordingly, this procedure allows for generation of large amounts of labeled synthetic data with known V_{frac}. This synthetic data is then used to train the SVM, which is described in detail in Chapter 6.

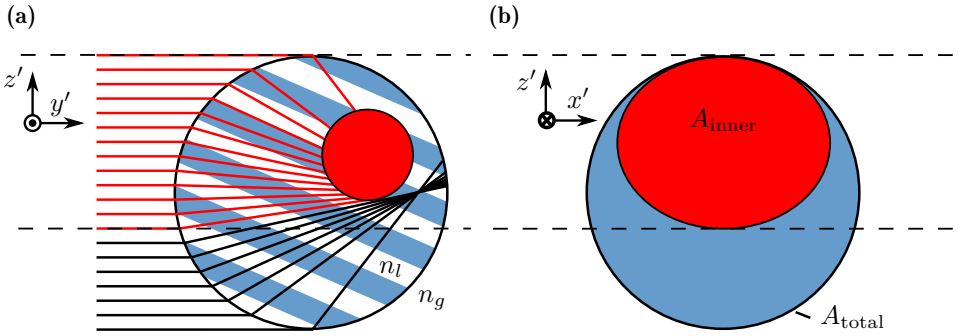

Figure 3.9: a) Schematic representation of ray paths refracted in a two-component droplet in a sectional view. b) projected image from a viewer's perspective.

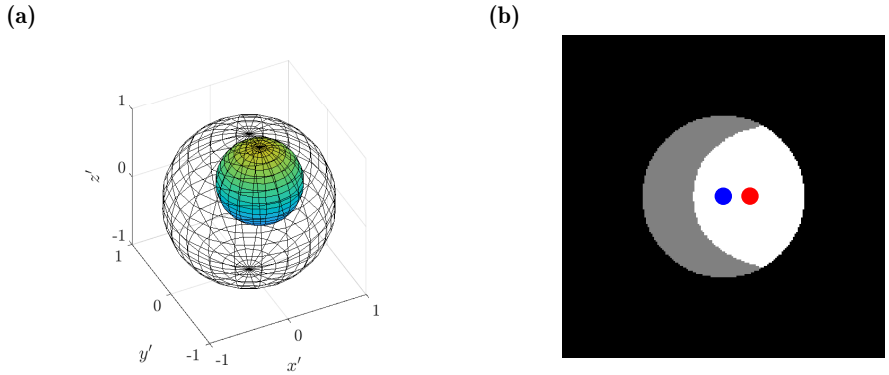

Figure 3.10: a) Three-dimensional plot of a two-component drop b) Calculated projected view observed from the negative y direction. The blue and red dot mark the centers of the total drop and projected area of the inner drop, respectively.

3.3.2. Levitating drop experiment

For experimental validation of the predictions of the trained SVM and the inverse ray tracing method, chromatic recordings of two-component droplets suspended in an acoustic levitator are obtained and evaluated. Figure 3.11 shows the experimental set-up, comprising an acoustic levitator and an image acquisition system using two orthogonally aligned chromatic cameras (Photron SA-X2 with a Tokina Macro 100 ATX Pro lens and 14 mm spacer, GoPro Hero7 with Nikkon AF Micro 60 mm lens).

The setup yields a spatial resolution of 0.0186 mm/px and a framerate of 250 fps for the Photron SA-X2 and a spatial resolution of 0.0151 mm/px and framerate of 240 fps for the GoPro Hero7. Illumination is provided by two LED lights (Veritas Constellation 120e). The background consists of opaque white acrylic glass with a layer of aluminum foil on the rear. Part of the light is diffusely reflected by this background, which ensures more uniform illumination of the drop. Linear polarisation filters that are mounted directly before the camera lens and the light source are used to reduce glare points. The acoustic levitator is a commercial instrument (Tec5, Steinbach am Taunus) operated at 58 kHz. The sound pressure level (SPL) is chosen as a minimum to maintain a stable position of the droplet; hence, minimizing the overall drop deformation. Further information regarding the deformation of droplets due to acoustic pressure in the levitator can be found in Yarin et al. (1998).

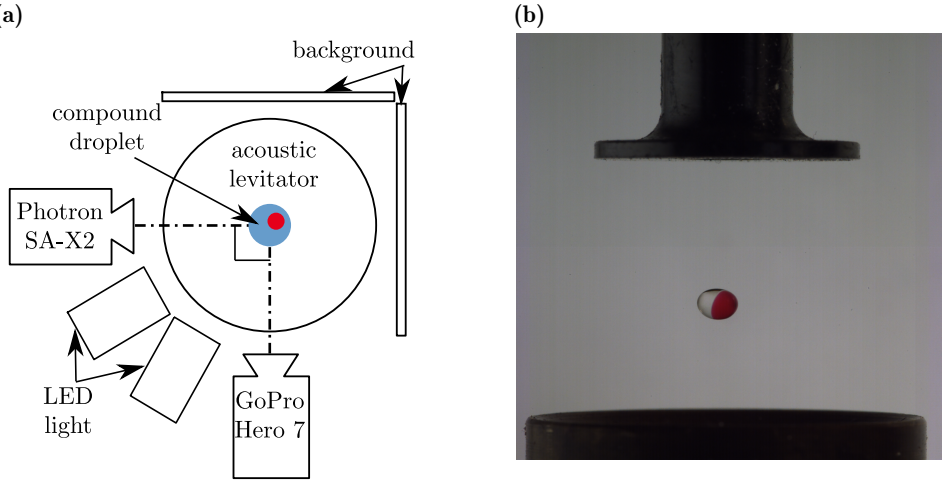

Figure 3.11: a) Schematic representation of the experimental set-up comprising the acoustic levitator from a top view. b) Snapshot of a two-component drop in the acoustic levitator from a side view.

Injection and positioning of the droplet in the acoustic levitator is performed manually with a syringe in two steps. First, the red coloured water droplet is inserted after which the silicone oil is added, forming the two-component droplet. In each step chromatic recordings of the colored water drop and the two-component drop are made, the individual volume is determined by extracting the horizontal and vertical diameter, which are then used to calculate the volume of a rotationally symmetric ellipsoid. Knowing the volume of the individual liquids injected, the volume fraction can be calculated.

For this experiment a silicone oil with a kinematic viscosity of $20\times10^{-6}\,\mathrm{m^2s^{-1}}$ was used, labelled here as S20. The inner water drop was coloured using fuchsine. The surface tension of the dyed drop was measured to be 70 ± 2 mN/m using a DCAT 25 tensiometer (Dataphysics), indicating that the dye had no significant influence on the surface tension of the liquid.

The camera images are then processed using an edge detection routine to determine the total A_{total} area of the droplet. The inner projected area A_{inner} is determined from the red channel of the RGB image. The projected eccentricities $e_{\mathrm{i,proj}}$ and the length of the drops half axis D_{min} and D_{maj} are determined by applying the *regionprops* function of Matlab.

3.3.3. Crown splash experiment

In a further experiment, a crown splash resulting from a red-coloured water drop impacting onto a thin film of silicone oil is observed from two perspectives.

As shown in Fig. 3.12a, the camera sensor is divided in half by employing a centrally placed knife-edge mirror, observing the splash through two equally spaced side mirrors. This optical configuration enables observation with two orthogonal perspectives using a single chromatic high-speed camera. The symmetrical layout ensures that the light rays have the same path length in both perspectives, which allows for a symmetric arrangement of the depth of field (DOF) and the focal plane (FP), as indicated in Fig. 3.12a. Three issues when imaging from two perspectives must be considered: limited depth of field (DOF), the limited spatial resolution and obscuration of the droplet of interest from other surrounding liquid in the experiment. These issues are largely avoided by restricting the observed portion of the splash to only a quarter of the spatial regime of splashing in a zoomed in perspective.

A sketch of the side view of the experimental setup is presented in Figure 3.12b. The impinging drop is produced with a cannula and a micropump. It is accelerated by gravity before impacting onto the liquid film. The liquid is contained in a pool enclosed within surrounding PVC foil, which is affixed to a sapphire glass plate. The liquid film thickness is determined by a confocal chromatic film thickness sensor confocalDT 2421 in combination with a IFS2405-1 probe from Micro Epsilon. The film thickness measurement is performed before the experiment, afterwards the the pool is moved to the impact location. The impact point of the drop is chosen such that it is visible near the outer edges of both observation fields of view (FOVs). This results in good visibility of the splash as well as enabling the velocity and volume of the impinging drop to be determined.

The setup uses the Photron SA-X2 with the same objective, spacer and background configuration as in the levitator experiment. The framerate is 12500 fps at an f-stop of 11 and the DOF was 11 mm. The resolution was 0.037 mm/px.

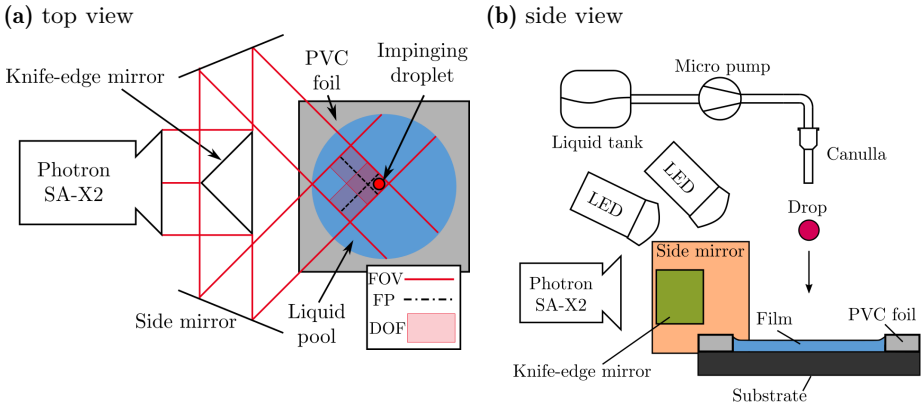

Figure 3.12: a) Sketch of the splashing setup showing the respective fields of view (FOV), focal planes (FP) and depth of field. b) Schematic representation of the experimental setup in a side view.

Image processing

The secondary droplets created during the splash must be recognized in images from both observation directions. Assigning the droplets of each perspective to oneanother poses several challenges. Due to the limited FOV not all drops are visible in both perspectives. Furthermore, droplets can only be observed in focus within the limited depth of field. The DOF is therefore used to detect relevant droplets, which are visible on both images. The mirror system is adjusted so that the focal plane of one perspective of observation is positioned with respect to the outer edge of the FOV of the other perspective of observation. Its distance to the outer edge is half of the experimentally predetermined DOF length. This results in a rectangular area in which a droplet is imaged sharply on both images, as indicated in Fig. 3.12a. To give an example of this principle in Fig. 3.13, an enlarged section of the arrangement of DOF, FOV and FP is presented. The red dot marks the impact position of the primary drop while the coloured dots mark characteristic positions of secondary droplets. The droplet represented by the purple dot will be sharply visible in both perspectives since it is located in both DOF areas. The green droplet would be visible only in perspective 1 (P1) but will be distinctly blurred since it is not in the DOF area. The secondary drop marked by the yellow dot would be seen sharply in perspective 2 (P2), but is out of focus for P1. However, since the origin of the trajectory of the yellow droplet is in the impact area marked by the red dot, the drop must also have passed through the

zone where the two DOF fields intersect; hence, it becomes gradually more blurry in P1. This focal information can additionally be utilised to reduce ambiguity in the matching process.

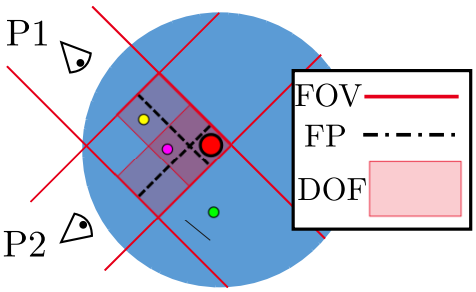

Figure 3.13: Schematic representation of the arrangement of FOV, DOF and FP in the impact area in a top view. P1 denotes the left perspective while P2 denotes the right perspective. The red dot represents the impacting drop while the coloured dots mark potential secondary droplets in characteristic positions.

The droplets are identified by a gradient-based, circle-finding algorithm which neglects drops that are too far out of focus. A fundamental particle tracking velocimetry (PTV) algorithm based on the nearest neighbour principle is then used to determine the droplet trajectories in consecutive images. For an unambiguous determination of droplet trajectories based on two perspectives, a post-processing procedure is employed. If a drop is the same in both perspectives, the horizontal coordinate is independent, but the vertical distance above the substrate must be identical. Therefore, the height of the droplet above the impact plane as a function of time is considered. If this involves two or more droplets having the same height over their entire trajectory, further criteria need to be applied to achieve an unambiguous allocation. Those criteria comprise the drop diameter, the presence of red liquid in the drop and focal information. Once the trajectories of the secondary droplets are identified and matched, several pairs of images of the droplet from both perspectives are extracted and evaluated to obtain the input parameters for the trained SVM. This procedure is analogous to the procedure evaluating the drops in the levitator experiment described in Sec. 3.3.2. Only droplets with a diameter of 10 pixels or more are considered to ensure comparability in the matching process and further evaluation. The assignment process is understandably less prone to error with lower volume number densities of secondary droplets. In Fig. 3.14, single frames of the experiment in two situations are shown. One is shortly before and one 25 ms after the impact. The trajectories of the droplets are highlighted with coloured lines, while matched pairs have the same colour and are marked with a number.

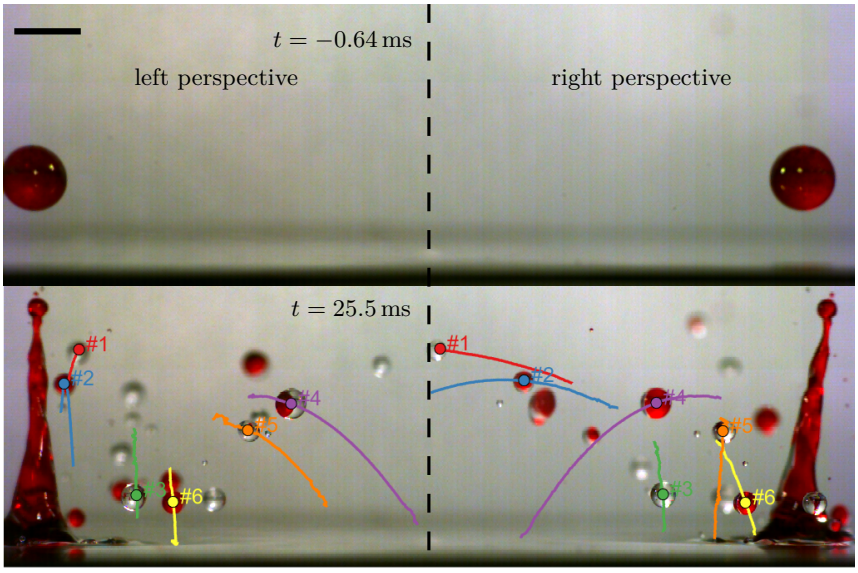

Figure 3.14: Single frames of a drop impact experiment 0.64 ms before impact and 25.5 ms after impact. The trajectories of secondary droplets are highlighted by coloured lines whereby matched pairs have the same colour and are marked with a number. The drop is red coloured water (FuH20, $U_0 = 3.2\,\mathrm{m/s}$, $D = 3\,\mathrm{mm}$, We = 437, Re = 10105) and the film is silicone oil (S10, $H_{\mathrm{f0}} = 600\,\mu\mathrm{m}$, $\tilde{\delta} = 0.2$).

4. Drop impact onto a substrate wetted by another liquid: Flow in the wall film [1]

The impact of a drop onto a liquid film is relevant for many natural phenomena and industrial applications such as spray painting, inkjet printing, agricultural sprays, or spray cooling. In particular, the height of liquid remaining on the substrate after impact is of special interest for painting and coating but also for applications involving heat transfer from the wall. While much progress has been made in explaining the hydrodynamics of drop impact onto a liquid film of the same liquid, the physics of drop impact onto a wall film with different material properties is still not well understood. In this chapter, drop impact onto a very thin liquid film of another liquid is investigated. The thickness of the film remaining on a substrate after drop impact is measured using a chromatic confocal line sensor. The experimental setup is described in Sec. 3.2. The results of the experiments are discussed in Sec. 4.1. Subsequently, a theoretical model for the flow in the drop and wall film is developed in Sec. 4.2 which accounts for the development of viscous boundary layers in both liquids. Finally, the predictions of the model are compared with the experiments and numerical simulations revealing good agreement.

4.1. Residual film thickness

In Fig. 4.1 the impact of a silicone oil (S10) drop onto a silicone oil film (S10), captured by the high-speed video system, is shown in three consecutive instants before, during, and after the impact. The time is given in dimensionless form $\tilde{t} = tU_0/D_0$. It can be observed that the drop impact results in the formation of a crown ($\tilde{t} = 1.92$), which subsequently fragments into secondary droplets ($\tilde{t} = 9.96$).

The evolution of the lamella thickness during the impact is characterised using the CL sensor. The yellow line in Fig. 4.1 indicates the position of the measuring line of the CL sensor whereby x_{CL} represents the longitudinal coordinate. The film thickness h above the substrate as a function of the longitudinal coordinate x_{CL} is shown in Fig. 4.2 for different times. The instants shown in this graph correspond to the high-speed recordings presented in Fig. 4.1.

[1] Part of this chapter is published in Stumpf et al. (2022b), used under CC BY 4.0.

The blue curve in Fig. 4.2 shows the undisturbed film of uniform thickness $H_{f0} = 42\,\mu m$ prior to the drop impact. At $\tilde{t} = 1.92$ a crown has formed as a result of the drop impact. The base of the crown can be recognized at the discontinuity of the orange graph at $x_{CL} \approx 3\,mm$. For larger times $\tilde{t} = 9.96$, the lamella height reaches an asymptotic value and forms a disk of nearly uniform height with a rim at its edge. Even for very large times $\tilde{t} = 51.6$ the thickness of the film remaining on the substrate does not change and thus is referred to as residual film thickness h_{res}, analogous to the residual film that forms on impact with dry substrates. Note that, for $\tilde{t} \to \infty$, the residual film would gradually merge with the wall film. This, however, happens on a larger timescale than the formation of the residual film, which is in the order of multiple minutes for the investigated range of film thickness. For thicker films ($\tilde{\delta} > 0.5$) surface tension and gravity lead to a receding of the crown crater; hence, the phase in which the lamella remains the residual thickness is shorter.

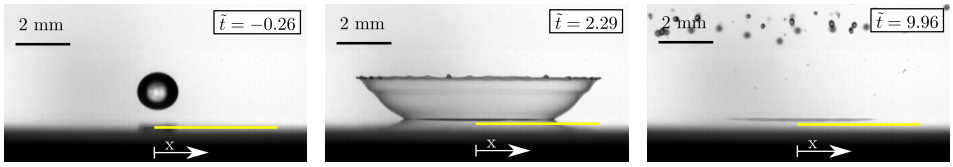

Figure 4.1: Consecutive images from the experiment of a S10 drop impacting onto an S10 film. The yellow line indicates the location of the film thickness measurements shown in Fig. 4.2 whereby x_{CL} represents the longitudinal coordinate of the CL sensor; impact parameters: $U_0 = 3.95\,m/s$, $D_0 = 1.55\,mm$, We = 1230, Re =612, $H_{f0} = 42\,\mu m$, $\tilde{\delta} = 0.027$.

The measurement results for the evolution in time of the film thickness at the impact axis $x_{CL} = x_0$ are shown in Fig. 4.3. The impact axis is not exactly at the position $x_{CL} = 0$ of the CL sensor for every impact. The approximate impact axis x_0 is determined by using the local maximum of the drop lamella at early times. For the example, shown in Fig. 4.2, this would result in $x_0 = 0.2\,mm$, taking the film thickness distribution at $\tilde{t} = 2.29$ as a reference. The measured values $h = 0\,\mu m$ at the impact instant $t = 0\,ms$, correspond to the stage when the total film thickness, including the drop height, exceeds the maximum limit of the working range of the instrument. The evolution of the film thickness in time is only very slightly influenced by the initial film thickness, as shown in Fig. 4.3a. However, Fig. 4.3b and Fig. 4.3c reveal that the dependence of the drop viscosity and even the wall film viscosity is significant.

In all the cases, shown in Figs. 4.3 the evolution of the film thickness initially follows the inertial regime expressed in Eq. (2.10). At later times, 2 - 3 ms after impact, when the thickness $h(t)$ is comparable with the thickness of the viscous boundary layer, viscous effects become dominant. As a result, a constant residual

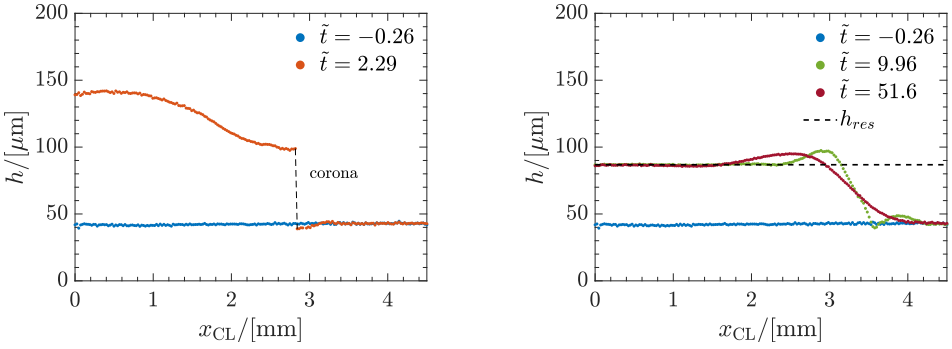

Figure 4.2: S10 drop impacting onto a S10 film. Film thickness h measured with the CL sensor at different dimensionless times before (blue markers) and after the impact. Impact parameters: U_0=3.95 m/s, D_0=1.55 mm, H_{f0} =42 µm.

thickness is measured. The thickness of the residual film after drop impact onto a dry substrate is determined in Eq. (2.14) and after drop impact onto a substrate wetted by the same liquid of the initial thickness comparable with the drop diameter, is expressed in Eq. (2.15). A detailed analysis and the predictive model are described in the next section.

In Fig. 4.4 the relation of the residual film height to the initial film thickness $\tilde{\delta}$ is shown. The residual film height is normalised by D_0 and scaled with $\mathrm{Re}^{-2/5}$. With this scaling, the ordinate represents the factor A defined in Eq. (2.14). The impact parameters of the experiments are listed in Table 4.1. In cases 1 to 7 the drop and film liquid, do not differ in the individual experiments. The viscosity, drop diameter and impact velocity are varied. It becomes apparent that none of these parameters influences the scaling, thus all values collapse on a horizontal line at $A \approx 0.72$. It is worth to mention that this value is close to the theoretical predictions of $A = 0.79$ for drop impact onto dry substrates (Roisman, 2009a). Furthermore, it can be seen, that the initial film thickness $\tilde{\delta}$ has almost no effect on the scaling, neither for the one-component impact of cases 1 to 7, nor for the two-component impact presented in cases 8 and 9. Only when the liquid of the film and drop differ, as in cases 8 and 9, where the viscosity ratio of film to drop viscosity is $\kappa_* = 2$ and $\kappa_* = 0.5$ does the scaling change. This is a rather surprising result, noting that the residual film thickness itself seems to be independent of the initial film height and the initial film height is much smaller than the drop diameter. How can the viscosity of the wall film have such a high influence on the dynamics of the lamella flow while at the same time its thickness is much smaller than that of the droplet?

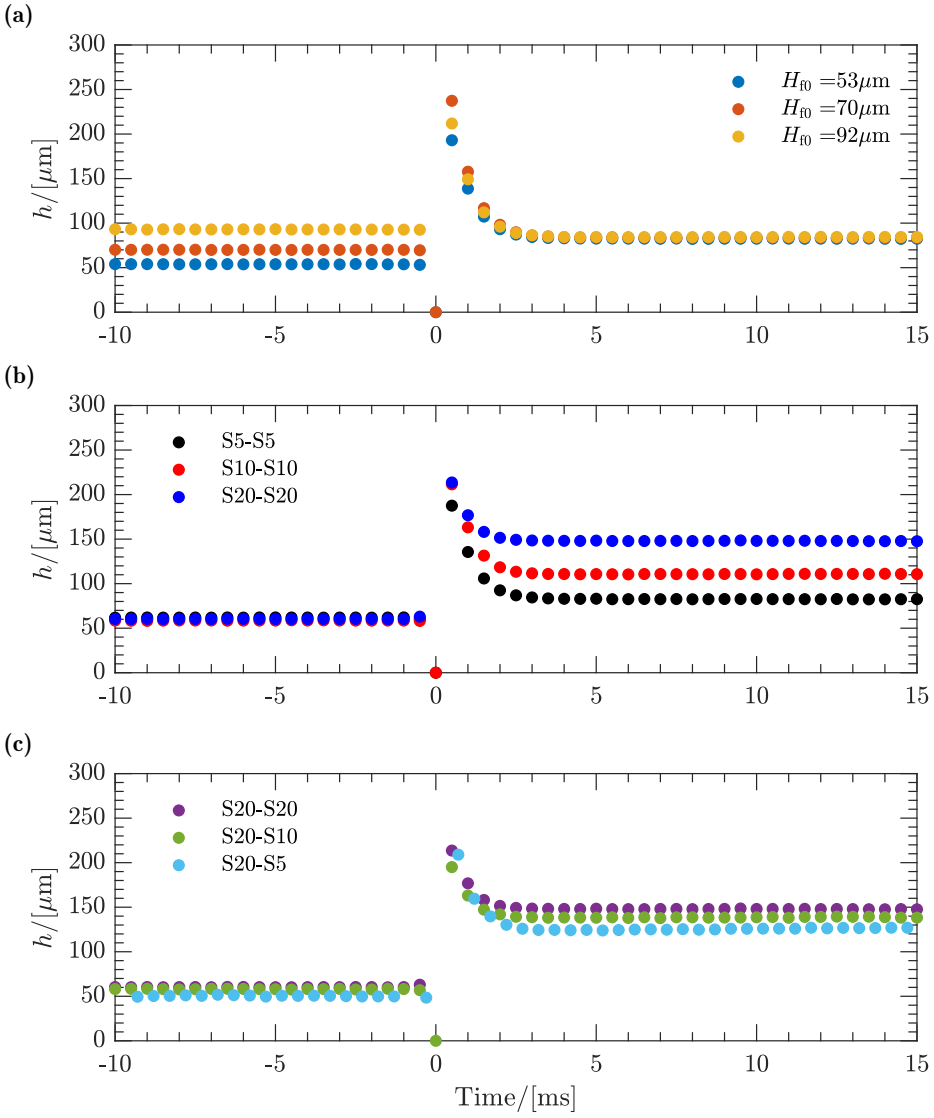

Figure 4.3: Evolution of the film thickness at the impact axis $x_{CL} = x_0$ for a) various initial wall film thicknesses H_{f0} for the same combination of the liquids, S5-S5, b) various drop viscosities and c) various liquid wall film viscosities.

case	film	drop	D_0/[mm]	U_0/[m/s]	Re	We
1	S5	S5	2	3.2	1280	1063
2	S10	S10	2	3.2	640	1041
3	S20	S20	2	3.2	320	1063
4	S10	S10	2	4.23	846	1819
5	S10	S10	1.55	3.96	614	1235
6	S10	S10	3	2.45	735	915
7	S10	S10	3	3.45	1035	1815
8	S10	S5	2	3.2	1280	1063
9	S5	S10	2	3.2	640	1041

Table 4.1: Variations of the initial drop diameter D_0, impact velocity U_0 and drop and film liquids in the experimental campaign. The relative uncertainty of the drop diameter is below below ±2.5% and the relative uncertainty of the impact velocity is smaller than ±3%.

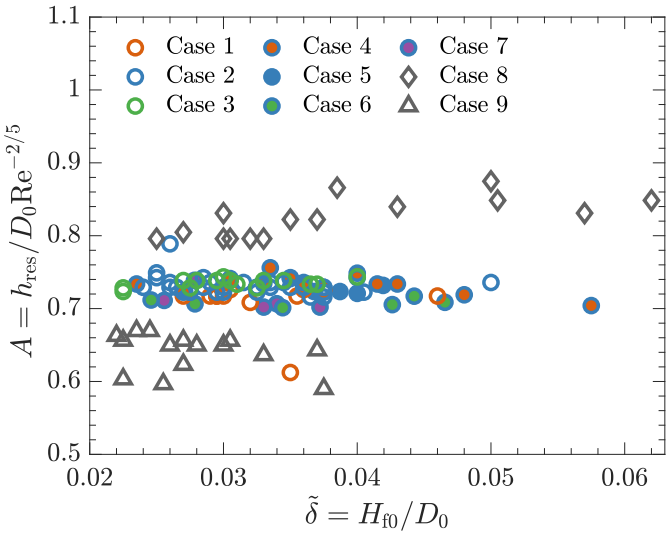

Figure 4.4: Measurement data for the scaling parameter of the residual film thickness A defined in (2.14) for various viscosity ν, impact velocity, U_0 drop diameter, D_0 and initial film height H_{f0}. The cases are defined in Table 4.1.

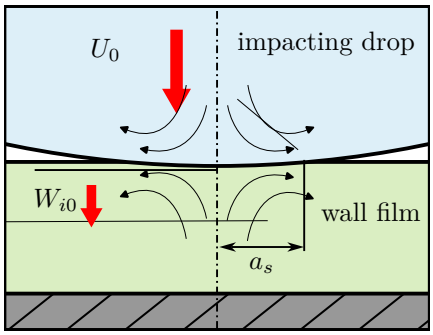

(a) Initial stage of drop penetration

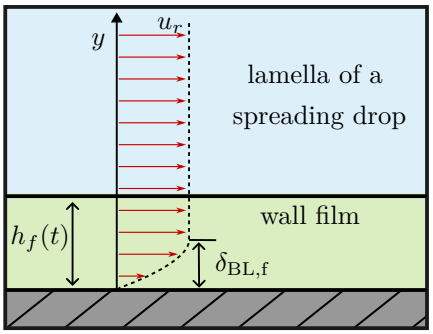

(b) Short times $t < t_{\nu_f}$

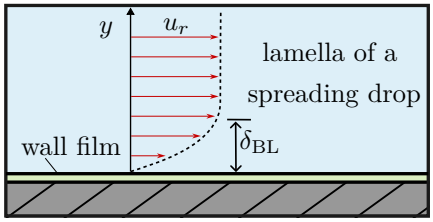

(c) Long times $t \gg t_{\nu_f}$, outer solution for the lamella of the spreading drop

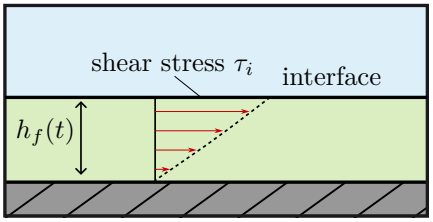

(d) Long times $t \gg t_{\nu_f}$, inner solution for the flow in the wall film

Figure 4.5: Sketches of the main assumed stages of drop impact, its initial penetration and spreading.

4.2. Dynamics of the drop and wall film spreading

Consider an impact of a liquid drop onto a solid substrate wetted by another liquid. If the Reynolds and Weber numbers are much higher than unity the impact is governed by liquid inertia. Although the investigated liquids in the experiments are miscible, the effects of diffusion are neglected since they occur on a much larger time scale. This is justified due to the fact, that the diffusion coefficient, which is in the order of 10^{-9} to $10^{-12}\,\mathrm{m^2/s}$ and is therefore much lower than the kinematic viscosity of $\nu \sim 10^{-6}\,\mathrm{m^2/s}$ (Tosun, 2007; Perez et al., 2011). The interface between the two liquids is thus theoretically treated as if the liquids were immiscible. The initial deformation of an inviscid drop onto a solid substrate is considered in Roisman (2022). The flow is approximated by a flow past a disc of a wetted radius $a_s(t)$, which is defined in Fig. 4.5a. In the case of drop impact onto

a liquid film the interfacial velocity W_{i0} at the film-drop interface, indicated in Fig. 4.5a, has to be considered. The pressure at the interface at the initial stage of impact $\tilde{t} \ll 1$ can be estimated as (Roisman, 2022)

$$p_{id} = \left[\frac{1}{2} + \frac{D_0^{1/2}}{\pi t^{1/2}(U_0 - W_{i0})^{1/2}}\right] \rho_d (U_0 - W_{i0})^2, \quad t \ll \frac{D_0}{U_0}. \tag{4.1}$$

If the contact radius $a_s \approx \sqrt{D_0(U_0 - W_{i0})t}$ is much smaller than the thickness of the wall film, the pressure in the film can be estimated from Roisman (2022), using a similar approach

$$p_{if} = \left[\frac{1}{2} + \frac{D_0^{1/2}}{\pi t^{1/2} W_{i0}^{1/2}}\right] \rho_f W_{i0}^2, \quad t \ll \frac{D_0}{U_0}. \tag{4.2}$$

Equating both these pressure expressions and taking only the dominant term for short times yields

$$W_{i0} = \frac{\rho_d^{2/3}}{\rho_d^{2/3} + \rho_f^{2/3}} U_0. \tag{4.3}$$

Certainly, if the densities of the liquids are very close, Eq. (4.3) is reduced to

$$W_{i0} = \frac{1}{2} U_0, \quad \text{if} \quad \rho_d \approx \rho_f. \tag{4.4}$$

This relation has been identified in the experimental studies on drop impact onto a liquid layer of the same liquid (Fedorchenko and Wang, 2004; Berberović et al., 2009; Bisighini et al., 2010). However, the explanation of this relation is based on the pressure estimation using the stationary Bernoulli equation, which neglects transient effects.

If the initial thickness of the wall film is much smaller than the drop diameter, $\tilde{\delta} \ll 1$ (as in the present experiments), the duration of the initial drop penetration with the velocity W_{i0} is very short, $\tilde{t} \sim \tilde{\delta}^2$, and its influence on the flow in the subsequent stages of impact can be neglected.

At larger times, when the spreading radius is larger than the drop height the flow in the drop and in the lamella can be approximated by an inviscid thin film flow (Yarin and Weiss, 1995), taking into account a growing viscous boundary layer that is restrained first to the wall film on the substrate, as indicated in Fig. 4.5b (Roisman, 2009a).

4.2.1. Early stages of impact: boundary layer in the wall film

If the Reynolds number of the impacting drop is much higher than unity, the spreading of the lamella is dominated by inertia. In the case of a dry wall the evolution of the lamella thickness is expressed in Eq. (2.12) if it is thicker than

the viscous boundary layer. It can be expect that these expressions are valid also for the case of drop impact onto a substrate wetted by the same liquid, if the film thickness is much smaller than the drop initial diameter, as shown schematically in Fig. 4.5b.

The evolution of the thickness of the wall film for long times can be estimated using the same approach as in the case of the drop lamella

$$\tilde{h}_f \approx \tilde{\delta}\frac{\eta}{\tilde{t}^2} + \frac{4}{5}\gamma\tilde{t}^{1/2}\mathrm{Re_f}^{-1/2}, \tag{4.5}$$

$$\mathrm{Re_f} \equiv \frac{D_0 U_0}{\nu_f} = {\kappa_*}^{-1}\mathrm{Re}. \tag{4.6}$$

where κ_* is the ratio of the drop and film viscosity, and Re is the Reynolds number based on the drop viscosity, defined in Eq. (2.1). Equation (4.5) is obtained using the viscosity of the wall film in the solution from Roisman et al. (2009b) and accounting for the initial dimensionless film thickness $\tilde{\delta}$.

Next, the modified solution (Roisman et al., 2009b) can be used for the estimation of the characteristic times and thicknesses. The time at which the wall film thickness is equal to the thickness $1.88\sqrt{t/\mathrm{Re_f}}$ is therefore

$$\tilde{t}_{\nu f} = 0.87\tilde{\delta}^{2/5}\eta^{2/5}\mathrm{Re_f}^{1/5}. \tag{4.7}$$

The corresponding wall film thickness at this instant is

$$\tilde{h}_{\nu f} = 1.8\tilde{\delta}^{1/5}\eta^{1/5}\mathrm{Re_f}^{-2/5}. \tag{4.8}$$

At times $\tilde{t} > \tilde{t}_{\nu f}$ the flow in the wall film is driven mainly by viscous stresses.

4.2.2. Late stages of impact: boundary layer in the lamella

At long times after impact $\tilde{t} \gg \tilde{t}_{\nu f}$ the thickness of the viscous boundary layer is much larger than the thickness of the wall film. The flow has to satisfy the continuity of the velocity and the shear stress at the film/drop interface at the distance $h_f(t)$ from the wall. The similarity solution (Roisman, 2009a) is not valid in this stage. The approximate solution in this stage consists of the outer solution in the drop lamella and the inner solution in the wall film, as shown in the sketch in Figs. 4.5c and 4.5d.

Outer solution in the lamella of the spreading drop

The thickness of the wall film is much smaller than the thickness of the viscous boundary layer in the liquid drop. In the outer solution, shown schematically in Fig. 4.5c, the thickness of the wall film is therefore neglected, the velocity profile and the shear stresses are approximated by the solution for drop impact onto a

solid substrate (Roisman, 2009a). This approximation is justified by the fact that the velocity at the interface is much smaller than the velocity r/t of the inviscid flow outside the boundary layer.

The thickness of the viscous boundary layer in the lamella of the drop can be approximated as $\delta_{\mathrm{BL}} \approx 1.88\sqrt{\nu_d t}$. The radial velocity far from the interface at large times is estimated $u_r \approx r/t$ using Eq. (2.8). The shear stress at the wall in the liquid is estimated in Roisman (2009a) as

$$\tau_{id} \approx r\frac{\sqrt{\nu_d}\rho_d}{t^{3/2}}. \tag{4.9}$$

At large times it can be assumed, that the velocity in a thin liquid wall film is much smaller than the velocity of spreading outside the boundary layer. Therefore, Eq. (4.9) is valid also for the case of drop spreading on a thin wall film at large times $\tilde{t} \gg \tilde{t}_{\nu f}$.

Inner solution for the wall film

The flow in the thin wall film is approximated by a linear profile, as shown in Fig. 4.5d. This flow can be estimated from the condition of the continuity of the shear stress at the interface with the drop flow

$$u_r = \frac{\tau_{id}}{\nu_f \rho_f} y. \tag{4.10}$$

The axial velocity in the wall film interface is then found from the continuity equation using Eq. (4.9) and Eq. (4.10)

$$W = -\frac{1}{r}\int_0^{h_f} \frac{\partial (r u_r)}{\partial r} \mathrm{d}y = -\frac{\sqrt{\nu_d}\rho_d h_f(t)^2}{\nu_f \rho_f t^{3/2}} \tag{4.11}$$

The velocity W determines the rate of change of the wall film thickness. The evolution equation for $h_f(t)$ at long times is therefore

$$h_f'(t) = -\frac{\sqrt{\nu_d}\rho_d h_f(t)^2}{\nu_f \rho_f t^{3/2}}. \tag{4.12}$$

The solution of the ordinary differential equation Eq. (4.12), which satisfies the initial condition $h_f(t_{\nu f}) = h_{\nu f}$ is

$$h_f(t) = \frac{h_{\nu f}}{1 + \frac{2h_{\nu f}(1-\xi)\sqrt{\nu_d}\rho_d}{\nu_f \rho_f \sqrt{t_{\nu,f}}}}, \quad \xi = \sqrt{\frac{t_{\nu f}}{t}}. \tag{4.13}$$

For large times $\xi \to 0$ the wall film thickness approaches the residual value

$$h_{\mathrm{res},f} \approx \frac{h_{\nu f}}{1 + \frac{3.86\sqrt{\nu_d}\rho_d}{\sqrt{\nu_f}\rho_f}}. \tag{4.14}$$

Inner and outer solution for the lamella

Finally, the residual film thickness is estimated as the sum of the residual thicknesses of the wall film and drop lamella

$$h_{\mathrm{res}} = h_{\mathrm{res},f} + h_{\mathrm{res},d} = A\frac{D_0}{\mathrm{Re}^{2/5}}, \tag{4.15}$$

$$A \approx A_0 + \frac{1.49\tilde{\delta}^{1/5}}{1+3.86\kappa_*^{-1/2}\rho_d\rho_f^{-1}}\kappa_*^{2/5} \tag{4.16}$$

where A_0 is a weak function of the film thickness, assumed constant for $\tilde{\delta} \ll 1$. The value $\eta \approx 0.39$ is taken from the results Roisman (2009a) obtained for drop impact onto a dry wall. The estimated value of A_0 for a dry substrate is $A_0 = 0.79$. However, it can be different in the case of drop impact onto a wetted wall since the drop spreading can be influenced by the initial stage of drop collision with the wall film.

In most practical cases, the density ratio of the wall film and drop liquids is relatively close to unity. The expression for the parameter A can be thus reduced to

$$A \approx A_0 + \frac{1.49\kappa_*^{2/5}\tilde{\delta}^{1/5}}{1+3.86\kappa_*^{-1/2}}, \quad \kappa_* = \frac{\nu_f}{\nu_d}, \quad \rho_d \approx \rho_f. \tag{4.17}$$

In Fig. 4.6 the experimental data for the factor A is compared with the theoretical predictions of Eq. (4.17) based on $\tilde{\delta} = 0.02$ and $\tilde{\delta} = 0.06$, the smallest and the largest relative film thicknesses, used in these experiments. The theoretical predictions only weakly depend on the initial film thickness but rather significantly depend on the viscosity ratio κ_*. The value $A_0 = 0.55$ is estimated from the best fit to the experimental data. The theoretical predictions agree rather well for values of $\kappa_* \leq 2$.

Considering the limit case of an infinitely viscous wall film, $\mathrm{Re}^\star$ would approach zero and therefore, the presented Eq. (4.16) is not longer valid, but it can be assumed, that the impact onto an infinitely viscous fluid behaves like the impact on a solid substrate. In this case the residual film thickness would be $\tilde{h}_{\mathrm{res}} = \tilde{\delta} + A\mathrm{Re}^{-2/5}$, where $A = 0.79$, as it is determined in Eq. (2.14) for drop impact on solid surfaces.

Fig. 4.7 shows the lamella profile of most extreme fluid combinations for $\tilde{t} = 10$ when the film thickness near the centre of the impact axis has reached an asymptotic value. It can be observed, that for the yellow line with $\kappa_* = 0.25$ the profile near the impact axis is comparably planar as in the case presented in Fig. 4.2. The cases with higher viscosity ratio $\kappa_* \geq 5$ (Blue and orange line) show a curvature of the residual profile for $0 < x_{CL} < 1.2\,\mathrm{mm}$. This is another indication that in the flow in the lamella at high κ_*, there are further influences

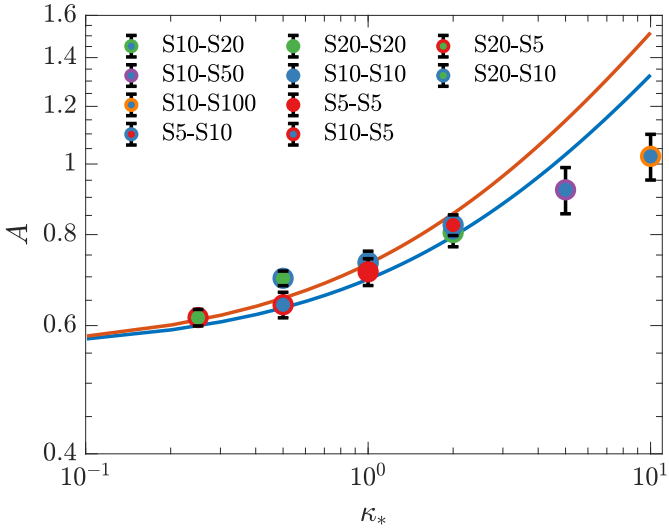

Figure 4.6: Dependence of the parameter A, defined in (4.15), on the viscosity ratio $\kappa_* \equiv \nu_f/\nu_d$. Comparison of the experimental data with the theoretical predictions. The orange line and the blue line represent the upper and the lower range of Eq. (4.17) with $\tilde{\delta} = 0.02$ for the blue line and $\tilde{\delta} = 0.06$ for the orange line. The drop diameter has been varied from 1.5 mm to 3.3 mm while the impact velocity is in the range from 2.45 m/s to 4.23 m/s. The fluid combinations used are expressed by the acronym Sxx-Syy, where Sxx denotes the drop and Syy denotes the film liquid.

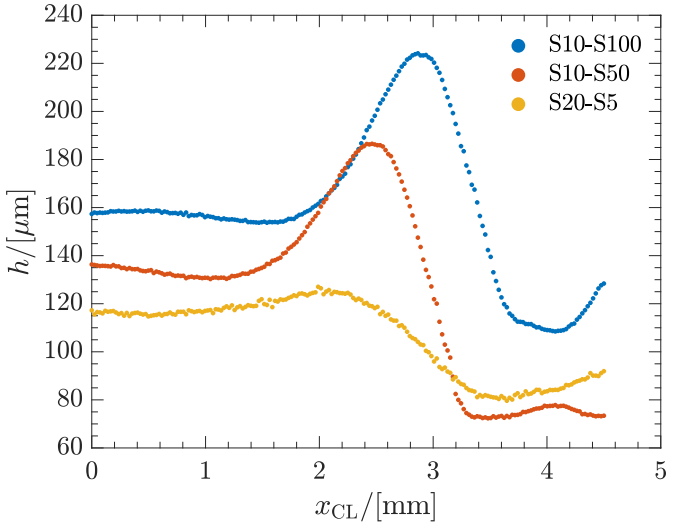

Figure 4.7: Lamella profile for the most extreme fluid combinations after a dimensionless time of $\tilde{t} = 10$. Impact parameters are: Blue: S10-S100, $D_0 = 2\,\mathrm{mm}$, $U_0 = 3.3\,\mathrm{m/s}$, $H_{f0} = 110\,\mu\mathrm{m}$, $\kappa_* = 10$; Orange: S10-S50, $D_0 = 2\,\mathrm{mm}$, $U_0 = 3.3\,\mathrm{m/s}$, $H_{f0} = 73\,\mu\mathrm{m}$, $\kappa_* = 5$; Yellow: S20-S5, $D_0 = 2\,\mathrm{mm}$, $U_0 = 3.3\,\mathrm{m/s}$, $H_{f0} = 60\,\mu\mathrm{m}$, $\kappa_* = 0.25$. The fluid combinations used are expressed by the acronym Sxx-Syy, where Sxx denotes the drop and Syy denotes the film liquid.

that are not yet fully identified. This also manifests in the deviations between theory and experiment. Nevertheless, it is important to note that the approach based on the high Reynolds number allows to predict the order of the residual films even for such relatively small values of the Reynolds numbers $\mathrm{Re}^\star$. This means that the governing physical phenomena are correctly identified in the presented explanation.

The influence of $\tilde{\delta}$ on the A parameter predicted in Eq. (4.17) does not become directly apparent from the results presented in Fig. 4.6, as the minor changes in residual film thickness that would be expected are overlayed by the experiments uncertainty. In order to test the predictive quality of the model, its predictions are compared with existing data resulting from drop impact with the same liquid in film and drop (i.e. $\kappa_* = 1$) onto films at larger film thickness ranging from $0.5 \leq \tilde{\delta} \leq 1.5$, in Fig 4.8.

The theoretical predictions agree rather well with the experimental and numerical data from van Hinsberg et al. (2010) for $\tilde{\delta} \leq 1$ while for $\tilde{\delta} > 1$, significant differences become apparent. These deviations can be attributed to two reasons. First, the

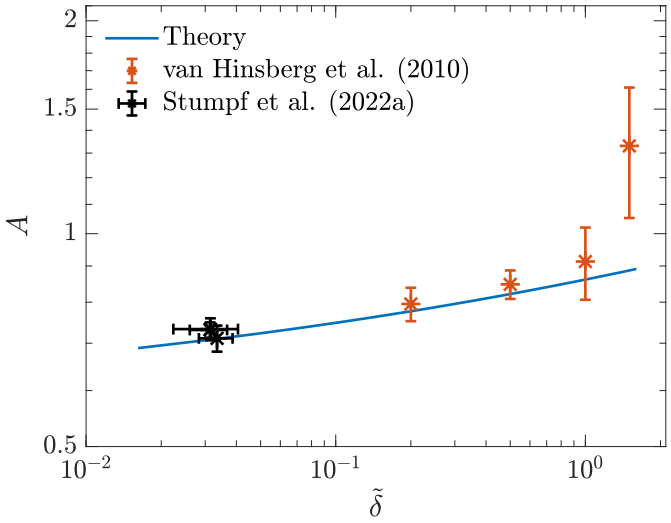

Figure 4.8: Dependence of the initial film thickness on A for $\kappa_* = 1$. Experiments from this study (Cases 1 to 7) are shown in black, results from numerical simulations obtained in van Hinsberg et al. (2010) are shown in orange. Each orange data point summarizes five simulations, where We is varied from 110 to 536, while Re is varied from 539 to 8491. The blue line represents the predictions of Eq. (4.17).

influence of the initial stage of impact is only negligible for $\tilde{\delta} \ll 1$; hence, this stage, which is neglected in the current theory, is gaining importance with increasing film thickness. Second, for drop impact onto films with $\tilde{\delta} > 1$, the curvature of the lamella is not negligibly small anymore as can be seen in the numerical simulations of Berberović et al. (2009) and the experiments of van Hinsberg et al. (2010). This violates a basic assumption that is fundamental to Eq. (4.5) with the consequence that effects of surface tension can no longer be neglected. The influence of surface tension in the thick film regime is evident for comparable parameters such as the spreading diameter of the crown as described in Eq. (2.23) and thus would also have to be considered to describe A for drop impact onto films with $\tilde{\delta} > 1$. However, the fact that predictions agree very well for a dimensionless film thickness up to unity further indicates that the governing physical phenomena have been correctly identified in the model.

4.3. Conclusions

In this study, the thickness of the liquid film remaining on a wetted substrate after drop impact is measured for a broad range of parameters with varying viscosity, drop diameter, impact velocity and initial film height. The experiments show that the scaling in Eq. (2.14) is almost not influenced by the impact velocity, drop diameter, drop viscosity or initial film height for the investigated parameter range.

The dynamics of the flow in the wall film and in the lamella of the spreading drop are considered. The evolution of the viscous boundary layer in the flow is described for short times, when its thickness δ_{BL} is smaller than the wall film thickness h_f, and for long times, $\delta_{\mathrm{BL}} \gg h_f$. For short times, the solution is based on the similarity solution Roisman (2009a), developed for drop impact onto a solid dry substrate. For long times a matching of asymptotic solutions in the outer and inner regions is applied.

The theoretical predictions for the residual film thickness agree very well with the experimental data only in the cases when the Reynolds numbers based on the film thickness, $\mathrm{Re}^{\star}$ are much higher than unity. Furthermore, a comparison of the predictions with numerical data (van Hinsberg et al., 2010) shows very good agreement for $\tilde{\delta} < 1$. This agreement indicates that the main physical phenomena are taken into account in the model. The theory predicts a significant influence of the viscosity ratio on the value of h_{res} and its weak dependence on the initial relative film thickness $\tilde{\delta}$, if $\tilde{\delta} < 1$.

The theoretical predictions for very viscous wall films, associated with small values of $\mathrm{Re}^{\star}$, slightly overestimate the values of the parameter A. This deviation is caused by the very short time for the expansion of the viscous boundary layer in the wall film for which the remote asymptotic solution in Eq. (2.8) is not applicable. Nevertheless, the experiments demonstrate that the dimensionless residual film thickness correlates well with the value of κ_* for a wide range of film viscosity. This result can potentially be used for better modelling of the key phenomena associated with drop impact, like drop and wall liquid mixing, splashing threshold, etc.

5. Corona detachment from the wall film [1]

The almost instantaneous detachment of the crown from the wall film, termed 'corona detachment' is a fascinating phenomena that is described in this chapter. Using the high-speed camera setup described in Sec. 3.2 the drop impact onto very thin films is observed and characterised. In Sec. 5.1 impact parameters that lead to a detachment of the crown sheet are identified and the measurement of the time of detachment are presented. Furthermore, in Sec. 5.2 the results of special experiments with the spreading crown impingement onto a fixed needle are presented giving information on the temporal evolution of the crown sheet thickness prior to detachment. Based on the evidence obtained from the experiments, a self-consistent theory predicting the instant of detachment is developed. As the theoretical analysis is a major contribution of Prof. A. Yarin it is presented in Appendix A. However, in Sec. 5.2 this theory is discussed in the context of the experimental results. Finally, the influence of viscous effects on the detachment are discussed and a conclusion is given in Sec. 4.3.

5.1. Experimental characterisation of the rupture process

Typical outcomes of drop impact onto a liquid film are shown in Fig. 5.1 for four cases in which the drop and wall film are the same fluid but with varying film thickness and/or fluid viscosity. In all cases a crown evolves after impact and in all cases the crown detaches from the wall film, eventually retracting to the upper Taylor rim and disintegrating into ligaments and/or drops. The instant shortly after detachment is marked in this figure with a red box. In this chapter, attention is focused on the mechanisms that lead to this observed corona detachment.

While Fig. 5.1 presents only exemplary observations, experiments have been carried out over a large range of wall film thickness, wall/film fluid combinations and impact parameters. Nine cases, systematically varying the viscosity, fluid combination, drop diameter and impact velocity are defined, and for each case experiments are carried out for a large range of wall film thickness. The fluid

[1] Part of this chapter is published in Stumpf et al. (2023), used under CC BY 4.0.

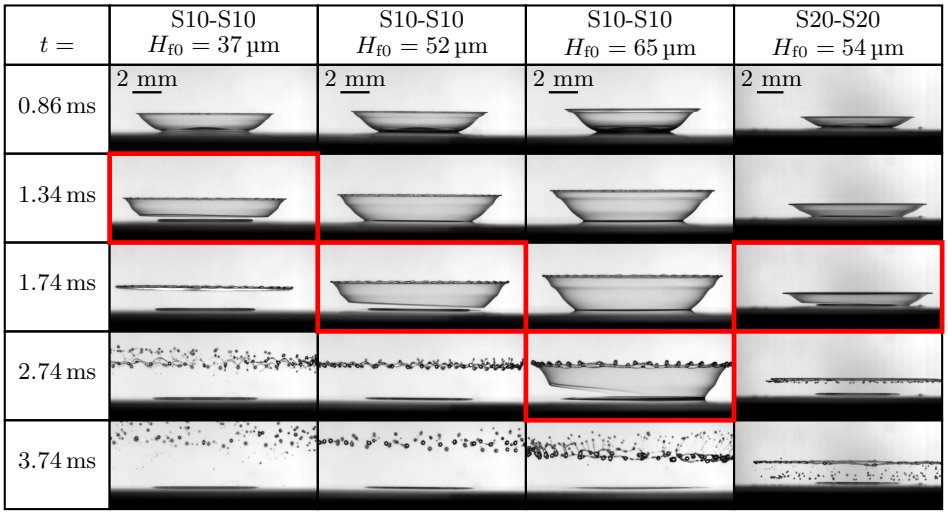

Figure 5.1: Evolution of crown formation, detachment and atomization for cases of varying H_{f0} and viscosity. The instant shortly after detachment is marked in each case with a red box. Impact parameters are: $D_0 = 2\,mm$, $U_0 = 3.2\,m/s$ and $\kappa_* = 1$.

combinations and impact parameters for the individual cases can be found in Table 5.1. These values of film thickness and impact velocity cover the regimes in which corona detachment could be observed. Note that in all cases the drop and film liquids are miscible.

At the high frame rate of the camera, the first instant of detachment can be determined very accurately and furthermore, the critical wall film thickness can be determined, beyond which corona detachment can no longer be observed ($H_{f0,crit}$). The time of detachment is defined as the time interval between first contact of the drop with the liquid film and the instant when a first rupture in the corona is visible. The results of these experiments are summarized in Fig. 5.2 and Table 5.2. In Fig. 5.2 the time of detachment t_d is shown as a function of the initial wall film thickness H_{f0} for different combinations of the drop and film liquid viscosity. These results are not made dimensionless to be compatible with the theoretical results in Eq. (5.5) which are derived in Stumpf et al. (2022b).

It is interesting to note that in the cases with the same liquid in the drop and wall film, the viscosity does not have a significant influence on t_d, since the results for S5-S5, S10-S10 as well as S20-S20 overlap closely. From this figure it is also apparent that for the different fluid combinations, corona detachment can only be observed for some maximum wall film thickness, beyond which no data points are shown. This limiting wall film thickness, $H_{f0,crit}$, is summarized in Table 5.2 for the

marker	ID	film	drop	Re	We	κ_*	U_0/[m/s]	D/[mm]
○	C1	S5	S5	1280	1063	1	3.2	2
□	C2	S10	S10	640	1041	1	3.2	2
○	C3	S20	S20	320	1063	1	3.2	2
□	C4	S10	S10	846	1819	1	4.23	2
□	C5	S10	S10	614	1235	1	3.96	1.55
□	C6	S10	S10	1035	1815	1	3.45	3
□	C7	S10	S10	735	915	1	2.45	3
◇	C8	S5	S10	640	1041	0.5	3.2	2
△	C9	S10	S5	1280	1063	2	3.2	2

Table 5.1: Liquid combinations and impact parameters of the investigated experimental cases. The cases and the symbols from this table correspond to those shown in Fig. 5.2. Sxx denotes the respective liquid. The liquid properties can be found in Table 3.1. The Reynolds and Weber number have been computed using the drop diameter and impact velocity and the liquid properties of the drop.

investigated fluid combinations. While the critical dimensional wall film thickness for corona detachment remains constant for a single component drop impact with the fluids S5 and S10, the critical value of H_{f0} is higher for S20. This can be explained by the fact that in the S5-S5 and S10-S10 cases the corona detachment is superimposed on a crown splash and at the instant when the crown in the S20-S20 case detaches, the crown in the other two cases has already collapsed due to the rim instability and can, therefore, no longer detach. Analogously, it can be observed that for cases with larger drop diameter or velocity (cases 4 to 7), the total collapse of the crown due to crown splash and the associated rim instability will occur at later times and, therefore later times of detachment, i.e. higher critical values of H_{f0} are possible. Finally, the data in Fig. 5.2 reveal a rather strong influence of the viscosity ratio κ_*, exhibiting longer dimensionless detachment times for lower values of κ_* and shorter detachment times for higher values of κ_*.

case	liquid		κ_*	$H_{\mathrm{f0,crit}}/[\mu\mathrm{m}]$
	film	drop		
1	S5	S5	1	75
2	S10	S10	1	75
3	S20	S20	1	80
4	S10	S10	1	83
5	S10	S10	1	62
6	S10	S10	1	135
7	S10	S10	1	95
8	S5	S10	0.5	60
9	S10	S5	2	>120

Table 5.2: Maximum wall film thickness $H_{\mathrm{f0,crit}}$ for which detachment can be observed for different fluid combinations. The impact parameters for the corresponding cases can be found in Table 5.1. Sxx-Syy specifies film-drop fluids; $\kappa_* = \nu_f/\nu_d$

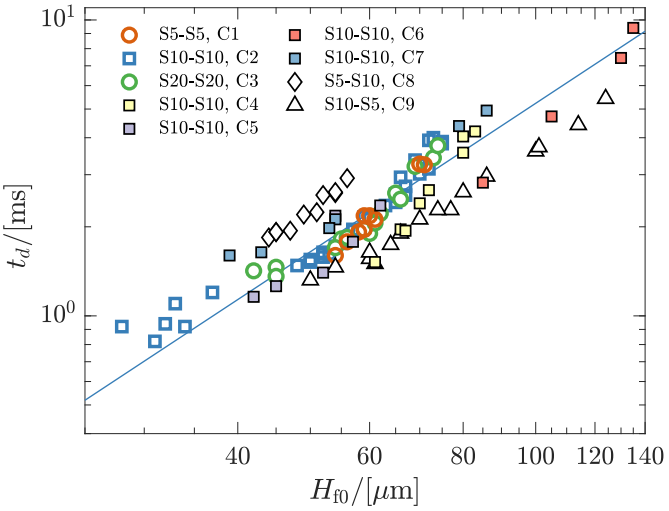

Figure 5.2: Instant of corona detachment t_d at different initial wall film thickness δ, different fluid combinations and impact parameters. The fluid combinations and impact parameters for the individual cases are listed in Table 5.1. The solid line represents the slope predicted by Eq. (5.5) using a value of $k = 73.43$ obtained by a least squares fitting to the data arising from like fluids S5, S10 and S20 and plotted for the S10-S10 case.

5.2. Estimation of crown sheet thickness

In order to obtain estimates of the thickness of the crown sheet prior to impact, a needle was used to artificially inflict a rupture in the crown sheet. The propagation speed of the ruptured rim is measured from the high-speed recordings and according to the Taylor-Clulick relation [$h_c = 2\sigma/(\varrho u_{tc}^2)$] the sheet thickness can be determined from the ruptured rim velocity. A detailed description of this method is given in Sec. 2.2. Applying this procedure to selected cases from Table 5.1 results in quantitative data for velocity and crown sheet thickness as a function of time and height y above the substrate for both the right and left hand sides of the crown. An example of one such measurement is shown in Figs. 5.3 and 5.4 for the velocity and rim thickness, respectively. Comparing results for the right and left hand sides of the hole propagation reveals a high degree of symmetry, confirming that the crown wall is equal in thickness around the circumference at a given height and time. Of particular interest however, is the film thickness very close to the impact surface, i.e., at very low y values, since this is a representative thickness of the rim when the crown begins to detach for cases which are not artificially ruptured. These values will be subsequently used in the theoretical model predicting the detachment time to compare with experimentally determined instants of detachment.

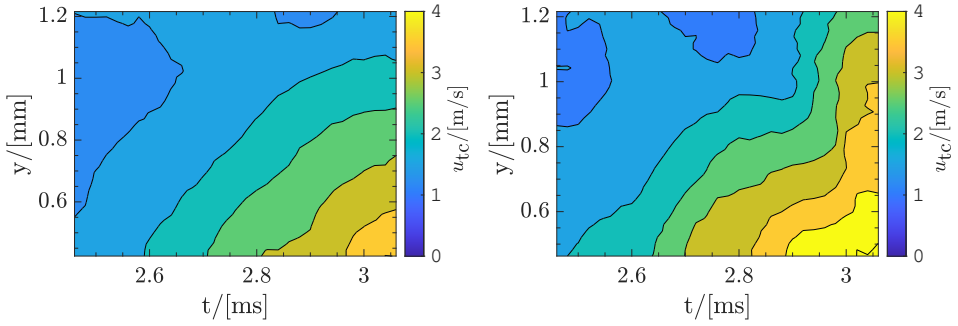

Figure 5.3: Measured rim velocity to the left and right side of the crown centerline. Impact parameters: $D_0 = 2\,\text{mm}$, $U_0 = 3.2\,\text{m/s}$, $H_{f0} = 80\,\mu\text{m}$. The velocities on both sides are shown as positive values for better comparison.

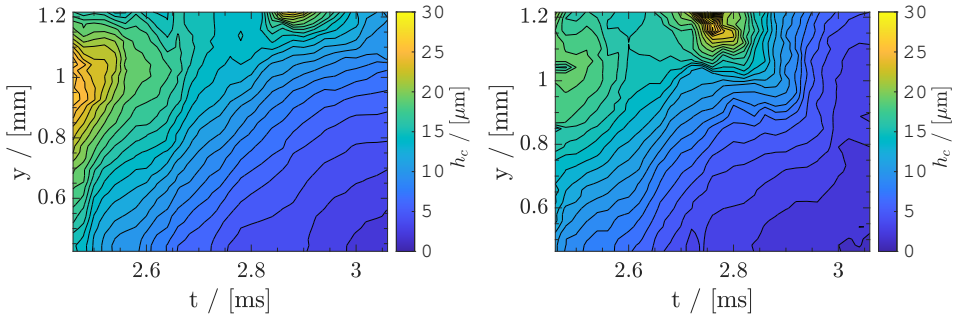

Figure 5.4: Sheet thickness on the left and right side of the crown centerline calculated from Eq. (2.30) using the velocities shown in Fig. 5.3. Impact parameters: $D_0 = 2\,\text{mm}$, $U_0 = 3.2\,\text{m/s}$, $H_{f0} = 80\,\mu\text{m}$.

The crown sheet thickness 0.46 mm above the crown base is then plotted in Fig. 5.5 for three cases of substrate film thickness, $H_{f0} = 61\,\mu\text{m}$, $70\,\mu\text{m}$ and $80\,\mu\text{m}$. The observed trends are clear: the crown sheet reduces rapidly in thickness from about $18\,\mu\text{m}$ to 3-4 µm, or until detachment occurs. For reference, in the case of $H_{f0} = 61\,\mu\text{m}$ the corona detachment occurs at 2.66 ms, for $H_{f0} = 70\,\mu\text{m}$ at 3.5 ms and for $H_{f0} = 80\,\mu\text{m}$ no corona detachment is observed. It is apparent therefore, that the thickness of the crown liquid sheet at the instance of detachment is influenced by the thickness of the liquid film on the substrate. If this thickness

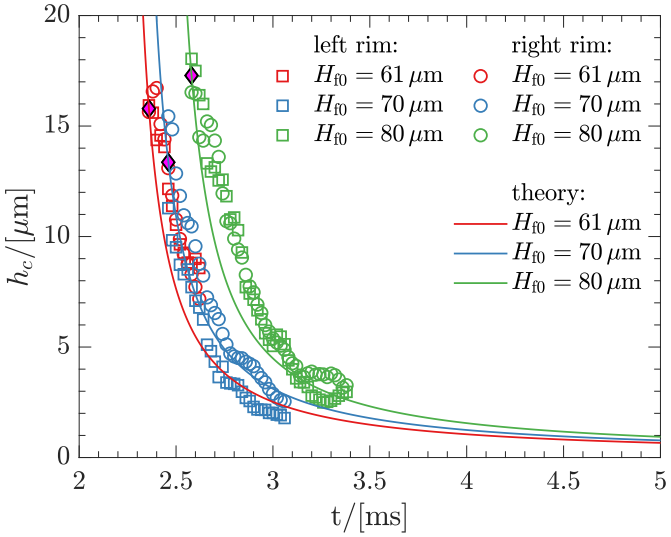

Figure 5.5: Comparison of temporal development of crown sheet thickness from experiments and theory. Experimental data shows the film thickness 0.46 mm above crown base.The fluid for film and drop is S10 for all experiments. H_{f0} is varied from 60 to 80 µm and is colour coded (red: $H_{f0} = 61$ µm; blue $H_{f0} = 70$ µm; green $H_{f0} = 80$ µm). The symbols (□ and ○) denote the left and right rim respectively. The solid lines show the evolution of crown sheet thickness predicted by Eq. (5.3). The temporal offset t_0 is $\{2.31, 2.37, 2.51\}$ ms for $\{61, 70, 80\}$ µm. The magenta coloured diamonds mark the film thicknesses and instances which were used to calculate the offset times t_0. Since the film heights determined from the right- and left-hand sides of the rim coincide well, the mean value of h_c from both sides at the first measured instance of each experiment has been chosen for reference.

is too large, no detachment of the crown occurs. In Fig. 5.5 the predicted film thickness evolution according to Eq. (5.3) is shown for the three substrate film thicknesses, as will be explained below.

5.3. Mechanisms of the film desintegration by hole nucleation and expansion

Analysis of high-speed recordings that capture rupturing liquid sheets has revealed that prior to breakup, often holes appear (Brenn et al., 2005, cf). Around these holes, liquid rims form that propagate, driven by surface tension, until they merge and finally cause a complete breakup. This scenario is treated analytically and discussed in detail in Appendix A, aiming for a theoretical model that predicts the time of detachment. In the following, the main results of this analysis are summarized.

First, considering a hole in a liquid sheet, a critical radius r_* exists for which the energy that is stored in the free surface starts to lower when r_* is exceeded. A specific activation energy must be exceeded for such a hole to emerge spontaneously. This energy is equivalent to the change in surface energy attributed to a hole of the critical radius that appears in an intact film. Assuming that the activation energy for such holes is provided by velocity fluctuations that originate from the early stages of drop impact and are subsequently swept into the crown sheet, the probability of such a 'supercritical hole' to appear can be described as

$$P = \exp\left[-\frac{1.09}{C}\frac{\sigma h_c}{\rho\nu^2}\right]. \tag{5.1}$$

Here, $C = 1.5$ is the universal Kolmogorov spectrum constant (George et al., 1984) and h_c is the thickness of the liquid sheet.

Based on the probability of a 'supercritical hole' and the characteristic timescales involved, an area specific hole formation rate is formulated

$$I_* = 0.067\frac{\nu}{k h_c^4}P, \tag{5.2}$$

where k is the characteristic number of time scales required for hole formation. Considering further that a supercritical hole, once it has emerged, expands with the Taylor-Culick velocity, a threshold based on the percolation theory (Stauffer, 1979) can be formulated, where the liquid sheet can be considered detached when the relative area occupied by holes in the film λ is $\frac{1}{2}$. The time until this threshold is reached is the time of detachment predicted in Eq. (5.5). For this prediction information on the local film thickness in the crown sheet is necessary as it has an influence on the specific hole formation rate as well as the probability of hole formation (cf. Eqs. (5.1) and (5.2)).

The evolution of the crown sheet thickness in the phase shortly before detachment can be described by

$$h_c = H_{\mathrm{f0}}\frac{3D_0}{4BU_0(t-t_0)}, \tag{5.3}$$

where B and $\tilde{t}_0$ are dimensionless constants depending on the characteristics of the lamella flow in the vicinity of the crown base. A detailed derivation of the equation, which is based on the remote asymptotic theory of Yarin and Weiss (1995), is published in Stumpf et al. (2023) and can also be found in Appendix A.3. In Fig. 5.5 Eq. (5.3) is compared with the results of the experiments where the parameters $B = 16$ and $\tilde{t}_0$ are both fitted to the experiments. The predicted $h_c \sim 1/\tilde{t}$ slope of the crown sheet thickness represents the experimental data well. Furthermore, (A.28) yields two boundary values for $h_c(\tilde{t} \to \infty) \approx 1\,\mu\text{m}$ and for $h_c(\tilde{t} \to \tilde{t}_0 = 3/2H_{\text{f0}})$. From the figure, a breakup thickness in the order of

$$h_c \approx h_b = 1\,\mu\text{m} \tag{5.4}$$

can be estimated, for which Eq. (5.1) yields a high probability for breakup (P=0.86). Note that in Opfer et al. (2014), a similar order of magnitude of breakup thickness for aerodynamic bag breakup has been observed.

Since the direct incorporation of Eq. (5.3) in Eq. (5.2) would require a numerical solution of the integral $\int_0^{t-R/u_{\text{tc}}} I_* d\tau$ for the further steps of the model (Eq. A.32), a constant I_* is used as a first approximation. This constant hole formation rate uses the limits $h_c(t \to t_0)$ and $P(h_b)$.

Accordingly, the time of detachment t_d is predicted based on the constant hole formation rate I_*, the percolation threshold $\lambda = 1/2$ and the propagation velocity u_{tc} of supercritical holes and can be formulated as

$$t_{\text{d}} \approx 3.37k^{1/3} \left(\frac{\rho_d H_{\text{f0}}^5}{\sigma_d \nu_d} \right)^{1/3} . \tag{5.5}$$

A more detailed description of the individual steps leading to this equation can be found in Sec. A.4.

Equation (5.5) predicts a scaling $t_d \sim H_{\text{f0}}^{5/3}$, which has been added to the log-log representation of the experimental data in Fig. 5.2. The exact position of this scaling relation on the diagram was chosen using a least squares fit to all data arising from experiments involving like fluids (drop, film), whereby k was used as a fitting parameter. The comparison shown in Fig. 5.2 indicates that this scaling describes the experimental results reasonably well for corona detachments with like fluids. The experimental data suggests that the absolute value of detachment time may be inversely proportional to κ_*, cf. cases 8 and 9 in Table 5.1. Below, at the end of this subsection, the value of k is also estimated theoretically.

For predicted characteristic times in fluid mechanics in general, including the one in Eq. (5.5) [based on Eq. (A.38)] in the present case, the most important aspect is the scaling dependencies on different relevant physical parameters. In this sense, the comparison with the experimental data in Fig. 5.2 shows that Eq. (A.45) predicts the scaling plausibly. As for the question 'how many characteristic times exactly a certain phenomenon takes', i.e., 'what would be the exact value of k in the present case?', the answer always comes from fitting the prediction to the

experimental data (using a least squares approach in Fig. 5.2). This is also done in the present work, and thus, the value of $k = 73.43$ was found for the cases with like fluids S5, S10 and S20 (cf. Fig. 5.2). There is nothing unusual with this value of k. For a general comparison, the Rayleigh theory of capillary breakup of thin inviscid liquid jets predicts that jet breakup takes 39.59 characteristic times $\tau_{\mathrm{ca}} = \sqrt{\rho a_0^3/\sigma}$ [where a_0 is the unperturbed cross-sectional radius of the jet, and $\ln(a_0/\delta_0) = 14$ according to the fitting of the theoretical predictions for the jet length to the experimental data, with δ_0 being the initial perturbation amplitude]; (Yarin et al., 2017)).

Some additional remarks regarding the detachment process are necessary, particularly whether detachment originates and propagates from a single crown wall rupture or whether multiple ruptures are responsible? In most cases, the detachment is observed to propagate from a single visible rupture in the crown wall, although some examples of multiple holes are observed, as is exemplarily illustrated in Fig. 5.6. This ambiguity has two origins. On the one hand, the detachment is very sensitive to the surface film thickness. Since the crown sheet thickness correlates with the initial film thickness and the propagation velocity of supercritical holes is lower in thicker films, the crown sheet ruptures first on the side of the crown exposed to the smaller initial film thickness. To illustrate this sensitivity an example of S10 (film)/S10 (drop) is taken with a film thickness of $H_{\mathrm{f0}} = 52\,\mu\mathrm{m}$ from Fig. 5.1. At the instant of detachment the crown has a radius of approximately 6.3 mm. A variation of 5 µm in film height over the crown diameter would occur already with an inclination of the surface of only 0.03°. According to Eq. (5.5), such a film height variation would lead to a difference in detachment time of 283 µs between opposite sides of the crown. However, the entire detachment process lasts only 120 µs, implying that in this example the film is more levelled than the estimated 0.03°. A second factor is that according to Eq. (A.5), the critical radius of a hole nuclei is 2.18 µm, but the resolution of the camera in the object plane is 19-37 µm. Thus, some nuclei may go unnoticed or merge to a bigger rupture before they can be observed in the recordings.

The velocity fluctuations that may trigger the critical holes can be attributed to turbulent eddies that emerge in the early stages of impact. The relevant velocity for the generation of turbulence in the moments following the impact is the velocity of the drop interface U_{i} rather than the initial drop impact velocity. Under the condition $\sqrt{\nu/(D_0 C_l)} \ll 1$, which holds in all the experimentally explored cases here, the relevant Reynolds number is $\mathrm{Re_i} = (U_0 D_0/\nu)\cot\alpha_d$, where α_d describes the angle of the path of the drop generatrix to the underlying horizontal. At the instant of impact $\cot\alpha_d \to \infty$, and thus $\mathrm{Re_i} \to \infty$, which makes the emergence of turbulent eddies plausible. It should be emphasized that according to Eq. (A.38) the characteristic time of the nucleation of supercritical spontaneously growing holes is of the order $\tau_{\mathrm{nucl}} \sim k\tau_\eta$. Where τ_η is the characteristic time scale of Kolmogorov dissipative eddies, defined in Eq. (A.37). Taking for the estimate $h_c = 1\,\mu\mathrm{m}$ and $\nu \sim 10^{-2}\,\mathrm{cm^2/s}$, one obtains $\tau_\eta \sim 10^{-6}\,\mathrm{s}$, whereas according to

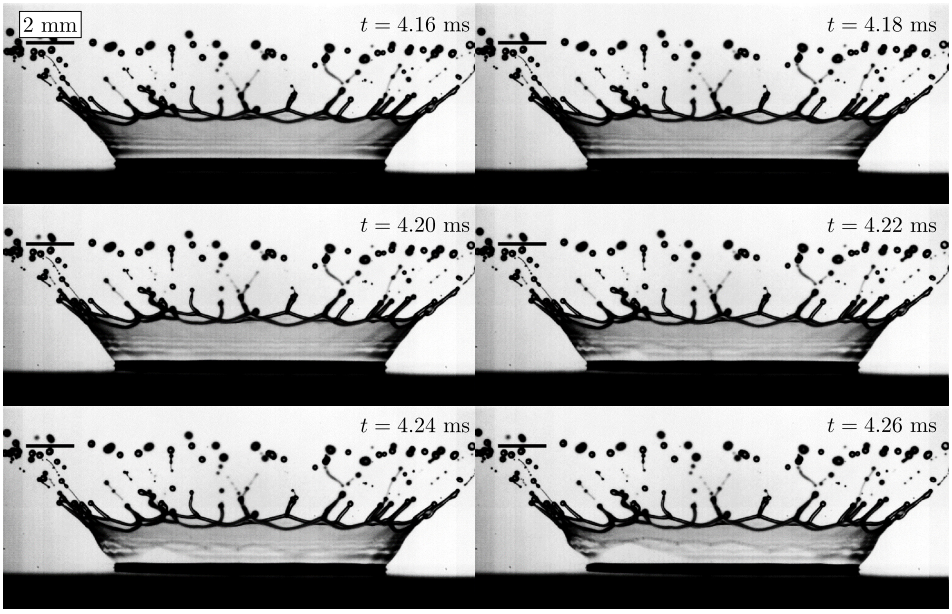

Figure 5.6: Consecutive images showing multiple holes forming and leading to corona detachment. The contrast of the images has been increased to make the rupture better visible. Impact parameters are: $D_0 = 2\,\mathrm{mm}$, $U_0 = 4.23\,\mathrm{m/s}$, $H_{\mathrm{f}0} = 83\,\mu\mathrm{m}$. Film and drop liquid are S10.

the experimental data discussed above $k \sim 10^2$, which yields $\tau_{\mathrm{nucl}} \sim 10^{-4}\,\mathrm{s}$. This value of k is intrinsically linked to the turbulence generation near the bottom of an impacting drop. First of all, the generation process would cease when the characteristic Reynolds number $\mathrm{Re_i}$ would diminish to the level characteristic of a laminar flow, say to $\mathrm{Re}_{il} \sim 10^4$.

Taking for the estimate the drop impact velocity $U_0 \sim 10^2\,\mathrm{cm/s}$, the drop diameter $D_0 \sim 3\,\mathrm{mm}$, and the kinematic viscosity $\nu \sim 10^{-6}\,\mathrm{m^2/s}$, one finds that the angle between the slope of the drop generatrix and the underlying horizontal $\alpha_d = \alpha_{dl} \approx 10^\circ$ corresponds to $\mathrm{Re}_{il} = (U_0 D_0/\nu)\cot\alpha_{dl} \approx 10^4$. Accordingly, the duration of the turbulence generation process is $\tau_{\mathrm{gen}} \sim D_0/(2U_0\cot\alpha_{dl}) \sim 10^{-4}\,\mathrm{s}$. During the period of τ_{gen}, 'large' turbulent eddies are generated and then undergo a cascade of instabilities, breaking them into Kolmogorov dissipative eddies. The characteristic time scale τ_0 of these 'large' eddies is related to the characteristic time scale of Kolmogorov dissipative eddies τ_η by the following expression: $\tau_\eta/\tau_0 \sim \mathrm{Re_i}^{-1/2}$ (Pope, 2001). Accordingly, during the turbulence generation regime, say at $\mathrm{Re_i} \sim 10^5$, $\tau_0 \sim \tau_\eta \mathrm{Re_i}^{1/2} \sim 3\times10^{-4}\mathrm{s}$. This estimate shows that during the time of the order of $\tau_{\mathrm{gen}} + \tau_0 \sim 4\times10^{-4}\,\mathrm{s}$, Kolmogorov eddies would

be formed, swept into the corona and, acting collectively, nucleate supercritical spontaneously growing holes. On the other hand, $k\tau_\eta \sim \tau_{\rm gen} + \tau_0 \sim 4 \times 10^{-4}$ s, because the critical hole nuclei of the order of $r_* \sim 2.18 h_c \sim 2.18$ µm are still invisible in the experiment, and only holes of the order 19-37 µm could be resolved by the camera. Taking for the estimate the least visible hole radius as $R_h \sim (20-40)h_c$, one finds the time required for such a hole to grow as $\tau_{\rm hole} \sim R_h/u_{\rm tc}$, which with the help of Eq. (A.31) yields $\tau_{\rm hole} \sim (20-40)h^{3/2}\rho^{1/2}/(2\sigma)^{1/2} \sim 10^{-5}$ s (according to Table 3.1 the values of $\rho \sim 10^3$ kg/m^3 and $\sigma \sim 18$ mN/m were used for the estimate). This time is to be added to $\tau_{\rm gen} + \tau_0$ and thus, the corona detachment time is estimated as $t_{\rm d} = \tau_{\rm gen} + \tau_0 + \tau_{\rm hole} \sim 4.1 \times 10^{-4}$ s. On the other hand, the data in Fig.s 5.2 and 5.5 reveal $t_d \sim 1$ ms, in reasonable agreement with the estimate. Note also that the above estimates reveal that $k \sim (\tau_{\rm gen} + \tau_0)/\tau_\eta$. The theoretically estimated value is $k \approx 10^2$.

Note that the number of physical parameters which determine the corona detachment time t_d is now reduced to only four: the density ρ, the kinematic viscosity ν, the surface tension σ, and the film thickness at the wall $H_{\rm f0}$. These four parameters involve three independent units, and thus, according to the Buckingham Pi-Theorem (Yarin, 2012), the dimensionless corona detachment time $\bar{t}_{\rm d} = t_{\rm d}/(H_{\rm f0}^2/\nu)$ should depend on a single dimensionless group, denoted here as the Corona number Co. Accordingly, Eq. (A.45) yields

$$\bar{t}_d \approx 3.37 k^{1/3} {\rm Co}^{1/3}, \qquad {\rm Co} = \frac{\rho\nu^2}{\sigma H_{\rm f0}} \tag{5.6}$$

To test this dimensionless law, the dimensionless detachment time $\bar{t}_d$ is plotted against the right-hand side of Eq. (5.6) using the value $k = 73.43$ in Fig. 5.7. As this figure indicates, the main dependency of $\bar{t}_d$ is indeed captured by the Corona number, although the scatter seen in this diagram suggests that a further second-order dependence is not yet fully captured with this scaling.

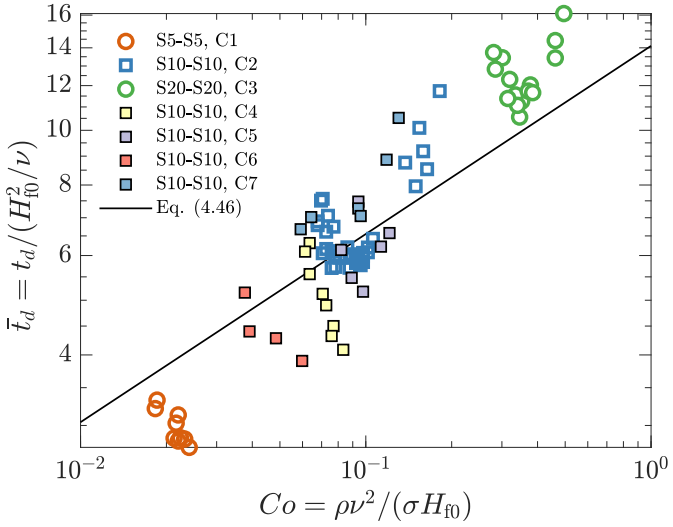

Figure 5.7: Dimensionless time of detachment $\bar{t}_d$ over the Corona number Co. The black line represents Eq. (5.6) with $k = 73.43$.

5.4. Equivocal effects of viscosity

Equivocal observations are made regarding the effect of viscosity on the crown stretching. On the one hand, the approach described in Sec A.3 is based on an inviscid theory and the resulting Eq. (A.28) agrees well with the experiments. On the other hand, it was shown in the previous Chapter 4 that viscous forces decelerate the flow in the lamella until it comes to a complete stop and the lamella reaches its residual height h_{res}. This result suggests that viscous effects in the lamella may play an additional role in the stretching of the crown sheet. To consider this in more detail, the characteristic times of the boundary layer are compared with those of the corona detachment. For example, in cases 1 to 3, where the viscosity is varied from (5 to 20 mm^2/s), the time at which h_{res} is reached is in the order of $t_{\mathrm{res}} \approx$ 2-3 ms (cf. Fig. 4.3). Although t_{res} is practically independent of H_{f0} in the investigated range, these times are comparable to the observed times of detachment presented in Fig. 3 ($0.8\,\mathrm{ms} < t_d < 3\,\mathrm{ms}$ for cases 1 to 3). A complete stop of the flow at the centre of the impact region would inevitably lead to a stretching of the lamella near the crown base and, consequently, to a thinning of the crown sheet. The typical time for the expansion of the viscous boundary layer for drop impact onto dry substrates, obtained in Roisman et al. (2009b) is $t_\nu = 0.6 D_0/U_0 Re^{1/5}$ which represents the time when the viscous boundary layer intersects with the interface of the lamella. Taking this relation for an estimate, t_ν would be $t_\nu \approx 1.2 - 1.6\,\mathrm{ms}$ for cases 1-3, depending on the viscosity. This time is comparable to the observed times of detachment, which implies that viscous effects may also affect the lamella flow preceding the corona detachment.

However, considering one of the most extreme cases with a very small initial film thickness of $H_{\mathrm{f0}} = 31\,\mu\mathrm{m}$ (with the impact parameters of case 2), the time of detachment $t_d = 0.8\,\mathrm{ms}$ is clearly smaller than $t_\nu = 1.4\,\mathrm{ms}$, revealing that corona detachment can occur before the viscous effects become dominant in the lamella flow. Furthermore, considering the times of detachment for identical fluids with varying viscosity from 5 to 20 mm^2/s (cases 1-3), Fig. 5.2 reveals that the time of detachment for those cases strictly coincide, despite the different viscosity.

While it is evident that the boundary layer affects the flow in the lamella in the centre of the impact region, it is not yet clear how the flow in the vicinity of the crown base is affected by viscous effects. In the case shown in Fig. 5.8, the time of detachment $t_d = 1.6\,\mathrm{ms}$ is comparable with $t_\nu = 1.4\,\mathrm{ms}$. Hence, the residual lamella can be observed in the high-speed recordings. Remarkably, the radius of the residual lamella is noticeably smaller than the maximum radius of the crown base. In Fig. 5.8e, a more detailed view of the detaching crown sheet, taken from Fig. 5.8d, is presented. In this figure, a zone between the lamella and the crown sheet with low local film thickness can be identified that is defined here as *stretched film*. In the moments before detachment in the presented case, the residual layer has formed and is almost at rest, while the inertia of the crown sheet causes the liquid to be sucked from the stretching zone and from the wall film into the crown.

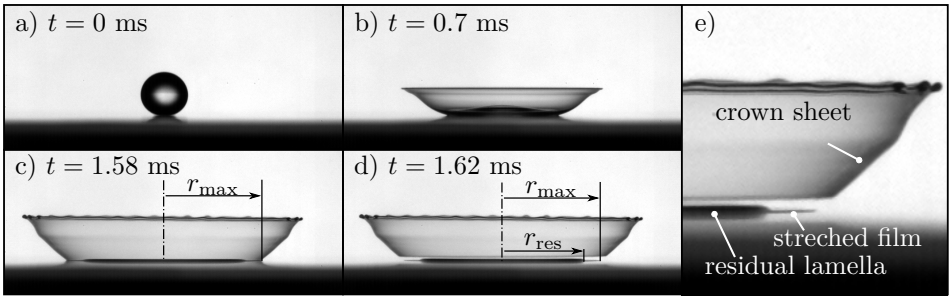

Figure 5.8: Temporal evolution of corona with the maximum corona radius r_{max} shown in c) and the radius of the residual film r_{res} shown in d). Impact parameters: Drop and film liquid is S10, $U_0 = 3.2\,\mathrm{m/s}$, $D_0 = 2\,\mathrm{mm}$, $H_{f0} = 52\,\mu\mathrm{m}$. Zoomed in section of d) presented in e) showing the geometry of the lamella in the vicinity of the crown base shortly after detachment.

The inertia of the crown sheet dominates this flow in the neck region of the crown, which can therefore be considered inviscid. A sketch of this situation is shown in Fig. 5.9. Note that this streched film region has also been observed in other studies Kuhlman and Hillen N. l., 2016 where the drop impact onto liquid films was investigated for $0.2 < \tilde{\delta} < 1$.

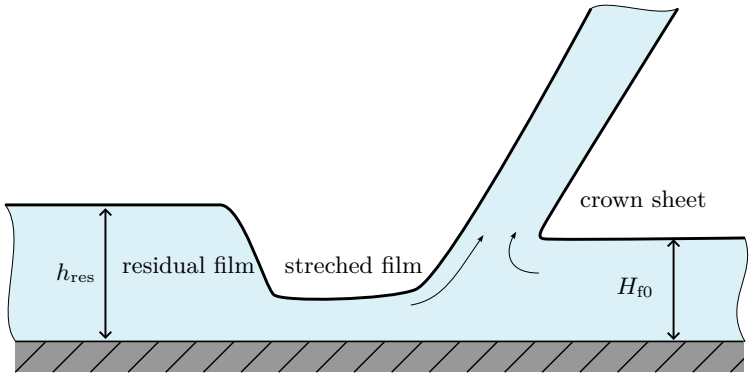

Figure 5.9: Sketch showing the stretched region of the lamella near the crown base.

Although reality seems to be more complicated than represented in the inviscid model that leads to Eq. (A.28) (cf. Appendix. A) the predicted $h_c \sim 1/\tilde{t}$ scaling agrees very well with the experimental observations.

5.5. Conclusions

In this chapter the impact of a liquid drop onto a solid substrate pre-wetted by a film of the same or another liquid is studied, and a fascinating phenomenon of a complete, almost instantaneous detachment of the crown sheet from the pre-existing liquid film on the wall is observed. The viscosity and the viscosity ratio of these liquids is varied over a wide range, through which conditions for a detachment of the crown liquid sheet from the wall film could be experimentally investigated.

Focus was then placed on the physics behind the almost instantaneous and uniform corona detachment and in cooperation with Prof. Yarin (University of Illinois Chicago) a theory was proposed to predict the time of corona detachment, based on the thinning of the crown wall. The breakup of liquid sheets is a fundamental step in numerous atomizers, such as pressure swirl, flat fan nozzles, or as a limiting factor in thin-film coating processes. Knowing the instant of liquid sheet breakup, is a first step to predicting drop size distributions in atomization processes. This will undoubtedly involve adjustment of perturbation characteristics, accounting for the disturbance levels present in the liquid sheet; however, the approach could remain unchanged as in Bang et al. (2023) who investigate the breakup of swirling films that are issued from a pressure-swirl atomizer.

The thinning of the crown sheet with time is predicted theoretically, exhibiting good agreement with experimental findings. This is related to the fact that the crown stretching in time appears to be the dominant process, which determines the crown sheet thinning. For this comparison between the theory and experiment, the Taylor-Culick relation was employed as a means for measuring the local, instantaneous thickness of the crown sheet at or near the time of rupture. This was made possible by the use of high-speed videos, which could capture the movement of the free rim at the perimeter of the rupture holes in the crown sheet. This method can be applied as a film thickness measurement of other rupturing liquid films.

It is shown that an ongoing thinning of the crown sheet with time makes the nucleation of 'super-critical' (by radius) holes more probable, i.e., those holes whose growth in time is sustained by a decrease in the total surface energy in the system 'crown sheet with a hole surrounded by a free rim'. Accordingly, growth of super-critical holes is shown to be energetically favorable. The hole nuclei are attributed to velocity fluctuations resulting from the strong shear field at the interface of the impacting drop and the pre-existing liquid film on the wall. Being entrained in the crown sheet, these random velocity fluctuations rupture the hole nuclei with a high probability if the sheet is sufficiently thin (~ 1 µm). That explains why a 'perfect corona detachment' (with a sharp uniform cut-off) happens at its base, where the disturbances are entrained, resulting almost instantaneously in hole nuclei, which rapidly increase in size and merge. The probability of a system of 'velocity fluctuations and a critical hole' is given by the Gibbs distribution rooted in the microcanonic δ-functional distribution of thermodynamics.

Moreover, the growth process of the super-critical holes in time is described using the Taylor-Culick formula for the velocity of propagation of a free rim over a crown sheet, and thus the time required for super-critical holes to break the intact crown sheet up is predicted in the framework of the percolation theory. This is the time of crown detachment t_d, and it is shown theoretically that this time is related to the thickness of the pre-existing liquid film on the wall H_{f0} by the following scaling law: $t_d \sim H_{\mathrm{f0}}^{5/3}$. This theoretical scaling appears to be reliable if the drop and film liquid are the same, although not all secondary effects are captured. In the case of dissimilar liquids in the impacting drop and the pre-existing liquid film on the wall, the experimental data show that the scaling apparently changes slightly depending on the viscosity ratio.

6. An imaging technique for determining the volume fraction of two-component droplets of immiscible fluids [1]

Droplets within droplets occur in numerous situations in which two immiscible liquids interact, for instance, binary drop collisions or when a drop of one liquid impacts onto a film of a different liquid, ejecting secondary droplets containing both liquids. In framework of this dissertation, an imaging technique for determining the volume fraction of each liquid component in such two-component droplets is introduced, in which images of the same drop from two perpendicular perspectives are used. The processing of these images is supported by a machine learning algorithm (i.e. SVM), which is taught using synthetically generated images and validated on droplets with known mixture fractions placed in an acoustic levitator. An overview of the individual steps in the development process is given in Fig. 6.1. The underlying methods, which are the ray tracing tool, the levitator experiment and the splash experiment, are discussed in detail in Chapter 3. In this chapter, first, the ray tracing tracing tool is used to identify parameters that influence the projected image of a two-component drop. These results are considered in the design and training of the SVM, which is described in the subsequent Sec. 6.2. In Sec. 6.3, the predictions of the trained SVM are validated by synthetic and experimental data. Finally, the application of this technique is demonstrated by measuring the volume fraction in splashed secondary droplets following the impact of a drop of one liquid onto a film of a different liquid. The results of which are presented in Sec. 6.4.

6.1. Projected image of a two-component drop

A comparison between an actual two-component droplet and a corresponding synthetic image is displayed in Fig. 6.2. In the figure the known volume fraction of the droplet imaged in Fig. 6.2a was used in the ray tracing tool and the eccentricities of the inner drop were adjusted iteratively until the synthetic image in Fig. 6.2b

[1] Part of this chapter is published in Stumpf et al. (2022b), used under CC BY 4.0.

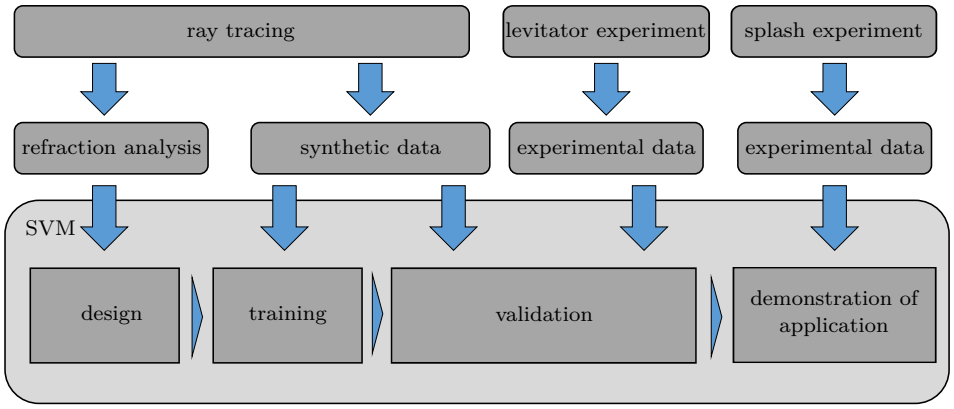

Figure 6.1: Process of developing an imaging technique for volume fraction determination.

was similar to that in Fig. 6.2a. The resulting area ratio and eccentricities collated very closely to those from the experiment, verifying the ray tracing approach for simulating the light scattering from such two-component droplets.

(a) **(b)**

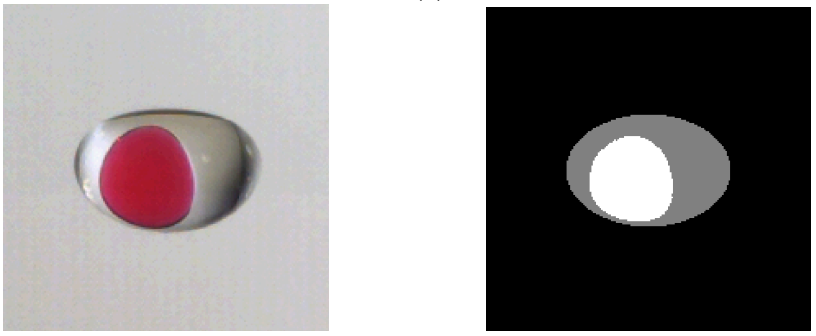

Figure 6.2: a) Levitated two-component droplet of red coloured water and silicone oil ($\nu = 20 \times 10^{-6}$ m^{2}s^{-1}), $V_{\mathrm{frac}} = 0.13$, $A_{\mathrm{ratio}} = 0.41$, $e_{\mathrm{x,proj}} = -0.21$, $e_{\mathrm{z,proj}} = -0.15$, $\varepsilon = 0.68$. b) Projected view on a two-component droplet modeled after (a) using ray tracing resulting in $A_{\mathrm{ratio}} = 0.41$, $e_{\mathrm{x,proj}} = -0.2$, $e_{\mathrm{z,proj}} = -0.17$

The influence of V_{frac} on the projected A_{ratio} is displayed in Fig. 6.3a. For this computation spherical droplets are considered for three cases with varying positions of the inner droplet in the x direction as illustrated in Fig. 6.3b. In the first case

the inner droplet is located on the front side facing the observer; in the second case the inner droplet is in the center; and in the last case the inner droplet is on the backside of the outer droplet. Three conclusions can be drawn from these results.

- The A_{ratio} depends strongly on the V_{frac} and e_i, which means that a prediction of V_{frac} by only the A_{ratio} is not possible unambiguously.
- There is a limit when the A_{ratio} reaches unity, since no information about the inner droplet position can be extracted anymore and the outer droplet appears as if it is composed of only one component. The limiting V_{frac}, indicated by the dashed lines in the figure, increases the closer the inner droplet is located to the observer.
- The slope of the curves decreases the closer the inner droplet is positioned to the front side, allowing a more accurate volume fraction quantification.

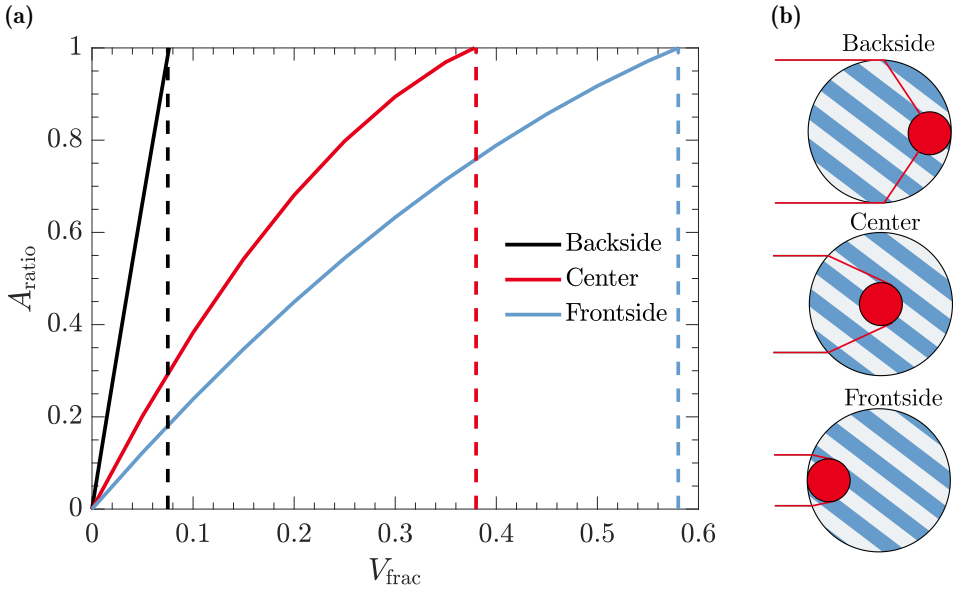

Figure 6.3: a) Relation between V_{frac} and A_{ratio} in dependence of the relative position of the inner droplet ($e_y = e_z = 0$, $n_{\mathrm{l}}/n_{\mathrm{g}} = 1.41$). Dashed lines represent the V_{frac} for which the $A_{\mathrm{ratio}} = 1$. b) Light ray paths of a two-component droplet in sectional view, resulting in varying A_{ratio}.

As can be seen from Fig. 6.3, information about the position of the inner droplet is necessary to determine V_{frac}. For this reason a second imaging perspective, orthogonal to the first one, is added, enabling depth perception. Figure 6.4a shows

a schematic sectional view from above, whereas Fig. 6.4b shows the corresponding projected images from the two perspectives. The location of the inner droplet can be estimated by considering the projected eccentricities $e_{\mathrm{i,proj}}$ from both perspectives. In the present example both projected eccentricities $e_{\mathrm{x,proj}}, e_{\mathrm{y,proj}}$ are on the left side of the two-component droplet center, thus the position of the inner droplet is in the upper left quadrant of the sectional view. Moreover, the additional information from the second projected area ratio A_{ratio} can improve the volume fraction estimation. The further the inner droplet moves away from the centre of the outer droplet, the larger are the shape and size differences on the projected images.

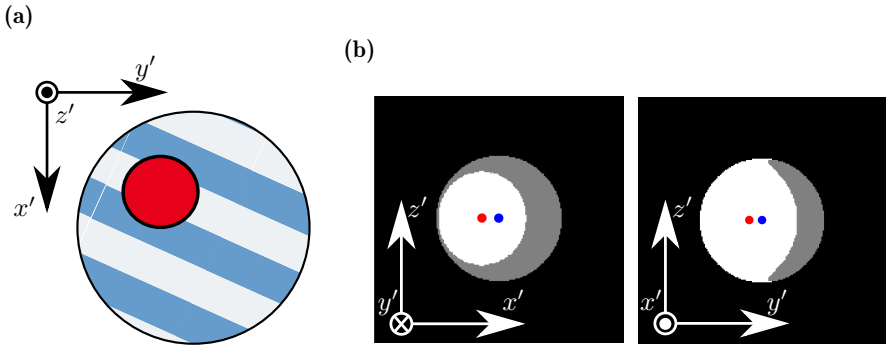

Figure 6.4: a) Schematic of a sectional view of the two-component droplet. b) Corresponding projected images from two sides. The blue and red dots represent the center of mass of the two-component droplet and the projected area, respectively.

6.2. Description of method

It becomes apparent that due to the influence of refraction inside the two-component droplet the real position of the enclosed droplet cannot be determined unambiguously. Only the projected eccentricities $\vec{e}_{i,\mathrm{proj}}$ can be measured directly from the recordings. This makes direct solution of the inverse problem difficult. On the other hand, the projected A_{ratio} in combination with $\vec{e}_{i,\mathrm{proj}}$ do include information about V_{frac}. In order to utilise this information to determine the V_{frac} a support vector machine (SVM) is used. The SVM is a methodology from the field of machine learning, first introduced by Cortes and Vapnik, 1995, which has become widely used for solving classification problems (Awad and Khanna, 2015).

6.2.1. SVM for volume ratio determination

The aim of using a SVM in the context of this study is to provide an algorithm, which is able to predict a volume fraction $\hat{V}_{\mathrm{frac}}$ based on experimentally observable features, summarized in an observation vector $\vec{b}$.

SVMs belong to the category of supervised learning methods, meaning that they are trained with labeled data. With the previously described ray tracing approach this labeled data can be easily provided because the V_{frac} of every synthetically generated droplet image pair is known. The output size, in this case $\hat{V}_{\mathrm{frac}}$, is divided into a fixed number of bins each of which is assigned to a specific class k. After training, a decoding function $d(\vec{b})$ can be solved for every class, i.e. volume fraction bin. The class that is then predicted by the SVM based on the observation $\vec{b}$, is determined by solving the following maximization problem:

$$\hat{V}_{\mathrm{frac}} = \arg\max_{k} (1 - |d|). \tag{6.1}$$

A detailed description of this procedure can be found in Sec. 2.2.2.

To train a SVM with the aim to predict $\hat{V}_{\mathrm{frac}}$, first a set of classes has to be defined. It becomes apparent from Fig. 6.3 that the projected A_{ratio} is close to unity for high V_{frac} even if the inner droplet is positioned on the side facing the observer. The V_{frac} of cases with $A_{\mathrm{ratio}} \approx 1$ cannot be determined unambiguously, since the projected image of the droplet contains limited information. A reasonable trade off is to limit the measuring range of V_{frac} between 0 and 0.5. To illustrate these proportions with an example: When the inner droplet is positioned exactly in the center of the two-component drop at $V_{\mathrm{frac}} = 0.5$ the inner drop would have already 80% of the total drop diameter. This measuring range is then divided into equal bin sizes of 0.025 resulting in 21 discrete classes each representing 5% intervals of the upper measuring range limit.

In Sec. 6.1 it is shown that the projected A_{ratio} depends on $V_{\mathbf{frac}}$, the refractive index $n_{gl} = n_l/n_g$, the relative position e_i of the inner drop and the aspect ratio ε of the two-component drop. With the aim to determine V_{frac} the information of A_{ratio}, n_{gl}, ε and e_i must therefore be taken into account. Since it is not possible to directly determine the exact position of the inner droplet from the recordings, its position is estimated by considering the center of the projected area of the inner droplet in each perspective image $e_{i,\mathrm{proj}}$, with $e_{i,\mathrm{proj}}$ being a two-dimensional vector as depicted in Fig. 3.8b. The SVM is trained for a fixed $n_{\mathrm{l}}/n_{\mathrm{g}} = 1.41$ of silicone oil, thus the observation vector $\vec{b}$ becomes

$$\begin{aligned}\vec{b} = [&\varepsilon, A_{\mathrm{ratio},1}, A_{\mathrm{ratio},2},\\ &e_{x,\mathrm{proj},1}, e_{z,\mathrm{proj},1}, e_{y,\mathrm{proj},2}, e_{z,\mathrm{proj},2}].\end{aligned} \tag{6.2}$$

The area ratios can be summarized in $A_{\text{ratio, p}}$ and the eccentricities in $e_{i,\text{proj},p}$, where the subscript $p \in [1,2]$ denotes the respective perspective 1 or 2 and the subscript i denotes the components of the eccentricity vector. The classification is based on these seven features.

In the next step the algorithm needs to be trained, i.e. the hyperplanes for the l= 210 binary classifiers need to be found. For this purpose, 67500 synthetic observations $\vec{b}$ were generated. For each observation two orthogonal projections are generated, as was illustrated in Fig. 6.4. The V_{frac} and the position of the inner droplet e_i are randomly varied, whereby V_{frac} is limited to the interval $[0, 0.5]$ and e_i is constrained by the condition that the inner droplet must be wholly within the outer droplet. An image processing script based on the Matlab image processing toolbox is then used to extract $A_{\text{ratio},p}$, ε and $e_{i,\text{proj},p}$ from the synthetically generated image pairs. These quantities are then combined in $\vec{b}$ and each observation is labeled with the V_{frac} it was generated with.

Using the Matlab Machine learning toolbox, the SVM is then trained based on this large set of labeled data. During the training process a *K-fold cross-validation* technique is applied for validation (Awad and Khanna, 2015). Therefore, the training data set is divided into 5 samples of equal size, whereby four samples are used for training while one sample is used for validation. This step is repeated five times. In order to evaluate the quality of the trained SVM, a classification cost as shown in the matrix of Table 6.1 is used. By means of this matrix, penalties for improper classification can be defined which are then incorporated into further training. The sum of miss-classification costs can also serve as a benchmark to compare different methods of classification. Based on a test sample of synthetic labeled data the cubic SVM has shown the best performance compared to all other available classification methods in the Matlab machine learning toolbox.

Table 6.1: Improper classification cost matrix

		Predicted class				
		k-2	**k-1**	**k**	**k+1**	**k+2**
True class	**k-2**	0	0.25	0.75	2	2
	k-1	0.25	0	0.25	0.75	2
	k	0.75	0.25	0	0.25	0.75
	k+1	2	0.75	0.25	0	0.25
	k+2	2	2	0.75	0.25	0

The trained SVM can then be used to predict the volume fraction based on an observation vector $\vec{b}$. The output of the SVM contains the d' values for every class, as shown exemplary in Fig. 6.5. Following the relation in Eq. (6.1), the class with the maximum value of $d' = 1 - |d|$ will be the resulting V_{frac} estimate. Thus, d' can

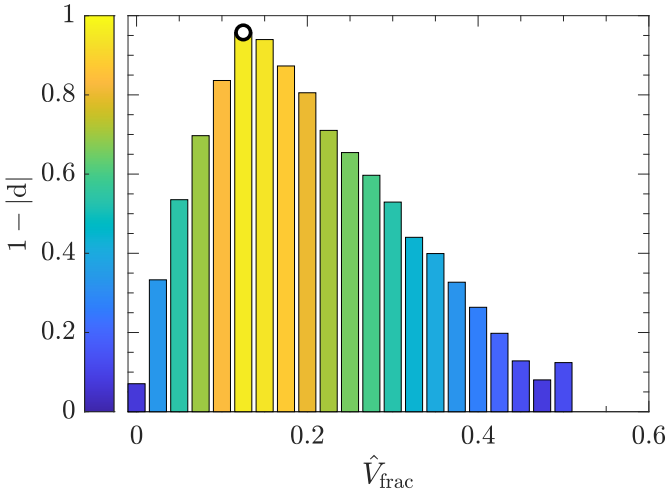

Figure 6.5: Output of decoding function d' for every V_{frac} class after classification. The chosen class with the maximum d' is marked with a circle.

be interpreted as a measure for the likelihood that a particular class best describes the true V_{ratio}. The color shading in Fig. 6.5 is superfluous; however, this shading is introduced here to be consistent with later representation of data in Sec. 6.4.1.

6.3. Validation

6.3.1. Validation using synthetic data

The approach described above is first validated using a large set of synthetically generated data. Each artificial droplet configuration is sorted into one of the 21 V_{frac} classes and classified individually. The mean estimated volume fraction $\langle \hat{V}_{\mathrm{frac}} \rangle$ and standard deviation are calculated from the sorted data. The results are displayed in Fig. 6.6. The red dashed line represents the theoretically correct classification result $V_{\mathrm{frac}} = \hat{V}_{\mathrm{frac}}$. Very good agreement between the mean classified volume fraction $\langle \hat{V}_{\mathrm{frac}} \rangle$ and the actual volume fraction V_{frac} is evident over the entire range of volume fraction. Slight deviations from the mean are apparent for $V_{\mathrm{frac}} > 0.3$. Furthermore, the standard deviation increases, reaching its peak at $V_{\mathrm{frac}} \approx 0.4$.

Both deviations can be explained by the upper limit of volume ratio quantification from Fig. 6.3. This figure shows that inner droplets positioned at the center of the two-component droplet reach a projected area ratio $A_{\mathrm{ratio}} = 1$ for volume fractions above $V_{\mathrm{frac}} > 0.3$. This means that the information content decreases for larger inner droplets as they approach the center of the outer droplet, leading to

an increase in standard deviation.
To determine the influence of the number of bins on the prediction, two further SVMs were trained with 11 and 41 bins respectively. The results of which are shown in Figs.6.7a-b. It can be seen that the number of bins i.e. bin size, has no significant influence on the predictions. With a larger number of bins, the resolution of the predictions can be increased; however, with decreasing bin size this is offset by the deviation of the predictions, so that the overall accuracy can not be improved by making the bin size too small. For a quantitative comparison of the three cases a root-mean-square error of the prediction error V_{RSME} is calculated over all predictions as

$$V_{\mathrm{RSME}} = \sqrt{\frac{1}{N}\sum_{N}(\hat{V}_{\mathrm{frac}} - V_{\mathrm{frac,true}})}. \tag{6.3}$$

Here N is the total number of predictions and $V_{\mathrm{frac,true}}$ is the true value used to generate the synthetic data. The $V_{\mathrm{frac,true}}$ differs from the labeled V_{frac} since the labeled V_{frac} is already discretised by rounding $V_{\mathrm{frac,true}}$ into the bins. In the step from 11 to 21 bins the error reduces from $V_{\mathrm{RMSE},11} = 0.0424$, to $V_{\mathrm{RMSE},21} = 0.0396$, while from 21 to 41 bins the error $V_{\mathrm{RMSE},41} = 0.0392$ only reduces slightly. The segmentation into 21 bins is a compromise, since a further increase of bin number would result in a larger training effort while reducing the RMSE only marginally.

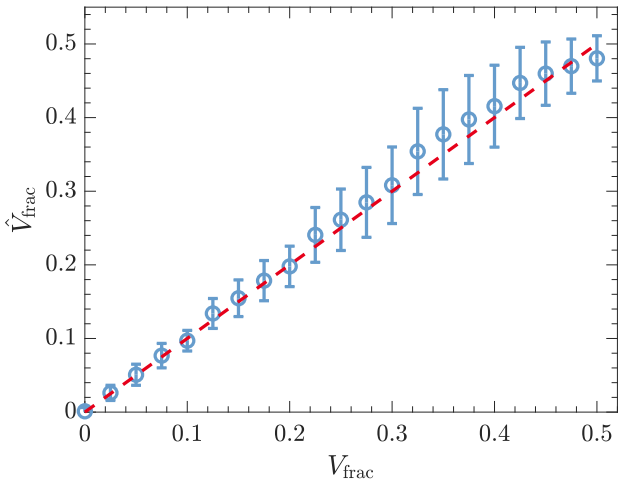

Figure 6.6: Relation between labeled V_{frac} and classified $\hat{V}_{\mathbf{frac}}$. The red dashed line indicates perfect agreement, i.e. $V_{\mathrm{frac}} = \hat{V}_{\mathrm{frac}}$.

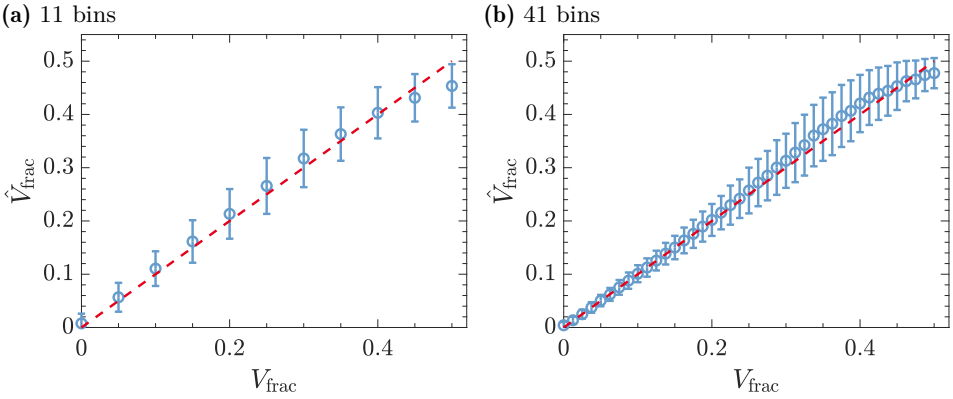

Figure 6.7: Labeled V_{frac} and classified $\hat{V}_{\text{frac}}$ for SVMs trained with a) 11 bins and b) 41 bins respectively.

6.3.2. Experimental validation

Experimental validation was conducted using a total of 32 individual silicon droplets, 20 of which had red coloured water droplets inside and 12 of which had solid, spherical particles ($D = 1\,\text{mm}$) inside. The results of these measurements are shown in Fig. 6.8, in which the 32 experiments are plotted with increasing volume fraction along the X axis according to their identification number (ID). The uncertainty bars correspond to ± 1 px on the respective image, which increase with volume fraction due to the growing influence of the diameter $V_{\text{frac}} = f(D^3_{\text{inner}}/D^3_{\text{total}})$.

The volume fraction $\hat{V}_{\text{frac}}$ estimated from the two images is marked by black markers. The graph shows good agreement between estimated and known values of volume fraction, particularly for $V_{\text{frac}} < 0.3$, similar to the results obtained using synthetic data. Furthermore, the classification results for spherical particles are significantly better than the droplet-in-droplet cases, especially for larger values of V_{frac}. This may be due to an increasing deformation of larger inner droplets.

There are three main reasons why the inner droplet may deviate from the spherical shape, leading to the large disagreement shown in Fig. 6.8 between ground truth and measurement, especially for larger volume fractions. The first is because the outer droplet is deformed due to the pressure forces exerted by the acoustic field to levitate the droplet under gravity. This may lead to a shape distortion of the inner droplet as well. The second reason is that an inner and outer acoustic streaming is generated in the levitator, as is described in Yarin et al., 1998. Finally, the droplet levitated in the pressure node undergoes rotation and centrifugal forces will then act on the inner droplet, possibly also leading to shape distortion. Therefore, since droplet rotation normally plays an insignificant role in practical applications, e.g.

in a corona splash, and furthermore, in practical situations there is no acoustic pressure or acoustic streaming, the results of the particle experiments should be more representative of the achievable accuracy with this method.

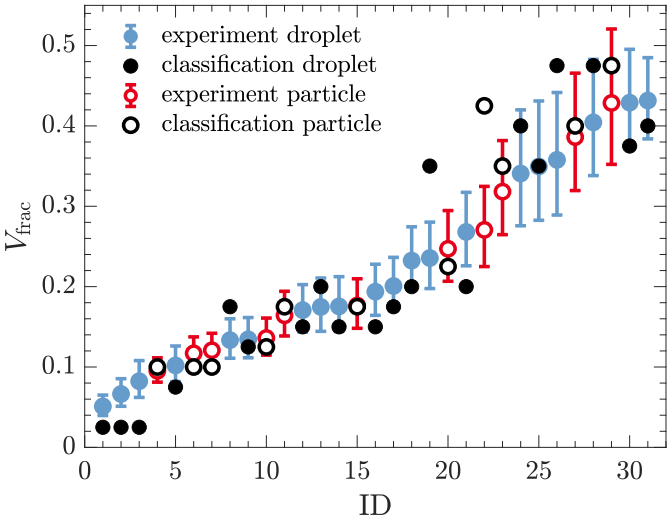

Figure 6.8: Comparison between experimental and classification based volume fraction V_{frac} determination. Blue markers indicate droplet-in-droplet experiments with red colored water inside S20 silicone oil, whereas red markers indicate spherical particles ($D = 1\,\mathrm{mm}$) inside S20 silicone oil droplets. The black symbols correspond to the estimated volume fraction from the experimental images.

6.4. Corona splash experiments

For a further demonstration of this method, measurements were made of secondary, two-component droplets originating from a corona splash. Since the method requires two orthogonal perspectives, a novel setup using mirrors has been employed which is described in Sec. 3.3. A typical single frame image is shown in Fig. 6.9, upon which the trajectories of several droplets have been superimposed. The trajectories have been obtained from frames taken before and after the frame pictured in this figure. Furthermore, the trajectories in the two perspectives are assigned to each other based on characteristics of the individual drops. This procedure is described in more detail in Sec. 3.3.

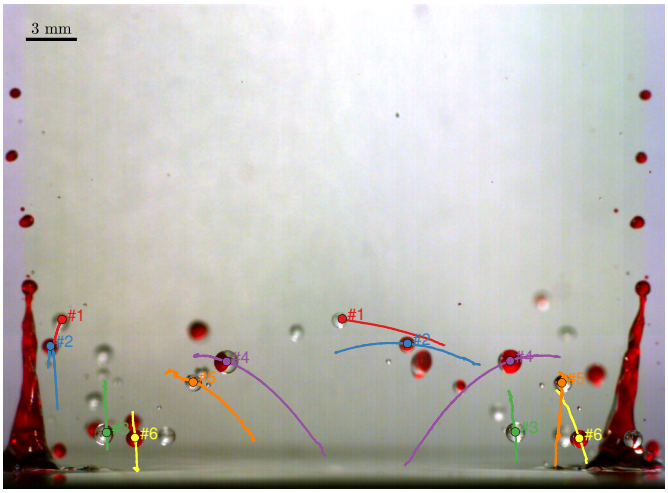

Figure 6.9: Single frame image from the experiment of an red coloured drop impinging onto a silicone oil film $t = 25\,\mathrm{ms}$ after impact. The trajectories of the secondary droplets are highlighted by coloured lines whereby matched pairs have the same colour. The impacting drop is red coloured water (FuH20, $U_0 = 3.2\,\mathrm{m/s}$, $D = 3\,\mathrm{mm}$, We $= 437$, Re $= 10105$) and the film is silicone oil (S10, $H_{\mathrm{f0}} = 600\,\mu\mathrm{m}$, $\tilde{\delta} = 0.2$).

6.4.1. Experimental results

A typical measurement result, obtained by tracking a single two-component secondary droplet is shown in Fig. 6.10. This corresponds to the droplet trajectory labelled #4 in Fig. 6.9. In Fig. 6.10 the complementary decoding function $d' = 1 - |d|$ is expressed in colour as a function of the V_{frac} class between 0 and 0.5. The maximum value of d' for each image frame along the trajectory is marked with a black dot and the volume fraction class in which the black dot lies corresponds to the most likely value of $\hat{V}_{\mathrm{frac}}$. The figure shows a total of 74 frames, equally spaced in time and increasing along the ordinate. As can be seen from this figure, the estimated volume fraction lies between 0.15 and 0.225. The different estimated values of V_{frac} at different trajectory positions (frames) arise because the orientation of the droplet with respect to the two observation directions changes along its trajectory.

A total of 15 drop impact events were performed, resulting in a total of 95 secondary, two-component droplets being tracked from both imaging directions. For each secondary droplet a result similar to that shown in Fig. 6.10 was obtained and a median value of $\hat{V}_{\mathrm{frac}}$ was obtained by summing over all frames in which the droplet could be observed. A median value was used instead of a mean to diminish effects of outliers arising from the image processing, e.g. through out of

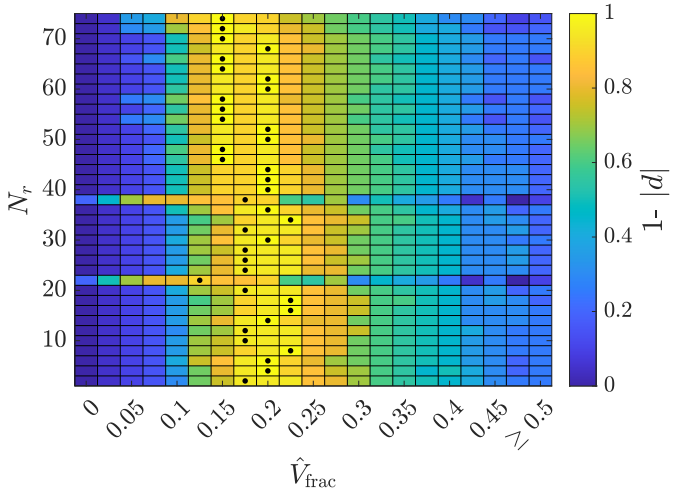

Figure 6.10: Output d' of the complementary decoding function for a set of 74 observations taken at equal times along the trajectory of a single two-component droplet, plotted as a function of the N_r classes of $\hat{V}_{\mathrm{frac}}$. For reasons of presentability only every second result is shown. The maximum d', i.e. the most likely value of V_{frac}, is marked with a black dot for each frame.

focus blurring. In the case of Fig. 6.10 this median value results in $\hat{V}_{\mathrm{frac}} = 0.175$. A histogram of the obtained median volume fractions was then computed and is shown in Fig. 6.11. By far the most frequently encountered droplets are those with no embedded droplet, i.e. for $\hat{V}_{\mathrm{frac}} = 0$. The frequency of droplet occurrences for the class at $\hat{V}_{\mathrm{frac}} = 0.5$ must be interpreted as $\hat{V}_{\mathrm{frac}} \geq 0.5$, since above a value of 0.5 no distinction regarding the true value can be made. This result cannot be verified, since ground truth is not known and no alternative measurement technique is available for comparison. Fig. 6.11 is therefore intended only as an illustration of what results can be derived from the measured values of $\hat{V}_{\mathrm{frac}}$.

6.5. Discussion and conclusion

Two further aspects concerning the accuracy of the measurements using this technique should be discussed. For one, the variance of the $\hat{V}_{\mathrm{frac}}$ estimates from consecutive frames appears to increase with increasing values of V_{frac}. This was observable in Figs. 6.6 and 6.8. Indeed, when $A_{\mathrm{ratio}} = 1$, the uncertainty becomes a maximum and it is reasonable to assume that the uncertainty grows monotonically between values of A_{ratio} between 0 and 1. The second issue is the question: to what degree does the accuracy depend on the number of image pairs captured along a

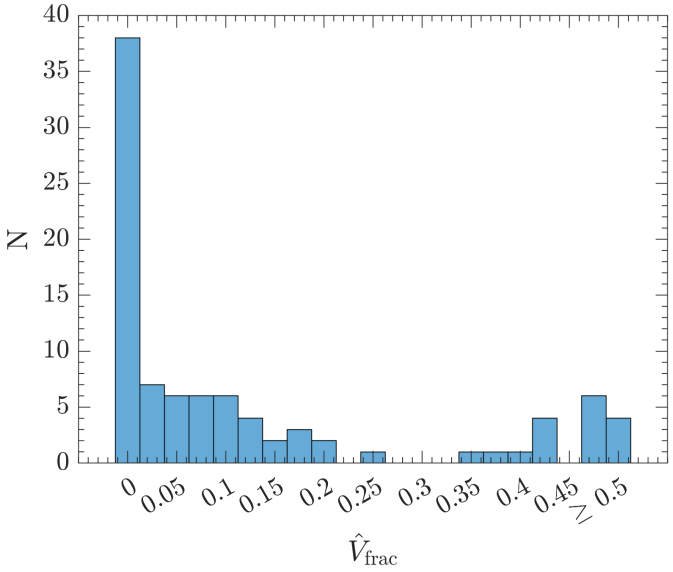

Figure 6.11: Histogram of $\hat{V}_{\mathrm{frac}}$ measured from 95 two-components droplets originating from 15 drop impact events. The impact parameters are held constant and are the same as exemplified in Fig. 6.9.

droplet trajectory? For instance, if the droplet does not change its orientation or distance from the focal plane of each observation direction with time, then identical images will be obtained for each frame. This results in a large amount of data, but no new information. In such a case, one single frame would suffice to estimate V_{frac}.

To investigate these two aspects, the ray tracing tool outlined in Sec. 3.3.1 can be used. By generating synthetic images and processing these as though they were measured images with known values of V_{frac}, the accuracy of the estimators can be investigated. This has been performed for exemplary values of V_{frac}, whereby each image pair used a random selection of $e_{i,\mathrm{proj},p}$ values at a fixed droplet deformation of $\varepsilon = 1$. Using random values ensures that each new data set (image pair) represents also new information. The results of this exercise is shown in Fig. 6.12 from which the following observations can be made:

- The mean error and its deviation decrease faster for smaller values of V_{frac}. Only a few data sets (frames) are necessary for a reliable prediction if V_{frac} is relatively small.

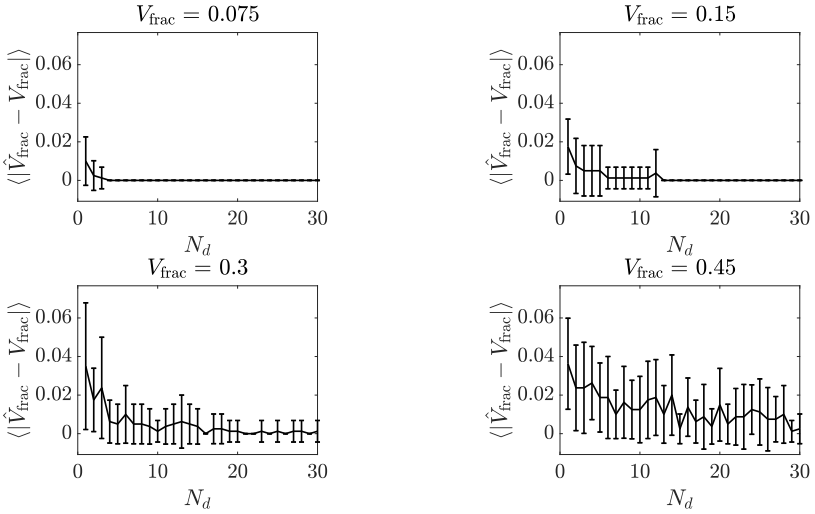

Figure 6.12: Relation between the number of available data sets for classification (N_d) and the mean absolute error between known and estimated volume fraction $\langle\|\hat{V}_{\text{frac}} - V_{\text{frac}}\|\rangle$.

- There is virtually no error at $N_d = 30$ for low values of volume fraction, i.e. $V_{\text{frac}} < 0.15$. For larger values of V_{frac} the uncertainty of the estimated volume fraction no longer decreases with increasing number of data sets, as evident from Figs. 6.12b and d.

These observations both suggest that this technique is particularly well suited for applications in which low volume fractions can be expected. In such cases, the required number of image frames is quite modest, whereby this refers to the number of *independent* frames, since the data in Fig. 6.12 was generated using random input values for the observation vector $\vec{b}$. Using a high-speed camera, consecutive images would normally be highly correlated with one another; hence, they would not each be delivering totally new information as with randomly chosen $\vec{b}$ vectors. The time between frames to insure that new, uncorrelated information is obtained would depend on the integral time scale of the image pattern variations, a quantity which would be very specific to a particular application and is therefore, beyond the scope of the present study.

Nevertheless, the fact that reliable $\hat{V}_{\text{frac}}$ estimates can be made with only few image pairs, suggests that shorter segments of the droplet trajectory can be used for processing, for instance by restricting the SVM procedure to images with much less out-of-focus blur. This would also decrease the number of outliers in the estimation procedure and is one of the planned refinements of the present study.

Another field of future study is the application of this technique to examine droplets with embedded solid particles. Such situations arise in encapsulation processes, when solid particles are encapsulated by spraying an atomized liquid into a fluidized bed of particles. After some period, the outer liquid shell solidifies and encapsulates the inner particle, a process common in the pharmaceutical industry. Application of this technique would of course necessitate a clear difference in colour between the solid particle and the surrounding liquid.

The situation of solid particles embedded in an outer liquid droplet also offers an interesting alternative method of validating the measurement technique. If monodispersed particles were used, then the volume fraction would always be known, once the outer drop diameter was determined. This known value could then be compared with the measured value. This would complement the validation presented here using the acoustic levitator.

7. Summary and outlook

Within the scope of this work, the impact of a drop onto a liquid film of the same or another liquid was investigated. For this purpose, an experimental setup was built and put into operation to conduct generic drop impact experiments onto thin liquid films with controlled impact parameters. A chromatic confocal film thickness sensor system was used for precise monitoring of the film thickness before impact and measurements of the lamella thickness during and after the drop-wall-film interaction. Furthermore, a high-speed camera system was used to observe and characterise the drop impact.

Drop impact experiments were conducted for a wide range of impact parameters, systematically varying the drop impact velocity, the drop diameter, the initial film thickness and the ratio of drop and film viscosity. It is shown, that due to a growing viscous boundary layer, the lamella flow is decelerated until it finally stops, and a residual film is formed. Interestingly, the height of this film depends only slightly on the initial film thickness but strongly on the viscosity of the initial film. Based on existing theories for the drop impact onto dry substrates (Roisman, 2009a), a theoretical model is developed that accounts for the viscous boundary layers in both drop and wall film liquid that predicts the height of the residual layer. The theoretical predictions are compared with the experiments showing excellent agreement. Only for viscosity ratios $\kappa^* \geq 3$ does the model overpredict the residual film layer height, which can be explained by the fact that for the highly viscous liquids (S50 and S100) that are used to achieve these high values of κ, the underlying assumptions that are based on a high film Reynolds number are no longer valid. The model validity is further tested by comparing it to data from the literature obtained from numerical simulations of one component drop impact. Remarkably, the influence of $\tilde{\delta}$ on the scaling parameter A is well predicted over a wide range of $\tilde{\delta}$ comprising multiple orders of magnitude ($0.02 \leq \tilde{\delta} \leq 1$), for larger film thicknesses effects of surface tension become increasingly influential.

Moreover, the fascinating phenomenon of corona detachment, the almost simultaneous detachment of the crown from the wall film, was investigated. Numerous experiments varying the viscosity and the viscosity ratio of liquids are conducted through which conditions that lead to a corona detachment were experimentally investigated. The time interval from impact until corona detachment was measured, revealing that it strongly correlates with the initial

film thickness and that corona detachment does not occur anymore if a critical initial film thickness is exceeded. It becomes apparent that the viscosity does not influence the time of detachment if the liquid in the drop and the film are the same. However, the viscosity ratio has a significant influence. Unique experiments were performed where an artificial rupture is inflicted into the crown sheet, and its propagation velocity is measured at instants shortly before the detachment. Utilising the Taylor-Culick relation, the film thickness in the crown sheet can be estimated as a function of time. The measured evolution of the crown sheet thickness is represented well by the predicted $h_c \sim 1/t$ slope obtained in Stumpf et al. (2023). A theoretical analysis of the rupture process reveals that a possible mechanism leading to the corona detachment is the formation of supercritical holes triggered by disturbances emerging from a thin layer at early instants of impact. These holes form Taylor-Culick rims that grow fast, merge and thus undercut the crown sheet. Based on the specific formation rate of supercritical holes and the propagation velocity of the associated rim, the time of detachment t_d can be predicted. The predicted scaling of $t_d \sim H_{f0}^{5/3}$ represents the experimental results well.

Finally, an imaging technique is developed that allows for the determination of the volume fraction of two-component drops that contain immiscible liquids. This technique relies on chromatic images of a drop from two perpendicular perspectives. The evaluation of those images is supported by a machine learning algorithm that is taught using synthetically generated data. The technique is then validated by measuring the volume fraction of single two-component drops with known volume fraction placed in an acoustic levitator. Further application of the method is demonstrated by measuring the volume fraction of secondary droplets that result from a splash of a drop that impacts onto a film of another immiscible liquid. For this, a special drop impact setup is developed that utilises a mirror system that allows observing the drop impact from two perpendicular perspectives with a single chromatic high-speed camera. First, the recordings of the drop impact are analyzed and droplet trajectories are identified. The trajectories are then allocated to each other in the two perspectives enabling the measurement of the volume fraction with the developed technique. While only a few frames of a drop along its trajectory are sufficient to measure the volume fraction, evaluating multiple images along its trajectory ensures certain robustness of the evaluation concerning outliers and errors in the image processing due to reflection or out-of-focus effects. Two-component drops of immiscible liquids occur in drop splashing, drop-drop interactions, in biomedical devices or additive manufacturing (Blanken et al., 2020; Li et al., 2019; Visser et al., 2018; Zhang et al., 2012). The developed technique allows for determining the volume ratios of such two-component droplets without contact.

Outlook

Exciting approaches for further research can be derived from this work. Besides the prediction of the total residual film thickness in Chapter 4, the evolution and residual value of the wall film lamella are described with the theory. Although the excellent agreement of the measurements and the predicted h_{res} speaks for its correctness, the assumed progression of the wall film thickness h_f is not yet validated individually. Hence, additional experiments measuring the thickness of the wall film lamella, for example, by applying LIF methods (Greszik et al., 2011) would be necessary to provide further validation. This quantity could provide valuable information to estimate the influence of transport processes in the film that succeed the impact. In many real-world applications that involve liquids with differing fluid parameters in drop and wall film, the heat flux from the wall is a relevant quantity (i.e. spray cooling). The height of the residual lamella on the heated substrate is necessary information to calculate such heat flux that could be incorporated into future models. Future experiments utilising an infrared camera to measure the heat flux from the wall to the lamella that forms during drop impact onto a heated liquid film could provide valuable data as a basis for further modelling.

Furthermore, the gained findings on the dynamics of the spreading lamella could be used to review and enhance existing crown spreading models and extend them to two-component drop impact. It was shown that viscous effects significantly influence the flow in the lamella near the impact axis and it is expected that this would also influence the flow into the crown sheet. On the other hand, the flow in the crown sheet can be considered inviscid as there is no more contact with a wall. This leads to a complex transition zone at the crown base that still needs to be completely understood. A task for future research would be to incorporate these viscous influences into models that describe the crown sheet thickness. Knowing the residual wall film thickness and the radial expansion of the crown could provide a measure of how much wall film liquid is propelled into the crown. A better understanding of the crown geometry and kinematics, including the evolution of its thickness, is essential to make better predictions about the parameters of the secondary droplets and can also help to model heat transfer and spray cooling.

Also, the developed technique for determining the volumetric composition of immiscible secondary droplets provides the opportunity for further research and development. It is shown that using uncorrelated images for the evaluation provides additional information that reduces the prediction error. However, in high-speed recordings, consecutive frames of a droplet along its trajectory are often highly correlated and do not provide additional information. Therefore, one possibility to further enhance the accuracy of the technique would be to add more perspectives to obtain more uncorrelated information with each set of frames. For this, a new SVM must be trained with synthetically generated data from the respective number of

perspectives. Another approach for future research would be to measure the volume fraction of drops that impact onto a bed of fluidized particles. Such experiments could provide ground truth if the fluidized particles are mono-dispersed. If the particle size is known, once the outer diameter of a droplet encapsulating a particle is determined, the volume fraction is known and can be compared to the predicted value. Moreover, the measured V_{frac} obtained with the present setup can provide valuable benchmark data for validating numerical simulations. In Bagheri et al. (2022b), temporally resolved data on the crown evolution is used to validate a diffuse interface phase field method that is extended to an arbitrary number of phases in Bagheri et al. (2022a). This model can potentially be used to calculate more complex drop-wall-film interactions resulting in a non-axisymmetric crown, including the formation of secondary droplets. Analogously to the previous studies, experimentally determined data, including V_{frac}, can be used for validation and reference.

Bibliography

Abramovich, G. N. (1963). *The Theory of Turbulent Jets*. Boston: The MIT Press.

Agbaglah, G., Josserand, C., and Zaleski, S. (2013). "Longitudinal instability of a liquid rim". *Physics of Fluids* 25.2, p. 022103. DOI: 10.1063/1.4789971.

Albrecht, H.-E., Borys, M., Damaschke, N., and Tropea, C. (2003). *Laser doppler and phase doppler measurement techniques*. Experimental Fluid Mechanics. Berlin, Germany and Heidelberg, Germany: Springer. ISBN: 978-3-662-05165-8.

Alireza, M. K. (2022). "Physics of droplet impact on flexible materials: A review". *Advances in Mechanical Engineering* 14.11, p. 168781322211372. DOI: 10.1177/16878132221137237.

Aljedaani, A. B., Wand, C., Jetly, A., and Thoroddsen, S. T. (2018). "Experiments on the breakup of drop-impact crowns by Marangoni holes". *Journal of Fluid Mechanics* 844, pp. 162–186. DOI: 10.1017/jfm.2018.178.

Allawein, E. L., Schapire, R. E., and Singer Y. (2000). "Reducing multiclass to binary: A unifying approach for margin classifiers". *Journal of Machine Learning Research* 1, pp. 113–141.

Allen, R. F. (1988). "The mechanics of splashing". *Journal of Colloid and Interface Science* 124.1, pp. 309–316. DOI: 10.1016/0021-9797(88)90352-9.

Asadi, S. and Panahi, H. (2011). "A numerical study of a droplet impinging on a liquid surface". *World Academy of Science, Engineering Technology* 5.7, pp. 613–617.

Awad, M. and Khanna, R. (2015). *Efficient Learning Machines : Theories, Concepts, and Applications for Engineers and System Designers*. 1st ed. 2015. Berkeley, CA: Apress. ISBN: 9781430259909.

Bagheri, M., Stumpf, B., Roisman, I. V., Dadvand, A., Wörner, M., and Marschall, H. (2022a). "A unified finite volume framework for phase–field simulations of an arbitrary number of fluid phases". *The Canadian Journal of Chemical Engineering* 100.9, pp. 2291–2308. DOI: 10.1002/cjce.24510.

Bagheri, M., Stumpf, B., Roisman, I. V., Tropea, C., Hussong, J., Wörner, M., and Marschall, H. (2022b). "Interfacial relaxation – Crucial for phase-field methods to capture low to high energy drop-film impacts". *International Journal of Heat and Fluid Flow* 94.2B, p. 108943. DOI: 10.1016/j.ijheatfluidflow.2022.108943.

Bang, B.-H., Ahn, C.-S., Yoon, S. S., and Yarin, A. L. (2023). "Breakup of swirling films issued from a pressure-swirl atomizer". *Fuel* 332.12, p. 125847. DOI: 10.1016/j.fuel.2022.125847.

Banks, D., Ajawara, C., Sanchez, R., Surti, H., and Aguilar, G. (2013). "Effects of drop and film viscosity on drop impacts onto thin films". *Chemical Engineering Science* 23.6, pp. 525–540. DOI: 10.1615/AtomizSpr.2013007494.

Berberović, E., van Hinsberg, N. P., Jakirlić, S., Roisman, I. V., and Tropea, C. (2009). "Drop impact onto a liquid layer of finite thickness: dynamics of the cavity evolution". *Physical Review E* 79.3 Pt 2, p. 036306. DOI: 10.1103/PhysRevE.79.036306.

Bernard, R., Baumgartner, D., Brenn, G., Planchette, C., Weigand, B., and Lamanna, G. (2021). "Miscibility and wettability: how interfacial tension influences droplet impact onto thin wall films". *Journal of Fluid Mechanics* 908, p. 137. DOI: 10.1017/jfm.2020.944.

Bernard, R., Vaikuntanathan, V., Weigand, B., and Lamanna, G. (2020). "On the crown rim expansion kinematics during droplet impact on wall-films". *Experimental Thermal and Fluid Science* 118.6, p. 110168. DOI: 10.1016/j.expthermflusci.2020.110168.

Bhavsar, H. and Panchal, M. H. (2012). "A review on support vector machine for data classification". *International Journal of Advanced Research in Computer Engineering & Technology* 1, pp. 185–189.

Birkhold, F., Meingast, U., Wassermann, P., and Deutschmann, O. (2006). "Analysis of the Injection of Urea-Water-Solution for Automotive SCR DeNOx-Systems: Modeling of Two-Phase Flow and Spray/Wall-Interaction". *SAE Technical Paper* 01, p. 0643. DOI: 10.4271/2006-01-0643.

Bisighini, A., Cossali, G. E., Tropea, C., and Roisman, I. V. (2010). "Crater evolution after the impact of a drop onto a semi-infinite liquid target". *Physical Review E* 82.3, p. D189. DOI: 10.1103/PhysRevE.82.036319.

Blanken, N., Saleem, M. S., Antonini, C., and Thoraval, M.-J. (2020). "Rebound of self-lubricating compound drops". *Science advances* 6.11, eaay3499. DOI: 10.1126/sciadv.aay3499.

Borghese, F., Sindoni, O. I., Denti, P., and Saija, R. (1992). "Optical properties of spheres containing a spherical eccentric inclusion". *Journal of the Optical Society of America A* 9.8, p. 1327. DOI: 10.1364/JOSAA.9.001327.

Boser, B. E., Guyon I. M., and Vapnik, V. N. (1992). "A training algorithm for optimal margin classifiers". *Proceedings of the Fifth Annual Workshop on Computational Learning Theory*, pp. 144–152. DOI: 10.1145/130385.130401.

Breitenbach, J., Kissing, J., Roisman, I. V., and Tropea, C. (2018a). "Characterization of secondary droplets during thermal atomization regime". *Experimental Thermal and Fluid Science* 98.2, pp. 516–522. DOI: 10.1016/j.expthermflusci.2018.06.030.

Breitenbach, J., Roisman, I. V., and Tropea, C. (2018b). "From drop impact physics to spray cooling models: a critical review". *Experiments in Fluids* 59.3, p. 418. DOI: 10.1007/s00348-018-2514-3.

Brenn, G., Prebeg, Z., Rensink, D., and Yarin, A. L. (2005). "Control of spray formation by vibrational excitation of flat-fan and conical liquid sheets". *Atomization and Sprays* 15.6, pp. 661–686. DOI: 10.1615/AtomizSpr.v15.i6.30.

Browne, M. A., Akinyemi, O., and Boyde, A. (1992). "Confocal surface profiling utilizing chromatic aberration". *Scanning* 14.3, pp. 145–153. DOI: 10.1002/sca.4950140304.

Brunton, S. L., Noack, B. R., and Koumoutsakos, P. (2020). "Machine learning for fluid mechanics". *Annual Review of Fluid Mechanics* 52.1, pp. 477–508. DOI: 10.1146/annurev-fluid-010719-060214.

Cao, Y., Tan, W., and Wu, Z. (2018). "Aircraft icing: An ongoing threat to aviation safety". *Aerospace Science and Technology* 75.5, pp. 353–385. DOI: 10.1016/j.ast.2017.12.028.

Chaitra, P. C. and Saravana Kumar, R. (2018). "A review of multi-class classification algorhythms". *International Journal of Pure and Applied Mathematics* 118, pp. 17–26.

Chen, N., Chen, H., and Amirfazli, A. (2017). "Drop impact onto a thin film: Miscibility effect". *Physics of Fluids* 29.9, p. 092106. DOI: 10.1063/1.5001743.

Coppola, G., Rocco, G., and Luca, L. de (2011). "Insights on the impact of a plane drop on a thin liquid film". *Physics of Fluids* 23.2, p. 022105. DOI: 10.1063/1.3555196.

Cortes, C. and Vapnik, V. N. (1995). "Support-Vector Networks". *Machine Learning* 20, pp. 273–297.

Cossali, G. E., Coghe, A., and Marengo, M. (1997). "The impact of a single drop on a wetted solid surface". *Experiments in Fluids* 22.6, pp. 463–472. DOI: 10.1007/s003480050073.

Cossali, G. E., Marengo, M., Coghe, A., and Zhdanov, S. (2004). "The role of time in single drop splash on thin film". *Experiments in Fluids* 36.6, pp. 888–900. DOI: 10.1007/s00348-003-0772-0.

Culick, F. (1960). "Comments on a ruptured soap film". *Journal of Applied Physics* 31, pp. 1128–1129.

Dietrich, T. G. and Bakiri, G. (1995). "Solving multiclass learning problems via error-correcting output codes". *Journal of Artificial Intelligence Research* 2, pp. 263–286. DOI: 10.1613/jair.105.

Dreizler, A., Pitsch, H., Scherer, V., Schulz, C., and Janicka, J. (2021). "The role of combustion science and technology in low and zero impact energy transformation processes". *Applications in Energy and Combustion Science* 7.8, p. 100040. DOI: 10.1016/j.jaecs.2021.100040.

Dzhaugashtin, K. E. and Yarin, A. L. (1977). "Numerical simulation of nonself-similar wall jet". *Journal of Engineering Physics* 32, p. 420. DOI: 10.1007/BF00867030.

Ersoy, N. E. and Eslamian, M. (2019). "Capillary surface wave formation and mixing of miscible liquids during droplet impact onto a liquid film". *Physics of Fluids* 31.1, p. 012107. DOI: 10.1063/1.5064640.

Ersoy, N. E. and Eslamian, M. (2020). "Phenomenological study and comparison of droplet impact dynamics on a dry surface, thin liquid film, liquid film and shallow pool". *Experimental Thermal and Fluid Science* 112, p. 109977. DOI: 10.1016/j.expthermflusci.2019.109977.

Escalera, S., Pujiol, O., and Radeva, P. (2010). "On the decoding process in ternary error-correcting output codes". *IEEE Transactions on Pattern Analysis and Machine Intelligence* 32, pp. 120–134.

Fedorchenko, A. I. and Wang, A.-B. (2004). "On some common features of drop impact on liquid surfaces". *Journal of Fluid Mechanics* 16.5, pp. 1349–1365. DOI: 10.1063/1.1652061.

Forzatti, P. (2001). "Present status and perspectives in de-NOx SCR catalysis". *Applied Catalysis A: General* 222.1-2, pp. 221–236. DOI: 10.1016/S0926-860X(01)00832-8.

Frackowiak, B. and Tropea, C. (2010). "Numerical analysis of diameter influence on droplet fluorescence". *Applied Optics* 49.12, pp. 2363–2370. DOI: 10.1364/AO.49.002363.

Fuller, K. A. (1995). "Scattering and absorption cross sections of compounded spheres III Spheres containing arbitrarily located spherical inhomogeneities". *Journal of the Optical Society of America A* 12.5, p. 893. DOI: 10.1364/JOSAA.12.000893.

Gao, X. and Li, R. (2015). "Impact of a single drop on a flowing liquid film". *Physical Review E* 92.5, p. 053005. DOI: 10.1103/PhysRevE.92.053005.

George, W. K., Beuther, P. D., and Arndt, R. E. A. (1984). "Pressure spectra in turbulent free shear flows". *Journal of Fluid Mechanics* 148, pp. 155–191. DOI: 10.1017/S0022112084002299.

Geppert, A. K. (2019). "Experimental Investigation of Droplet Wall-Film Interaction of Binary Systems". Dissertation. Stuttgart: University of Stuttgart.

Geppert, A. K., Chatzianagnostou, D., Meister, C., Gomaa, H., Lamanna, G., and Weigand, B. (2016). "Classification of impact morphology and splashing/deposition limit for n-hexadecane". *Atomization and Sprays* 26.10, pp. 983–1007. DOI: 10.1615/AtomizSpr.2015013352.

Geppert, A. K., Terzis, A., Lamanna, G., Marengo, M., and Weigand, B. (2017). "A benchmark study for the crown-type splashing dynamics of one- and two-component droplet wall–film interactions". *Experiments in Fluids* 58.12, p. 485. DOI: 10.1007/s00348-017-2447-2.

Ghahfarokhi, P. S., Podgornovs, A., Kallaste, A., Marques Cardoso, A. J., Belahcen, A., and Vaimann, T. (2022). "The oil spray cooling system of automotive traction motors: The state of the art". *IEEE Transactions on Transportation Electrification*, p. 1. DOI: 10.1109/TTE.2022.3189596.

Ghosal, A., Chen, K., Sinha-Ray, S., Yarin, A. L., and Pourdeyhimi, B. (2020). "Modeling polymer crystallization kinetics in the meltblowing process". *Industrial & Engineering Chemistry Research* 59.1, pp. 399–412. DOI: 10.1021/acs.iecr.9b04840.

Gingold, R. A. and Monaghan, J. J. (1977). "Smoothed particle hydrodynamics: theory and application to non-spherical stars". *Monthly Notices of the Royal Astronomical Society* 181.3, pp. 375–389. DOI: 10.1093/mnras/181.3.375.

Gloerfeld, M., Roisman, I. V., Hussong, J., and Tropea, C. (2021). "Measurements and modelling of the residual mass upon impact of supercooled liquid drops". *Experiments in Fluids* 62.10, p. 4520. DOI: 10.1007/s00348-021-03292-7.

Golloch, R. and Merker, G. P. (2005). "Internal combustion engine downsizing". *MTZ worldwide* 66.2, pp. 20–22. DOI: 10.1007/BF03227737.

Gouesbet, G. and Gréhan, G. (2000). "Generalized Lorenz-Mie theory for a sphere with an eccentrically located spherical inclusion". *Journal of Modern Optics* 47.5, pp. 821–837. DOI: 10.1080/09500340008235093.

Greszik, D., Yang, H., Dreier, T., and Schulz, C. (2011). "Laser-based diagnostics for the measurement of liquid water film thickness". *Applied Optics* 50.4, A60–7. DOI: 10.1364/AO.50.000A60.

Guildenbecher, D. R., Cooper, M. A., and Sojka, P. E. (2016). "High-speed (20 kHz) digital in-line holography for transient particle tracking and sizing in multiphase flows". *Applied Optics* 55.11, pp. 2892–2903. DOI: 10.1364/AO.55.002892.

Guildenbecher, D. R., Engvall, L., Gao, J., Grasser, T. W., Reu, P. L., and Chen, J. (2014). "Digital in-line holography to quantify secondary droplets from the impact of a single drop on a thin film". *Experiments in Fluids* 55.3, p. 888. DOI: 10.1007/s00348-014-1670-3.

Gultekin, A., Erkan, N., Colak, U., and Suzuki, S. (2020). "PIV measurement inside single and double droplet interaction on a solid surface". *Experiments in Fluids* 61.10, p. 159. DOI: 10.1007/s00348-020-03051-0.

Guo, Y., Wei, L., Liang, G., and Shen, S. (2014). "Simulation of droplet impact on liquid film with CLSVOF". *International Communications in Heat and Mass Transfer* 53.5, pp. 26–33. DOI: 10.1016/j.icheatmasstransfer.2014.02.006.

Harlow, F. H. and Welch, J. E. (1965). "Numerical calculation of time-dependent viscous incompressible flow of fluid with free surface". *Proceedings of the Royal Society of London. Series A: Mathematical and Physical Sciences* 8.12, p. 2182. DOI: 10.1063/1.1761178.

Heinz, M., Stephan, P., and Gambaryan-Roisman, T. (2021). "Influence of nanofiber coating thickness and drop volume on spreading, imbibition, and evaporation". *Colloids and Surfaces A: Physicochemical and Engineering Aspects* 631.46, p. 127450. DOI: 10.1016/j.colsurfa.2021.127450.

Hirt, C. and Nichols, B. (1981). "Volume of fluid (VOF) method for the dynamics of free boundaries". *Journal of Computational Physics* 39.1, pp. 201–225. DOI: 10.1016/0021-9991(81)90145-5.

Hosseini, S. E. and Butler, B. (2020). "An overview of development and challenges in hydrogen powered vehicles". *International Journal of Green Energy* 17.1, pp. 13–37. DOI: 10.1080/15435075.2019.1685999.

Josserand, C. and Thoroddsen, S. T. (2016). "Drop impact on a solid surface". *Annual Review of Fluid Mechanics* 48, pp. 365–391. DOI: 10.1146/annurev-fluid-122414-034401.

Josserand, C. and Zaleski, S. (2003). "Droplet splashing on a thin liquid film". *Physics of Fluids* 15, p. 1650.

Kandlikar, S. G. and Bapat, A. V. (2007). "Evaluation of jet impingement, spray and microchannel chip cooling options for high heat flux removal". *Heat Transfer Engineering* 28.11, pp. 911–923. DOI: 10.1080/01457630701421703.

Kim, J. (2007). "Spray cooling heat transfer: The state of the art". *International Journal of Heat and Fluid Flow* 28.4, pp. 753–767. DOI: 10.1016/j.ijheatfluidflow.2006.09.003.

Kim, S. C. and Ryou, H. S. (2003). "An experimental and numerical study on fire suppression using a water mist in an enclosure". *Building and Environment* 38.11, pp. 1309–1316. DOI: 10.1016/S0360-1323(03)00134-3.

Kittel, H. M. (2019). "Drop impact onto a wall wetted by a thin film of another liquid". Dissertation. Darmstadt: Technische Universität Darmstadt.

Kittel, H. M., Alam, E., Roisman, I. V., Tropea, C., and Gambaryan-Roisman, T. (2018). "Splashing of a Newtonian drop impacted onto a solid substrate coated by a thin soft layer". *Colloids and Surfaces A: Physicochemical and Engineering Aspects* 553.171–178, pp. 89–96. DOI: 10.1016/j.colsurfa.2018.04.060.

Kolmogorov, A. N. (1962). "A refinement of previous hypotheses concerning the local structure of turbulence in a viscous incompressible fluid at high Reynolds number". *Journal of Fluid Mechanics* 13.1, pp. 82–85. DOI: 10.1017/S0022112062000518.

Kubach, H., Weidenlener, A., Pfeil, J., Koch, T., Kittel, H. M., Roisman, I. V., and Tropea, C. (2018). *Investigations on the influence of fuel oil film interaction on pre-ignition events in highly boosted DI gasoline engines*. DOI: 10.4271/2018-01-1454.

Kuhlman, J. M. and Hillen N. l. (2016). "Droplet impact cavity film thickness measurements versus time after drop impact and cavity radius for thin static residual liquid layer thicknesses". *Experimental Thermal and Fluid Science* 77, pp. 246–256. DOI: 10.1016/j.expthermflusci.2016.04.020.

Lamanna, G., Geppert, A. K., Bernard, R., and Weigand, B. (2022). "Drop impact onto wetted walls: an unsteady analytical solution for modelling crown spreading". *Journal of Fluid Mechanics* 938, p. 555. DOI: 10.1017/jfm.2022.69.

Lamanna, G., Tonini, S., Cossali, G. E., and Weigand, B. (2020). *Droplet Interactions and Spray Processes*. Vol. 121. Cham: Springer International Publishing. ISBN: 978-3-030-33337-9. DOI: 10.1007/978-3-030-33338-6.

Landau, L. D. and Lifshitz, E. M. (2013). *Statistical Physics: Volume 5*. Oxford: Butterworth-Heinemann.

Lee, S. H., Hur, N., and Kang, S. (2011). "A numerical analysis of drop impact on liquid film by using a level set method". *Journal of Mechanical Science and Technology* 25.10, pp. 2567–2572. DOI: 10.1007/s12206-011-0613-7.

Lefebvre, A. H. and McDonell, V. G. (2017). *Atomization and sprays*. Second edition. Combustion. Boca Raton, London, and New York: CRC Press Taylor & Francis Group. ISBN: 978-1498736251. DOI: 10.1201/9781315120911.

Lesser, M. B. and Field, J. E. (1983). "The Impact of Compressible Liquids". *Annual Review of Fluid Mechanics* 15, pp. 97–122. DOI: 10.1146/annurev.fl.15.010183.000525.

Levin, Z. and Hobbs, C. V. (1971). "Splashing of water drops on solid and wetted surfaces: hydrodynamics and charge separation". *Philosophical Transactions of the Royal Society of London. Series A, Mathematical and Physical Sciences* 269.1200, pp. 555–585. DOI: 10.1098/rsta.1971.0052.

Li, E. Q., Thoraval, M.-J., Marston, J. O., and Thoroddsen, S. T. (2018). "Early azimuthal instability during drop impact". *Journal of Fluid Mechanics* 848, pp. 821–835. DOI: 10.1017/jfm.2018.383.

Li, X., Zhang, J. M., Yi, X., Huang, Z., Lv, P., and Duan, H. (2019). "Multimaterial microfluidic 3D printing of textured composites with liquid inclusions". *Advanced Science (Weinheim, Baden-Wurttemberg, Germany)* 6.3, p. 1800730. DOI: 10.1002/advs.201800730.

Liang, G., Guo, Y., and Shen, S. (2014a). "Gas Properties on Crown Behavior and Drop Coalescence". *Numerical Heat Transfer, Part B: Fundamentals* 65.6, pp. 537–553. DOI: 10.1080/10407790.2014.884834.

Liang, G., Guo, Y., Shen, S., and Yang, Y. (2014b). "Crown behavior and bubble entrainment during a drop impact on a liquid film". *Theoretical and Computational Fluid Dynamics* 28.2, pp. 159–170. DOI: 10.1007/s00162-013-0308-z.

Liang, G., Guo Ya-Li, Shen, S., and undefined (2013). "Analysis of liquid sheet and jet flow mechanism after droplet impinging onto liquid film". *Acta Physica Sinica* 62.2, p. 024705. DOI: 10.7498/aps.62.024705.

Liang, G. and Mudawar, I. (2016). "Review of mass and momentum interactions during drop impact on a liquid film". *International Journal of Heat and Mass Transfer* 101, pp. 577–599.

Liang, G. and Mudawar, I. (2017a). "Review of spray cooling – Part 1: Single-phase and nucleate boiling regimes, and critical heat flux". *International Journal of Heat and Mass Transfer* 115, pp. 1174–1205. DOI: 10.1016/j.ijheatmasstransfer.2017.06.029.

– (2017b). "Review of spray cooling – Part 2: High temperature boiling regimes and quenching applications". *International Journal of Heat and Mass Transfer* 115, pp. 1206–1222. DOI: 10.1016/j.ijheatmasstransfer.2017.06.022.

Lott, P., Wagner, U., Koch, T., and Deutschmann, O. (2022). "Der Wasserstoffmotor – Chancen und Herausforderungen auf dem Weg zu einer dekarbonisierten Mobilität". *Chemie Ingenieur Technik* 94.3, pp. 217–229. DOI: 10.1002/cite.202100155.

Lu, L., Pei, Y., Qin, J., Peng, Z., Wang, Y., and Zhu, Q. (2020). "Impingement behaviour of single ethanol droplet on a liquid film of glycerol solution". *Fuel* 256, p. 117820. DOI: 10.1016/j.fuel.2020.117820.

Maliha, M., Stumpf, B., Beyer, F., Kühnert, M., Kubach, H., Roisman, I. V., Hussong, J., and Koch, T. (2022). "Optical investigation on the interaction between a fuel-spray and an oil wetted wall with the focus on secondary droplets". *International Journal of Engine Research* 2, p. 146808742210952. DOI: 10.1177/14680874221095235.

Marston, J. O. and Thoroddsen, S. T. (2008). "Apex jets from impacting drops". *Journal of Fluid Mechanics* 614, pp. 293–302. DOI: 10.1017/S0022112008003881.

Miks, A., Novak, J., and Novak, P. (2010). "Analysis of method for measuring thickness of plane-parallel plates and lenses using chromatic confocal sensor". *Applied Optics* 49.17, pp. 3259–3264. DOI: 10.1364/AO.49.003259.

Moreira, A., Moita, A. S., and Panao, M. R. (2010). "Advances and challenges in explaining fuel spray impingement: How much of single droplet impact research is useful?" *Progress in Energy and Combustion Science* 36, pp. 554–580. DOI: 10.1016/j.pecs.2010.01.002.

Motzkus, C., Gensdarmes, F., and Géhin, E. (2011). "Study of the coalescence/splash threshold of droplet impact on liquid films and its relevance in assessing airborne particle release". *Journal of Colloid and Interface Science* 362.2, pp. 540–552. DOI: 10.1016/j.jcis.2011.06.031.

Mukherjee, S. and Abraham, J. (2007). "Crown behavior in drop impact on wet walls". *Physics of Fluids* 19.5, p. 052103. DOI: 10.1063/1.2736085.

Mundo, C., Sommerfeld, M., and Tropea, C. (1995). "Droplet-wall collisions: Experimental studies on the deformation and breakup process." *International Journal of Multiphase Flow* 21, pp. 151–173. DOI: 10.1016/0301-9322(94)00069-V.

Nikolopoulos, N., Theodorakakos, A., and Bergeles, G. (2005). "Normal impingement of a droplet onto a wall film: a numerical investigation". *International Journal of Heat and Fluid Flow* 26.1, pp. 119–132. DOI: 10.1016/j.ijheatfluidflow.2004.06.002.

Ninomiya, N. and Iwamoto, K. (2011). "PIV measurement of a droplet impact on a thin fluid layer", pp. 11–17. DOI: 10.1063/1.3694683.

Okawa, T., Kubo, K., Kawai, K., and Kitabayashi, S. (2021). "Experiments on splashing thresholds during single-drop impact onto a quiescent liquid film". *Experimental Thermal and Fluid Science* 121.2, p. 110279. DOI: 10.1016/j.expthermflusci.2020.110279.

Okawa, T., Shiraishi, T., and Mori, T. (2006). "Production of secondary drops during the single water drop impact onto a plane water surface". *Experiments in Fluids* 41.6, pp. 965–974. DOI: 10.1007/s00348-006-0214-x.

– (2008). "Effect of impingement angle on the outcome of single water drop impact onto a plane water surface". *Experiments in Fluids* 44.2, pp. 331–339. DOI: 10.1007/s00348-007-0406-z.

Opfer, L., Roisman, I. V., Venzmer, J., Klostermann, M., and Tropea, C. (2014). "Droplet-air collision dynamics: evolution of the film thickness". *Physical Review E* 89.1, p. 013023. DOI: 10.1103/PhysRevE.89.013023.

Osher, S. and Sethian, J. A. (1988). "Fronts propagating with curvature-dependent speed: Algorithms based on Hamilton-Jacobi formulations". *Journal of Computational Physics* 79.1, pp. 12–49. DOI: 10.1016/0021-9991(88)90002-2.

Pan, K.-L. and Law, C. K. (2007). "Dynamics of droplet–film collision". *Journal of Fluid Mechanics* 587, pp. 1–22. DOI: 10.1017/S002211200700657X.

Perez, E. E., Carelli, A. A., and Crapiste, G. H. (2011). "Temperature-dependent diffusion coefficient of oil from different sunflower seeds during extraction with hexane". *Journal of Food Engineering* 105, pp. 180–185. DOI: 10.1016/j.jfoodeng.2011.02.025.

Philippi, J., Lagree, P., and Antkowiak, A. (2016). "Drop impact on a solid surface: short-time self-similarity". *Journal of Fluid Mechanics* 795, pp. 96–135. DOI: 10.1017/jfm.2016.142.

Pope, S. B. (2001). *Turbulent Flows*. Cambridge University Press.

R. Davidson, M. (2002). "Spreading of an inviscid drop impacting on a liquid film". *Chemical Engineering Science* 57.17, pp. 3639–3647. DOI: 10.1016/S0009-2509(02)00266-X.

Raman, K. A., Jaiman, R. K., Lee, T. S., and Low, H. T. (2015). "On the dynamics of crown structure in simultaneous two droplets impact onto stationary and moving liquid film". *Computers & Fluids* 107.056703, pp. 285–300. DOI: 10.1016/j.compfluid.2014.11.007.

Riboux, G. and Gordillo, J. M. (2014). "Experiments of drops impacting a smooth solid surface: a model of the critical impact speed for drop splashing". *Physical Review Letters* 113.2, p. 024507. DOI: 10.1103/PhysRevLett.113.024507.

Richter, S. (2019). *Statistisches und maschinelles Lernen : Gängige Verfahren im Überblick*. Berlin, Heidelberg.

Rieber, M. and Frohn, A. (1999). "A numerical study on the mechanism of splashing". *International Journal of Heat and Fluid Flow* 20.5, pp. 455–461. DOI: 10.1016/S0142-727X(99)00033-8.

Rioboo, R., Bauthier, J., Conti, J., Voue, M., and De Coninck J. (2003). "Experimental investigation of splash and crown formation during singledrop impact on wetted surfaces". *Experiments in Fluids* 35, pp. 648–652.

Rioboo, R., Marengo, M., and Tropea, C. (2002). "Time evolution of liquid drop impact onto solid, dry surfaces". *Experiments in Fluids* 33.1, pp. 112–124. DOI: 10.1007/s00348-002-0431-x.

Roisman, I. V. (2009a). "Inertia dominated drop collisions. II. Ananalytical solution of the Navier–Stokesequations for a spreading viscous film". *Physics of Fluids* 21, p. 052104.

– (2010). "On the instability of a free viscous rim". *Journal of Fluid Mechanics* 661, pp. 206–228. DOI: 10.1017/S0022112010002910.

– (2022). "Hydrodynamic model of a collision of a spherical plastic ice particle with a perfectly rigid substrate". *International Journal of Impact Engineering* 159, p. 104019. DOI: 10.1016/j.ijimpeng.2021.104019.

Roisman, I. V., Berberović, E., and Tropea, C. (2009b). "Inertia dominated drop collisions. I. On theuniversal flow in the lamella". *Physics of Fluids* 21, p. 052103.

Roisman, I. V. and Tropea, C. (2002). "Impact of a drop onto a wetted wall: descriptionof crown formation and propagation". *Journal of Fluid Mechanics* 472, pp. 373–397.

Roisman, I. V., Tropea, C., and Horvat, K. (2006). "Spray impact: Rim transverse instability initiating fingering and splash, and description of a secondary spray". *Physics of Fluids* 16, p. 102104.

Roisman, I. V., van Hinsberg, N. P., and Tropea, C. (2008). "Propagation of a kinematic instability in a liquid layer: Capillary and gravity effects". *Physical Review E* 77, p. 046305.

Samenfink, W., Elsäßer, A., Dullenkopf, K., and Wittig, S. (1999). "Droplet interaction with shear-driven liquid films: analysis of deposition and secondary droplet characteristics". *International Journal of Heat and Fluid Flow* 20.5, pp. 462–469. DOI: 10.1016/S0142-727X(99)00035-1.

Schlichting, H. and Gersten, K. (2017). *Boundary-Layer Theory*. 9th ed. 2017. Berlin Heidelberg: Springer Berlin Heidelberg and Imprint: Springer. ISBN: 9783662529195.

Schmidt, A., Bonarens, M., Roisman, I. V., Nishad, K., Sadiki, A., Dreizler, A., Hussong, J., and Wagner, S. (2021). "Experimental investigation of AdBlue film formation in a generic SCR test bench and numerical analysis using LES". *Applied Sciences* 11.15, p. 6907. DOI: 10.3390/app11156907.

Shaikh, S., Toyofuku, G., Hoang, R., and Marston, J. O. (2018). "Immiscible impact dynamics of droplets onto millimetric films". *Experiments in Fluids* 59.1, p. 329. DOI: 10.1007/s00348-017-2461-4.

Shao, C., Luo, K., Yang, J., Chen, S., and Fan, J. (2015). "Accurate level set method for simulations of liquid atomization". *Chinese Journal of Chemical Engineering* 23.4, pp. 597–604. DOI: 10.1016/j.cjche.2014.07.004.

Sharma, S., Rao, S. J., Chandra, N. K., Kumar, A., Basu, S., and Tropea, C. (2023). "Depth from defocus technique applied to unsteady shock-drop secondary atomization". *Experiments in Fluids* 64.4, p. 977. DOI: 10.1007/s00348-023-03588-w.

Shen, S., Bi, F., and Guo, Y. (2012). "Simulation of droplets impact on curved surfaces with lattice Boltzmann method". *International Journal of Heat and Mass Transfer* 55.23-24, pp. 6938–6943. DOI: 10.1016/j.ijheatmasstransfer.2012.07.007.

Shi, Z.-y., Yan, Y.-h., Yan, F., Qian, Y.-h., and Hu, G.-h. (2008). "A lattice boltzmann method for simulation of a three-dimensional drop impact on a liquid film". *Journal of Hydrodynamics* 20.3, pp. 267–272. DOI: 10.1016/S1001-6058(08)60056-6.

Šikalo, Š. and Ganić, E. N. (2006). "Phenomena of droplet–surface interactions". *Experimental Thermal and Fluid Science* 31.2, pp. 97–110. DOI: 10.1016/j.expthermflusci.2006.03.028.

Sivakumar, D. and Tropea, C. (2002). "Splashing impact of a spray onto a liquid film". *International Journal of Heat and Fluid Flow* 14.12, pp. L85–L88. DOI: 10.1063/1.1521418.

Smith, M. I. and Bertola, V. (2011). "Particle velocimetry inside Newtonian and non-Newtonian droplets impacting a hydrophobic surface". *Experiments in Fluids* 50.5, pp. 1385–1391. DOI: 10.1007/s00348-010-0998-6.

Smith, P., van de Ven, T., and Mason, S. (1981). "The transient interfacial tension between two miscible fluids". *Journal of Colloid and Interface Science* 80.1, pp. 302–303. DOI: 10.1016/0021-9797(81)90186-7.

Son, G. (2003). "Efficient implementation of a coupled level-set and volume-of-fluid method for three-dimensional incompressible two-phase flows". *Numerical Heat Transfer, Part B: Fundamentals* 43.6, pp. 549–565. DOI: 10.1080/713836317.

Sreenivasan, K. R. (1995). "On the universality of the Kolmogorov constant". *Physics of Fluids* 7.11, pp. 2778–2784. DOI: 10.1063/1.868656.

Stauffer, D. (1979). "Scaling theory of percolation clusters". *Physics Reports* 54.1, pp. 1–74. DOI: 10.1016/0370-1573(79)90060-7.

Stauffer, D. and Aharony, A. (1985). *Introduction to Percolation Theory*. Abingdon, UK: Taylor & Francis. DOI: 10.4324/9780203211595.

Steinwart, I. and Christmann, A. (2008). *Support Vector Machines*. 1st ed. 2008. Information Science and Statistics. New York, NY: Springer New York. ISBN: 9780387772424. DOI: 10.1007/978-0-387-77242-4.

Stiti, M., Labergue, A., Hervy, F., Castanet, G., Becker, S., and Lemoine, F. (2021). "Characterization of supercooled droplets in an icing wind tunnel using laser-induced fluorescence". *Experiments in Fluids* 62.8, p. 4902. DOI: 10.1007/s00348-021-03210-x.

Stow, C. D. and Stainer, R. D. (1977). "The physical products of a splashing water droplet". *Journal of Meteorological Society of Japan* 55, pp. 518–532.

Stumpf, B., Hussong, J., and Roisman, I. V. (2022a). "Drop impact onto a substrate wetted by another liquid: flow in the wall film". *Colloids and Interfaces* 6.4, p. 58. DOI: 10.3390/colloids6040058.

Stumpf, B., Roisman, I. V., Yarin, A. L., and Tropea, C. (2023). "Drop impact onto a substrate wetted by another liquid: corona detachment from the wall film". *Journal of Fluid Mechanics* 956, p. 625. DOI: 10.1017/jfm.2022.1060.

Stumpf, B., Ruesch, J. H., Roisman, I. V., Tropea, C., and Hussong, J. (2022b). "An imaging technique for determining the volume fraction of two-component droplets of immiscible fluids". *Experiments in Fluids* 63.7, p. 113. DOI: 10.1007/s00348-022-03462-1.

Tang, X., Saha, A., Law, C. K., and Sun, C. (2019). "Bouncing drop on liquid film: Dynamics of interfacial gas layer". *Physics of Fluids* 31.1, p. 013304. DOI: 10.1063/1.5063257.

Taylor, G. I. (1959). "The dynamics of thin sheets of fluid. III. Disintegration of fluid sheets". *Proceedings of the Royal Society of London. Series A: Mathematical and Physical Sciences* 253, pp. 625–639.

Taylor, G. I. and Michael, D. H. (1973). "On making holes in a sheet of liquid". *Journal of Fluid Mechanics* 58.4, pp. 625–639.

Terzis, A., Kirsch, M., Vaikuntanathan, V., Geppert, A. K., Lamanna, G., and Weigand, B. (2019). "Splashing characteristics of diesel exhaust fluid (AdBlue) droplets impacting on urea-water solution films". *Experimental Thermal and Fluid Science* 102.1–6, pp. 152–162. DOI: 10.1016/j.expthermflusci.2018.11.002.

Thoraval, M.-J., Takehara, K., Etoh, T. G., and Thoroddsen, S. T. (2013). "Drop impact entrapment of bubble rings". *Journal of Fluid Mechanics* 724.724, pp. 234–258. DOI: 10.1017/jfm.2013.147.

Thoraval, M.-J., Takehara, K., Etoh, T. G., Popinet, S., Ray, P., Josserand, C., Zaleski, S., and Thoroddsen, S. T. (2012). "von Kármán vortex street within an impacting drop". *Physical Review Letters* 108.26, p. 264506. DOI: 10.1103/PhysRevLett.108.264506.

Thoroddsen, S. T. (2002). "The ejecta sheet generated by the impact of a drop". *Journal of Fluid Mechanics* 451, pp. 373–381. DOI: 10.1017/S0022112001007030.

Thoroddsen, S. T., Etoh, T. G., and Takehara, K. (2006). "Crown breakup by Marangoni instability". *Journal of Fluid Mechanics* 557, pp. 63–72. DOI: 10.1017/S002211200600975X.

– (2008). "High-speed imaging of drops and bubbles". *Annual Review of Fluid Mechanics* 40.1, pp. 257–285. DOI: 10.1146/annurev.fluid.40.111406.102215.

Thoroddsen, S. T., Thoraval, M.-J., Takehara, K., and Etoh, T. G. (2011). "Droplet splashing by a slingshot mechanism". *Physical Review Letters* 106, p. 034501. DOI: 10.1103/PhysRevLett.106.034501.

Tosun, I., ed. (2007). *Modeling in Transport Phenomena (Second Edition)*. Second Edition. Amsterdam: Elsevier Science B.V. ISBN: 978-0-444-53021-9.

Tropea, C. and Marengo, M. (1999). "The impact of drops on walls and films". *Multiphase Science and Technology* 11.1, pp. 19–36. DOI: 10.1615/MultScienTechn.v11.i1.20.

Tropea, C. and Roisman, I. V. (2000). "Modeling of spray impact on solid surfaces". *Atomization and Sprays* 10.3-5, pp. 387–408. DOI: 10.1615/AtomizSpr.v10.i3-5.80.

Trujillo, M. F. and Lee, C. F. (2001). "Modeling crown formation due to the splashing of a droplet". *Physics of Fluids* 13, p. 2503.

van Hinsberg, N. P., Budakli, M., Göhler, S., Berberović, E., Roisman, I. V., Gambaryan-Roisman, T., Tropea, C., and Stephan, P. (2010). "Dynamics of the cavity and the surfacee film for impingements of single drops on liquid films of various thickness". *Journal of Colloid and Interface Science* 350, pp. 336–343. DOI: 10.1016/j.jcis.2010.06.015.

Vander Wal, R. L., Berger, G. M., and Mozes, S. D. (2006). "The combined influence of a rough surface and thin fluid film upon the splashing threshold and splash dynamics of a droplet impacting onto them". *Experiments in Fluids* 40.1, pp. 23–32. DOI: 10.1007/s00348-005-0043-3.

Versluis, M. (2013). "High-speed imaging in fluids". *Experiments in Fluids* 54.2, p. 69. DOI: 10.1007/s00348-013-1458-x.

Videen, G., Ngo, D., Chýlek, P., and Pinnick, R. G. (1995). "Light scattering from a sphere with an irregular inclusion". *Journal of the Optical Society of America A* 12.5, p. 922. DOI: 10.1364/JOSAA.12.000922.

Visser, C. W., Kamperman, T., Karbaat, L. P., Lohse, D., and Karperien, M. (2018). "In-air microfluidics enables rapid fabrication of emulsions, suspensions, and 3D modular (bio)materials". *Science advances* 4.1, eaao1175. DOI: 10.1126/sciadv.aao1175.

Wacławczyk, T. (2017). "On a relation between the volume of fluid, level-set and phase field interface models". *International Journal of Multiphase Flow* 97.5672, pp. 60–77. DOI: 10.1016/j.ijmultiphaseflow.2017.08.003.

Wakimoto, T. and Azuma, T. (2009). "Influence of the physical properties of a liquid on perforations in a radial liquid sheet jet". *Journal of Fluid Science and Technology* 4.2, pp. 359–367. DOI: 10.1299/jfst.4.359.

Wang, A.-B. and Chen, C.-C. (2000). "Splashing impact of a single drop onto very thin liquid films". *Physics of Fluids* 12.9, pp. 2155–2158. DOI: 10.1063/1.1287511.

Wang, J. J., Gouesbet, G., Han, Y. P., and Gréhan, G. (2011). "Study of scattering from a sphere with an eccentrically located spherical inclusion by generalized Lorenz-Mie theory: internal and external field distribution". *Journal of the Optical Society of America A* 28.1, pp. 24–39. DOI: 10.1364/JOSAA.28.000024.

Wang, J.-X., Guo, W., Xiong, K., and Wang, S.-N. (2020). "Review of aerospace-oriented spray cooling technology". *Progress in Aerospace Sciences* 116.4–5, p. 100635. DOI: 10.1016/j.paerosci.2020.100635.

Weiss, D. A. and Yarin, A. L. (1999). "Single drop impact onto liquid films: neck distortion, jetting, tiny bubble entrainment, and crown formation". *Journal of Fluid Mechanics* 385, pp. 229–254. DOI: 10.1017/S002211209800411X.

Whitham, G. B. (1974). *Linear and Nonlinear Waves*. ISBN: 0-471-35942-4.

Worthington, A. M. (1908). *A Study of Splashes*. Nineteenth Century Collections Online: Photography: The World through the Lens. Longmans, Green, and Company.

Wu, Y., Wang, Q., and Zhao, C. Y. (2020). "Three-Dimensional droplet splashing dynamics measurement with a stereoscopic shadowgraph system". *International Journal of Heat and Fluid Flow* 83.7, p. 108576. DOI: 10.1016/j.ijheatfluidflow.2020.108576.

– (2021). "A comparative study of the immiscibility effect on liquid drop impacting onto very thin films". *Experiments in Fluids* 62.7, p. 162. DOI: 10.1007/s00348-021-03232-5.

Xie, H., Koshizuka, S., and Oka, Y. (2004). "Modelling of a single drop impact onto liquid flm using particle method". International Journal for numerical Methods in Fluids.45, pp. 1009–1023.

Yang, X., Dai, L., and Kong, S.-C. (2017). "Simulation of liquid drop impact on dry and wet surfaces using SPH method". *Proceedings of the Combustion Institute* 36.2, pp. 2393–2399. DOI: 10.1016/j.proci.2016.07.031.

Yarin, A. L. (1992). "Flow-induced on-line crystallization of rodlike molecules in fiber spinning". *Journal of Applied Polymer Science* 46.5, pp. 873–878. DOI: 10.1002/app.1992.070460514.

– (1993). *Free liquid jets and films: Hydrodynamics and rheology*. Interaction of mechanics and mathematics series. Harlow and New York: Longman Scientific & Technical and Wiley. ISBN: 0582102952.

– (2006). "Drop impact dynamics: splashing, spreading, receding, bouncing. . ." *Annual Review of Fluid Mechanics* 2006.38, pp. 159–192. DOI: 10.1146/annurev.fluid..

Yarin, A. L., Brenn, G., Kaster, O., Rensink D., and Tropea, C. (1999). "Evaporation of acoustically levitated droplets". *Journal of Fluid Mechanics* 399, pp. 151–204. DOI: 10.1017/S0022112099006266.

Yarin, A. L., Pfaffenlehner, M., and Tropea, C. (1998). "On the acoustic levitation of droplets". *Journal of Fluid Mechanics* 356, pp. 65–91. DOI: 10.1017/S0022112097007829.

Yarin, A. L., Roisman, I. V., and Tropea, C. (2017). *Collision Phenomena in Liquids and Solids*. Cambridge: Cambridge University Press. ISBN: 1107147905. DOI: 10.1017/9781316556580.

Yarin, A. L. and Weiss, D. A. (1995). "Impact of drops on solid surfaces: self-similar capillary waves, and splashing as a new type of kinematic discontinuity". *Journal of Fluid Mechanics* 283, pp. 141–173.

Yarin, L. P. (2012). *The Pi-Theorem: Applications to Fluid Mechanics and Heat and Mass Transfer*. Berlin: Springer Science & Business Media.

Zhang, D., Papadikis, K., and Gu, S. (2014). "Application of a high density ratio lattice-Boltzmann model for the droplet impingement on flat and spherical surfaces". *International Journal of Thermal Sciences* 84, pp. 75–85. DOI: 10.1016/j.ijthermalsci.2014.05.002.

Zhang, L., Huang, J., Si, T., and Xu, R. X. (2012). "Coaxial electrospray of microparticles and nanoparticles for biomedical applications". *Expert Teview of Medical Devices* 9.6, pp. 595–612. DOI: 10.1586/erd.12.58.

Zhou, W., Tropea, C., Chen, B., Zhang, Y., Luo, X., and Cai, X. (2020). "Spray drop measurements using depth from defocus". *Measurement Science and Technology* 31.7, p. 075901. DOI: 10.1088/1361-6501/ab79c6.

Zhou, W., Zhang, Y., Chen, B., Tropea, C., Xu, R., and Cai, X. (2021). "Sensitivity analysis and measurement uncertainties of a two-camera depth from defocus imaging system". *Experiments in Fluids* 62.11, p. 136. DOI: 10.1007/s00348-021-03316-2.

Nomenclature

Acronyms

CCD	charge-coupled device
CCS	chromatic confocal sensor
CD	corona detachment
CL	chromatic line
CMOS	complementary metal-oxide-semiconductor
DFD	depth from defocus
DOF	depth of field
ECOC	error correcting output
FOV	field of view
FP	focal plane
fps	frames per second
IC	internal combustion
KD	kinematic discontinuity
LB	Lattice Boltzman
LED	light emitting diode
LP	Lagrangian particle
LS	level-set
NI-DAQ	National Instruments - data aquisition system
OVA	one versus all
OVO	one versus one

P1	perspective 1
P2	perspective 2
PD	phase Doppler
PHF	phase field method
PIV	particle image velocimetry
PTV	particle tracking velocimetry
SCR	selective catalytic reduction
SLS	standard-level-set
SPL	sound pressure level
SVM	support vector machine
VOF	volume of fluid

Dimensionless groups

Co	Corona number
Fr	Froude number
K	dimensionless splash threshold parameter
$K^\star$	compound K number
K_d	K number based on the drop fluid parameters
K_f	K number based on the film fluid parameters
Oh	Ohnesorge number
Re	Reynolds number
$\mathrm{Re}^\star$	film Reynolds number
$\mathrm{Re}_{\mathrm{il}}$	impact Reynolds number for estimated laminar transition
Re_{i}	impact Reynolds number
Re_f	Reynolds number based on film liquid properties
We	Weber number
$\mathrm{We}^\star$	compound We number

We_f	Weber number based on film liquid properties	

Greek letters

α	angle of rupture rim relative to the z axis	rad
α_c	crown angle	rad
α_d	angle of the drop generatrix path to the horizontal	rad
α_L	dimensionless constant	
α_{dl}	characteristic drop generatrix path angle	rad
$\tilde{\delta}$	dimensionless initial film thickness	
$\tilde{\delta}_1$	dimensionless displacement thickness	
$\tilde{\delta}_{\mathrm{BL}}$	dimensionless boundary-layer thickness	
δ_0	initial perturbation amplitude	m
δ_{BL}	boundary-layer thickness	m
$\tilde{\eta}$	dimensionless constant	
η_d	dynamic viscosity of the drop	$\mathrm{kg\,m^{-1}\,s^{-1}}$
η_f	dynamic viscosity of the film	$\mathrm{kg\,m^{-1}\,s^{-1}}$
η_K	Kolmogorov length scale	m
γ	dimensionless constant	
κ	wavenumber	$\mathrm{m^{-1}}$
κ'	dummy variable	$\mathrm{m^{-1}}$
κ_*	viscosity ratio	
κ_h	wave number related to the sheet thickness	$\mathrm{m^{-1}}$
λ	dimensionless relative area occupied by holes	
λ_1	time dependent function	
λ_i	dimensionless constant	
ν	kinematic viscosity	$\mathrm{m\,s^{-2}}$
ν_d	kinematic viscosity of the drop	$\mathrm{m\,s^{-2}}$

ν_f	kinematic viscosity of the film	$\mathrm{m\,s^{-2}}$
$\Delta\Phi$	change of surface energy	$\mathrm{kg\,m^{2}\,s^{-2}}$
$\Delta\Phi'_*$	hole energy per unit volume	$\mathrm{kg\,m^{-1}\,s^{-2}}$
$\Delta\Phi_*$	activation energy for hole nucleation	$\mathrm{kg\,m^{2}\,s^{-2}}$
$\Delta\Phi_{\mathrm{film}}$	surface energy decrease	$\mathrm{kg\,m^{2}\,s^{-2}}$
$\Delta\Phi_{\mathrm{rim}}$	surface energy increase	$\mathrm{kg\,m^{2}\,s^{-2}}$
σ	surface tension	$\mathrm{N\,m^{-1}}$
σ_d	surface tension of the drop	$\mathrm{N\,m^{-1}}$
σ_f	surface tension of the film	$\mathrm{N\,m^{-1}}$
τ	integration time	s
$\tilde{\tau}$	dimensionless constant	
τ_η	characteristic time scale of Kolmogorov dissipative eddies	s
τ_0	characteristic time scale of large eddies	s
τ_{ca}	characteristic time of capillary breakup	s
τ_{gen}	time of turbulence generation	s
τ_{hole}	characteristic time of hole formation	s
τ_{nucl}	characteristic time of nucleation	s
τ_{id}	shear stress in the drop liquid	$\mathrm{kg\,m^{-1}\,s^{-2}}$
$\tilde{\tau}_{\mathrm{ini}}$	dimensionless temporal offset	
τ_i	shear stress at the film-drop interface	$\mathrm{kg\,m^{-1}\,s^{-2}}$
θ	angle of the rupture rim relative to the impact axis	rad
ε	ellipsoidal deformation	
ε_K	specific dissipation rate	$\mathrm{m^{2}\,s^{3}}$
ϱ	density	$\mathrm{kg\,m^{-3}}$
ϱ_*	density ratio	
ϱ_d	density of the drop	$\mathrm{kg\,m^{-3}}$

ϱ_f	density of the film	$\mathrm{kg\,m^{-3}}$
ξ	scaled time parameter	
ζ	Lagarangian location parameter	

Latin letters

A	dimensionless scaling factor	
A_0	dimensionless scaling factor	
a_0	unperturbed cross sectional radius of a jet	m
A_{inner}	projected area of the inner drop	$\mathrm{m^2}$
A_{ratio}	ratio of projected areas	
A_{total}	projected area of the total drop	$\mathrm{m^2}$
A_c	dimensionless constant	
a_h	cross sectional rim radius	m
A_K	dimensionless prefactor	
a_s	intersection radius	m
B	dimensionless parameter characterising the radial velocity distribution of the lamella flow	
$\vec{b}$	observation vector	
C	Kolmogorov spectrum constant	
c	number of classes	
C_{r}	dimensionless constant	
C_K	spectral constant	
C_l	speed of sound in liquid	$\mathrm{m\,s^{-1}}$
C_s	dimensionless constant	
d	decoding function	
$\bar{d}_{\mathrm{sec}}$	average diameter of secondary droplets	m
d'	complement of the decoding function	
D_0	drop diameter	m

D_{maj}	major axis length of a drop	m
D_{min}	minor axis length of a drop	m
d_{mod}	modal diameter of secondary droplets	m
d_{prim}	mean diameter of primary spray	m
dn	number of holes formed on a ring	
E	Energy spectrum of turbulence	$\mathrm{m^3\,s^{-2}}$
e_i	three-dimensional normalized eccentricity vector	
E_T	kinetic energy of turbulence per unit volume	$\mathrm{kg\,m^{-1}\,s^{-2}}$
$e_{i,\mathrm{proj}}$	two-dimensional projected eccentricity vector	
f_j	classifier	
g	loss function	
h	local film thickness	m
H_{f0}	initial film thickness	m
h_{res}	residual film thickness	m
h_b	estimated breakup thickness	m
h_c	liquid sheet thickness	m
h_f	wall film thickness	m
$\tilde{h}_f$	dimensionless wall film thickness	
$\tilde{h}_{\mathrm{yw}}$	dimensionless lamella thickness defined by Yarin and Weiss (1995)	
h_l	lamella thickness in front of the kinematic discontinuity	m
$\tilde{h}_l$	dimensionless lamella thickness in front of the kinematic discontinuity	m
$\tilde{h}_{\mathrm{inv}}$	dimensionless lamella thickness defined by Roisman (2009a)	
$h_{\nu f}$	characteristic viscid wall film thickness	m
$h_{\mathrm{res},d}$	residual height of the drop liquid	m
$h_{\mathrm{res},f}$	residual height of the film liquid	m
I_*	specific hole formation rate	$\mathrm{m^{-2}\,s^{-1}}$

k	number of characteristic time scales	
$\hat{k}$	predicted class	
K_{crit}	critical K number	
k_T	specific pulsation energy	$\mathrm{m^2\,s^{-2}}$
l	number of binary classifiers	
$\tilde{L}$	dimensionless crown height	
L_{nd}	characteristic length scale of roughness	m
m	number of holes reaching a specific location	
m_{sec}	mass of secondary droplets	kg
m_{kj}	coding matrix	
N	number of dimensions	
n	number of features	
n_{r}	dimensionless exponent	
N_{sec}	number of secondary droplets	
n_g	refractive index of gas	
N_h	average number of holes	
n_l	refractive index of liquid	
n_s	dimensionless exponent	
P	probability of a critical hole	
P_0	probability of zero holes reaching a specific location	
P_m	probability of m holes reaching a specific location	
p_{id}	pressure at the drop interface	$\mathrm{kg\,m^{-1}\,s^{-2}}$
p_{if}	pressure at the wall film interface interface	$\mathrm{kg\,m^{-1}\,s^{-2}}$
Q	specific volume flux	$\mathrm{m^2\,s^{-1}}$
R	ring radius	m
$\bar{r}_{\mathrm{cs},12}$	time averaged crown radius	m

$\tilde{r}$	dimensionless radial coordinate	
r_*	critical hole nucleus size	m
$R_{\mathrm{c,ini}}$	dimensionless initial crown radius	
$r_{\max}$	maximum crown radius before breakup	m
r_{res}	radius of the residual disk	m
R_a	mean surface roughness	m
r_c	crown radius	m
$\tilde{r}_c$	dimensionless crown radius	
R_h	least visible hole radius	m
r_h	hole radius	m
$r_{\mathrm{cs},1}$	crown radius at instant one	m
$r_{\mathrm{cs},2}$	crown radius at instant two	m
r_{cs}	crown radius as a function of the axial coordinate	m
r_{KD}	radial position of the kinematic discontinuity	
s_{az}	arc length of the rupture rim path	m
s_j	output of the coding matrix	
T	temperature	°C
t	time	s
$\bar{t}_d$	dimensionless time of detachment	
$\tilde{t}$	dimensionless time	
$\tilde{t}_0$	dimensionless temporal offset	
$\tilde{t}_{\nu f}$	dimensionless characteristic time of the boundary layer in the wall film	s
t_1	time at instant one	s
t_2	time at instant two	s
t_ν	characteristic time of the boundary layer in the lamella	s
$\tilde{t}_\nu$	dimensionless characteristic time of the boundary layer	

t_{res}	time of residual film	s
t_d	time of corona detachment	s
T_e	temperature in energy units	$\mathrm{kg\,m^{-1}\,s^{-2}}$
t_e	evaluated time interval	s
Δt_e	temporal error	s
T_e^*	energy equivalent temperature	K
$t_{\nu f}$	characteristic time of the boundary-layer in the wall film	s
$\bar{u}_{i,\mathrm{sec}}$	mean velocity of secondary droplets	$\mathrm{m\,s^{-1}}$
$\tilde{U}_c$	dimensionless radial velocity of the lamella at the crown base.	
U_0	drop impact velocity	$\mathrm{m\,s^{-1}}$
U_1	velocity from lamella into the kinematic discontinuity	$\mathrm{m\,s^{-1}}$
U_2	velocity in the wall film	$\mathrm{m\,s^{-1}}$
u_{az}	azimuthal velocity of rupture rim	$\mathrm{m\,s^{-1}}$
U_{i}	velocity of drop-film intersection	$\mathrm{m\,s^{-1}}$
U_{KD}	velocity of the kinematic discontinuity	$\mathrm{m\,s^{-1}}$
u_{tc}	Taylor Culick velocity	$\mathrm{m\,s^{-1}}$
u_{typ}	typical rim velocity	$\mathrm{m\,s^{-1}}$
$\tilde{u}_r$	dimensionless velocity in radial direction	
$\tilde{u}_y$	dimensionless velocity in axial direction	
$u_{\mathrm{az},e}$	error of the azimuthal rupture rim velocity	$\mathrm{m\,s^{-1}}$
$\tilde{V}_{\mathrm{crown}}$	dimensionless crown volume	
V_{frac}	volume fraction	
V_{inner}	volume of the inner drop	$\mathrm{m^3}$
V_{total}	total drop volume	$\mathrm{m^3}$
W	rate of change of wall film thickness	$\mathrm{m\,s^{-1}}$
W_{i0}	initial axial velocity of drop-wall film interface	$\mathrm{m\,s^{-1}}$

x_0	longitudinal position of the impact axis	m
x_{CL}	longitudinal coordinate of chromatic line sensor	m
x_{R}	horizontal position of the rupture rim	m
x_e	typical displacement	m
Δx_e	spatial error	m
$\tilde{y}$	dimensionless axial coordinate	

List of Figures

List of Tables

A. Mechanisms of the film desintegration by hole nucleation and expansion: Analytical analysis [1]

A.1. Spontaneously growing holes in liquid films

Examination of images of disintegrating liquid films reveals that multiple holes often appear prior to breakup (cf. Brenn et al., 2005). These holes proliferate into the intact film because of the surrounding circular free rims and are driven by surface tension according to the Taylor-Culick mechanism (Taylor, 1959; Culick, 1960; Yarin et al., 2017). These expanding holes then merge, leaving a network of ligaments, which break up due to capillary instability. This is the scenario further explored analytically in the present work in relation to the mechanism of corona detachment.

Free liquid films, being a two-dimensional continuum, are not inherently prone to break up into droplets, because in contrast to one-dimensional continua (jets), their surface energy would increase through breakup. Therefore, holes appear only as a result of a nucleation, which is, for example, a perturbation resulting from disturbances in the corona wall film. Note also that perturbations can be introduced in free liquid films by an atomizer exit, or turbulent pulsations in the surrounding air, which also result in hole nucleation, as observed in Wakimoto and Azuma (2009) at high Reynolds numbers.

Consider a circular disk-like hole in a film of thickness h_c. The hole in the film is surrounded by a free rim of cross-sectional radius a_h, which accommodates the liquid volume removed from the hole, i.e. $\pi(r_h + a_h)^2 h_c$, where r_h is the radius of the rim centerline. The situation is sketched in Figure A.1.

The rim volume is $2\pi^2 r_h a_h^2$, and thus, volume conservation yields

$$a = \frac{r_h h_c^{1/2}}{\sqrt{2\pi r_h} - h_c^{1/2}}. \tag{A.1}$$

[1] Parts of this chapter are published in Stumpf et al. (2023), used under CC BY 4.0.

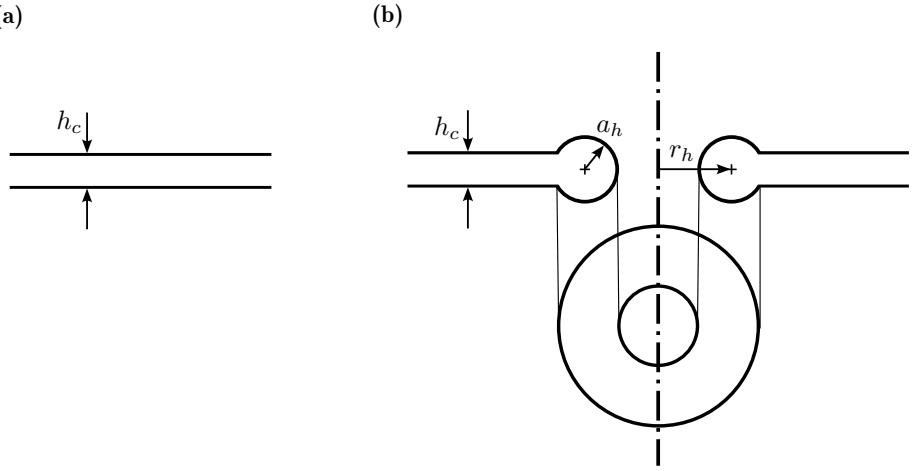

Figure A.1: Sketch of a) a liquid sheet of thickness h_c and b) the liquid sheet with a circular hole of radius r_h surrounded by a toroidal rim of cross-sectional radius a_h.

Note that in recent work of Bang et al. (2023), where similar arguments related to hole formation on swirling liquid films issued from pressure-swirl atomizers were considered, a_h was neglected compared to r_h, which leads to an equation for the cross-sectional radius a_h without the term $h_c^{1/2}$ in the denominator instead of Eq. (A.1), and the related changes in the equations of Bang et al. (2023) corresponding to Eqs. (A.2)-(A.6) here. It should be emphasized that the present refined version of Eqs. (A.1)-(A.6) is preferable.

The surface energy increase attributed to the surface energy of the free rim, $\Delta\Phi_{\mathrm{rim}} = 4\sigma\pi^2 r_h a_h$ is expressed accounting for Eq. (A.1) as

$$\Delta\Phi_{\mathrm{rim}} = \frac{4\sigma\pi^2 r_h^2 h_c^{1/2}}{\sqrt{2\pi r_h} - h_c^{1/2}}, \tag{A.2}$$

where σ is the surface tension.

The surface energy decrease due to the hole formation is

$$\Delta\Phi_{\mathrm{film}} = -2\pi(r_h + a_h)^2\sigma \tag{A.3}$$

Here the factor 2 accounts for the two surfaces of the film.

Equations (A.2) and (A.3) show with the help of (A.1) that the total energy change related to the formation of a hole is

$$\Delta\Phi(r_h) = \Delta\Phi_{\text{film}} + \Delta\Phi_{\text{rim}} = -\frac{4\pi^2 r^2 \left(h_c - \sqrt{2\pi r_h h_c} + r_h\right)\sigma}{\left(\sqrt{2\pi r_h} - \sqrt{h_c}\right)^2}. \tag{A.4}$$

The function $\Delta\Phi(r_h)$ has a maximum corresponding to the condition $d\Delta\Phi(r_h)/dr = 0$, which yields the critical hole nucleus size

$$r_* \approx 2.18 h_c. \tag{A.5}$$

If the radius of a hole 'nucleus' r_h is smaller than r_*, its growth would correspond to an increase in the total energy, given by Eq. (A.4), i.e., it is energetically unfavorable and thus, cannot be spontaneous. On the other hand, if a hole 'nucleus' is larger than the critical one, i.e., $r_h > r_*$, its growth would correspond to a decrease in the total energy $\Delta\Phi(r_h)$ given by Eq. (A.4), i.e., it would be energetically favorable and thus, spontaneous. The critical total energy corresponding to the critical hole 'nucleus' is found as $\Delta\Phi_* = \Delta\Phi(r_*)$, and according to Eqs. (A.4) and (A.5), is equal to

$$\Delta\Phi_* \approx 13.4\sigma h_c^2 \tag{A.6}$$

This expresses the activation energy required to be exceeded to form a spontaneously growing hole. The next step is then to formulate the probability that a hole of this size will occur, given random disturbances in a liquid sheet. This is the subject of the next subsection.

Taylor and Michael (1973) also developed an approach to determine the critical size of a hole which would grow. They propose a catenoidal shape, which guarantees zero capillary pressure in the liquid on the hole that remains in equilibrium with the surrounding vacuum. There are two possible catenoidal hole shapes of different sizes, with the smaller one (in radius) being stable, and thus, non-growing, and the larger one being unstable, and thus, growing. This approach uses stability arguments based on the surface energy of catenoidal holes and yields $r_* \sim h_c$ [cf. Eq. (A.5)]. However, this approach neglects the formation of a free rim, which could be realized in the Taylor and Michael (1973) apparatus with suspended soap films, but is inapplicable to hole formation in dynamic free liquid films originating from drop impacts onto pre-existing liquid films [or many other films, e.g., those originating from swirl atomizers as in (Bang et al., 2023)]. Furthermore, the requirement of zero capillary pressure in liquid in equilibrium with the surrounding vacuum is arbitrary. The present approach accounts for realistic configurations of holes with free rims, and moreover, does not insist that their growth inevitably begins from an arbitrary chosen equilibrium catenoidal shape.

A.2. Turbulent eddies in liquid films

The intermittency and instability mechanisms at the base of the frontal ejecta arising underneath drops impacting onto liquid films are also driven by inertial effects (Thoraval et al., 2012; Li et al., 2018), which can represent the first steps in the cascade of instabilities leading to formation of turbulent eddies.

Consider a liquid film with turbulent eddies inside it, as suggested by the experiments of Wakimoto and Azuma (2009). Even though the global Reynolds numbers Re listed in Tab. 5.1 are of the order of 100-1000, local generation of turbulence near the drop bottom following the impact is not precluded at all. Indeed, the global Reynolds number $Re = U_0 D_0/\nu$ based on the drop impact velocity U_0 does not characterise at all the situation at the drop bottom at the moment following its impact, when disturbances set in, could grow and be swept into the forming lamella and crown sheet in the form of turbulent eddies. Indeed, the relevant velocity for the bottom part of the drop is that of the intersection between the drop and surface film U_i, rather than U_0. The former is related to the latter through $U_\mathrm{i} = U_0 \cot\alpha_d$, where α_d is the slope of the drop generatrix relative to the underlying horizontal surface (in particular, at the impact moment ($\alpha_d = 0$); (Lesser and Field, 1983). Moreover, if the condition $\sqrt{\nu/(D_0 C_l)} \ll 1$ holds (with C_l being the speed of sound in liquid), the entire droplet body is already involved in the radial spreading after the impact. This condition holds for investigated drops with $D_0 \approx 10^{-1}$ cm, $\nu = 10^{-2}$ cm^2/s and $C_l \approx 1.5$ km/s, whereby $\sqrt{\nu/(D_0 C_l)} \sim 10^{-3}$. That means that the characteristic scale of motion is D_0 and the characteristic Reynolds number is $\mathrm{Re_i} = (U_0 D_0/\nu)\cot\alpha_d$. Because at the moments following drop impact $\cot\alpha_d \to \infty$, the Reynolds number $\mathrm{Re_i} \to \infty$. Thus, turbulence generation near the drop bottom following the impact is real, and the growing disturbances are inevitably entrained as turbulent eddies into the spreading liquid lamella and corona arising from it. In the inertial range, down to the dissipation range, the distribution of pulsation energy by wavenumber κ, $E(\kappa)$ is given by the Kolmogorov spectrum (Kolmogorov, 1962; Pope, 2001):

$$E(\kappa) = C\varepsilon_K^{2/3}\kappa^{-5/3}, \tag{A.7}$$

where ε_K is the specific dissipation rate, and C is the universal Kolmogorov spectrum constant $C = 1.5$ according to George et al. (1984), which is related to the experimentally determined spectral constant C_K as $C = (55/18)C_K$ (Sreenivasan, 1995)

The specific pulsation energy k_T of all the turbulent eddies in the film is found as

$$k_T = \int_{\kappa_h}^{\infty} E(\kappa')d\kappa' = \frac{3}{2}C\left(\frac{\varepsilon_K h_c}{2\pi}\right)^{2/3}, \tag{A.8}$$

where $\kappa_h = 2\pi/h_c$, and κ' is the dummy variable.

The Kolmogorov length scale is $\eta_K = (\nu^3/\varepsilon_K)^{1/4}$, with ν being the kinematic viscosity. Assuming the overlap of the inertial and dissipation ranges, take $\eta_K \approx h_c$. Then, the dissipation rate is estimated as

$$\varepsilon_K \approx \frac{\nu^3}{h_c^4}. \tag{A.9}$$

Using Eqs. (A.8) and (A.9), one finds the kinetic energy of turbulence per unit volume, $E_T = \rho k_T$, as

$$E_T = \frac{3C}{2(2\pi)^{2/3}} \frac{\rho\nu^2}{h_c^2}. \tag{A.10}$$

The latter shows that the specific pulsation energy increases in smaller eddies (thinner films), as in the Kolmogorov theory.

Consider the film as a system of turbulent eddies and introduce its temperature in the energy units T_e as

$$T_e = E_T. \tag{A.11}$$

For the system of turbulent eddies one can, essentially repeat the entire thermodynamic derivation starting from the microcanonical δ-functional distribution to the introduction of the entropy S as in Landau and Lifshitz (2013)

$$\frac{dS}{dE} = \frac{1}{T_e^*}, \tag{A.12}$$

where E is understood here as the energy of velocity fluctuations. Then, the probability of a critical hole' is given by the Gibbs distribution (Landau and Lifshitz, 2013)

$$P = K' \exp\left(-\frac{\Delta\Phi'_*}{T_e}\right), \tag{A.13}$$

which is also called the Boltzmann distribution; K' is a dimensionless constant.

In Eq. (A.13), $\Delta\Phi'_* = \Delta\Phi_*/\pi[r_* + a_h(r_*)]^2 h_c$ is the hole energy per unit volume. According to Eqs. (A.5) and (A.6), $\Delta\Phi'_* \approx 0.48\sigma/h_c$. Then, Eqs. (A.10), (A.11) and (A.13) yield

$$P \approx K' \exp\left[-\frac{1.09}{C}\frac{\sigma h_c}{\rho\nu^2}\right]. \tag{A.14}$$

At $h_c = 0$, the probability of a system with a critical hole is 1, which yields $K' = 1$, and thus,

$$P = \exp\left[-\frac{1.09}{C}\frac{\sigma h_c}{\rho\nu^2}\right]. \tag{A.15}$$

Equation (A.15) shows that the thinner the film is, the higher is the probability of a critical hole forming. Taking for an estimate the parameters of water, $\rho = 1\,\mathrm{g/cm^3}$, $\sigma = 72\,\mathrm{g/s^2}, \nu = 10^{-2}\,\mathrm{cm^2/s}$, and the above-mentioned value of the empirical constant $C = 1.5$, one obtains $P = 0.59$ for $h_c = 10$ nm. The estimation for the silicon oil S10 yields $P = 0.49$ (ρ=0.93 g/cm^3) for $h_c = 5$ µm.

A.3. Evolution of film thickness in time

The probability of critical hole formation (A.15) depends on time because the corona wall thickness h_c depends on time. Consider the simplest case where the pre-existing film on the wall and the impacting drop are of the same liquid. In this case the experiments show that corona detachment is possible. Then, the theory of Yarin and Weiss (1995) is applicable and the dimensionless radial velocity in the film on the wall at the spreading corona, $\tilde{U}_c$, is given by

$$\tilde{U}_c = \frac{B\tilde{r}_c}{1 + B(\tilde{t} - \tilde{t}_0)}, \tag{A.16}$$

where B is dimensionless and determined by the radial velocity gradient in the film on the wall resulting from the drop impact near the impact center. Note that here and hereinafter time is rendered dimensionless using D_0/U_0, velocity using U_0 and lengths using D_0. Dimensionless times, lengths and velocities are signified here with a tilde. The time shift $\tilde{t}_0$ is required because, as discussed in Yarin and Weiss (1995), this theory describes only a remote-asymptotics and cannot be extended to the drop impact time $\tilde{t} = 0$; cf. $\tilde{\tau}$ in Eq. (2.8). The shift is equivalent to the 'polar distance' introduced when the theory of self-similar submerged jets, valid as remote asymptotics, is compared to the experimental data acquired using jets issued from a finite nozzle (Abramovich, 1963, cf.).

In addition,

$$\tilde{r}_c = \sqrt{2A_c(\tilde{t} - \tilde{t}_0)} \tag{A.17}$$

is the current dimensionless radial position of the corona, with A_c being the dimensionless integral characteristic of the radial velocity distribution in the film on the wall resulting from the drop impact.

Note that neither parameter A_c nor parameter B in Eqs. (A.16) and (A.17) are the adjustable constants in the theory of Yarin and Weiss (1995). They are the characteristics of an earlier velocity distribution in the lamella following drop impact, which are 'inherited' by the remote-asymptotics theory of Yarin and Weiss (1995) or Eqs. (A.16) and (A.17). If one would use a detailed numerical model of drop evolution after impact up to the remote asymptotics stage when a corona is formed, the parameters A and B could be fully predicted, and that had, essentially, been done in the numerical simulations of Weiss and Yarin (1999). The same is true regarding the time shift $\tilde{t}_0$, which is similar to the polar distance widely used in the theory of self-similar jets, which is nothing but a remote-asymptotics theory of non-self-similar jets (Abramovich, 1963). It can be predicted using the numerically simulated evolution of a non-self-similar jet toward the remote-asymptotics self-similar regime, as in Dzhaugashtin and Yarin (1977). The Yarin and Weiss (1995) theory leading to Eqs. (A.16) and (A.17) is an inviscid one, and in general, an effect of the Reynolds number could modify these equations.

Accordingly,

$$\tilde{U}_c = B\sqrt{2A}\frac{\sqrt{\tilde{t}-\tilde{t}_0}}{1+B(\tilde{t}-\tilde{t}_0)}. \tag{A.18}$$

Assuming negligible viscous losses when the liquid is propelled from the film to the corona, one can find the dimensionless corona height $\tilde{L}$ integrating the following equation:

$$\frac{d\tilde{L}}{d\tilde{t}} = \tilde{U}_c, \tag{A.19}$$

which together with Eq. (A.18) yields

$$\tilde{L} = 2\sqrt{2A}\left[\sqrt{\tilde{t}-\tilde{t}_0} - \frac{1}{\sqrt{B}}\arctan\sqrt{B(\tilde{t}-\tilde{t}_0)}\right]. \tag{A.20}$$

For relatively short times of interest here, Eq. (A.20) yields

$$\tilde{L} = \frac{2\sqrt{2A}B}{3}(\tilde{t}-\tilde{t}_0)^{3/2}. \tag{A.21}$$

Accordingly, the current volume of the corona is

$$\tilde{V}_{\text{corona}} = 2\pi\tilde{r}_c\tilde{h_c}\tilde{L}. \tag{A.22}$$

whereby the volume is rendered dimensionless with D_0^3. On the other hand, this volume was propelled from the film on the wall inside the corona, i.e.,

$$\tilde{V}_{\text{corona}} = \pi\tilde{r}_c^2(\tilde{\delta}_{\text{f0}} - \tilde{h}_l), \quad \tilde{\delta}_{\text{f0}} = \frac{H_{\text{f0}}}{D_0}, \tag{A.23}$$

where $\tilde{h}_l$ is the current dimensionless film thickness on the wall inside the corona.

The film thickness rendered dimensionless by D_0 is found as (Yarin and Weiss, 1995)

$$\tilde{h}_l = \frac{\tilde{\delta}_{\text{f0}}}{[1+B(\tilde{t}-\tilde{t}_0)]^2}. \tag{A.24}$$

Then, using Eqs. (A.17) and (A.21) - (A.24) one obtains the dimensionless thickness of the corona wall as

$$\tilde{h}_c = \frac{3\tilde{\delta}_{\text{f0}}}{4B(\tilde{t}-\tilde{t}_0)}\left\{1 - \frac{1}{[1+B(\tilde{t}-\tilde{t}_0)]^2}\right\}. \tag{A.25}$$

In dimensional form, Eq. (A.25) reads

$$h_c = H_{\text{f0}}\frac{3D_0}{4BU_0(t-t_0)}\left\{1 - \frac{1}{[1+BU_0(t-t_0)/D_0]^2}\right\}. \tag{A.26}$$

As $(t - t_0) \to 0$, Eq. (A.26) yields

$$h_c = \frac{3}{2} H_{\mathrm{f0}}. \tag{A.27}$$

Then, according to Eq. (A.26), h_c decreases monotonically in time approximately as

$$h_c = H_{\mathrm{f0}} \frac{3D_0}{4BU_0(t - t_0)}. \tag{A.28}$$

According to Fig. 5.5, the corona sheet would break up at

$$h_c = h_b \approx 1\,\mu\mathrm{m} \tag{A.29}$$

and a reasonable estimate of the probability of hole formation would be, according to Eqs. (A.15) ,

$$P = \exp\left[-\frac{1.09}{C}\frac{\sigma h_b}{\rho\nu^2}\right]. \tag{A.30}$$

A.4. Hole growth process and the corona detachment time

Toroidal free rims surrounding the super-critical, spontaneously growing holes move outward with the Taylor-Culick velocity (Taylor, 1959; Culick, 1960; Yarin and Weiss, 1995),

$$u_{\mathrm{tc}} = \sqrt{\frac{2\sigma}{\rho h_c}}. \tag{A.31}$$

Consider a specific location in the film and hole forming around this location. Any hole which appears at a distance R from the location at time $\tau < t - R/u_{\mathrm{tc}}$ will reach this location before the instant t. The number of the holes $\mathrm{d}n$, formed in a ring of the radius R defined by the radius element $\mathrm{d}R$, which reach the considered point at time t can be estimated as

$$\mathrm{d}n = \int_0^{t-R/u_{\mathrm{tc}}} I_* 2\pi R \mathrm{d}R \mathrm{d}\tau = I_* \left(t - \frac{R}{u_{\mathrm{tc}}}\right) 2\pi R \mathrm{d}R, \tag{A.32}$$

where τ is an integration time, and I_* is the constant hole formation rate.

Note that if variation of I_* in time would be accounted for, one would have to evaluate the integral $\int_0^{t-R/u_{\mathrm{tc}}} I_* d\tau$ numerically, which would complicate the following calculations, but, in principle, does not affect the main theoretical structure.

In total, the average number of holes N_h which can reach the location under consideration during time t is

$$N_h = \int_0^{u_{tc}t} I_* \left(t - \frac{R}{u_{\mathrm{tc}}}\right) 2\pi R dR = I_* \frac{\pi}{3} \mathrm{u}_{\mathrm{tc}}^2 t^3. \tag{A.33}$$

Because the growing hole formation process is random, the probability that the location under consideration will be reached by m holes during time t is given by the Poisson distribution

$$P_m(t) = \frac{N_h^m}{m!}\exp(-N_h). \tag{A.34}$$

Then, the probability that zero holes will reach that location ($m = 0$), i.e., it will stay intact is equal to

$$P_0(t) = \exp(-N_h). \tag{A.35}$$

Accordingly, the relative area occupied by the holes, accounting for their interactions, is

$$\lambda = 1 - \exp(-N_h). \tag{A.36}$$

Note that the calculation of λ via Eqs. (A.32)-(A.36) is similar in a sense to the calculation of the degree of crystallization in polymer crystallization processes (Yarin, 1992; Yarin, 1993; Ghosal et al., 2020).

The characteristic time scale of Kolmogorov dissipative eddies is $\tau_\eta = (\nu/\varepsilon_K)^{1/2}$ (Kolmogorov, 1962; Pope, 2001). Using Eq. (A.9), one obtains

$$\tau_\eta = \frac{h_c^2}{\nu}. \tag{A.37}$$

Then, the specific rate of formation of growing holes per surface area is

$$I_* = \frac{P}{(\pi r_*^2)(k\tau_\eta)}. \tag{A.38}$$

where k is the number of characteristic time scales required for a hole formation. Using Eqs. (A.5), (A.37) and (A.38), one obtains

$$I_* = 0.067\frac{\nu}{kh_c^4}P. \tag{A.39}$$

The value of I_* found from Eqs. (A.27), (A.30) and (A.39) reads

$$I_* = 0.013\frac{\nu}{kH_{\mathrm{f0}}^4}\exp\left(-\frac{1.09}{C}\frac{\sigma h_b}{\rho\nu^2}\right). \tag{A.40}$$

The expression Eqs. (A.36) for the relative area of the holes λ with the help of Eqs. (A.27), (A.31) and (A.33) yields

$$\lambda = 1 - \exp\left(-\frac{4\pi I_*\sigma}{9\rho H_{\mathrm{f0}}}t^3\right). \tag{A.41}$$

According to the percolation theory (Stauffer, 1979; Stauffer and Aharony, 1985), when the value of

$$\lambda = \frac{1}{2} \tag{A.42}$$

has been reached, the intact film disappears. Then, Eqs. (A.41) and (A.42) yield the corona detachment time t_d as

$$t_\mathrm{d} = \left(\frac{9\ln 2}{4\pi} \frac{\rho H_\mathrm{f0}}{I_* \sigma} \right)^{1/3} . \tag{A.43}$$

According to Eqs. (A.40) and (A.43) the dependence of the corona detachment time t_d on the initial film thickness on the wall H_f0 is

$$t_\mathrm{d} = 3.37 \left(\frac{\rho k H_\mathrm{f0}^5}{\sigma \nu} \right)^{1/3} \exp\left(\frac{0.363}{C} \frac{\sigma h_b}{\rho \nu^2} \right) . \tag{A.44}$$

Using Eq. (A.29) the exponent in Eq. (A.44) with $h_b \approx 1$ µm and C=1.5 is approximately 1. Even small variations in estimating h_b will not alter the result significantly. Then, Eq. (A.44) yields

$$t_\mathrm{d} \approx 3.37 k^{1/3} \left(\frac{\rho H_\mathrm{f0}^5}{\sigma \nu} \right)^{1/3} . \tag{A.45}$$